

The performance of speckle filters on Copernicus Sentinel-1 SAR images containing natural oil slicks

Cristina A. Vrinceanu^{1*}, Stephen Grebby¹ and Stuart Marsh¹

¹Nottingham Geospatial Institute, University of Nottingham, Nottingham, NG7 2TU, UK

*Corresponding author (e-mail: cristina.vrinceanu@nottingham.ac.uk)

ORCID: C.A.V: <https://orcid.org/0000-0001-6305-3597>

Abbreviated title: Speckle filtering SAR data containing oil slicks

Abstract: Synthetic Aperture Radar (SAR) is traditionally used in the identification, mapping, and analysis of petroleum slicks, regardless of their origin. On SAR images, oil slicks appear as dark patches that contrast with the brightness of the surrounding sea surface. This distinction allows for automated detection algorithms to be designed using computer vision methods for objective oil slick identification. Nevertheless, efficient interpretation of the SAR imagery by statistical analysis can be diminished due to the speckle effect present on SAR images, a granular artefact associated with the coherent nature of SAR, which visually degrades the image quality. In this study, a quantitative and qualitative assessment of common SAR image despeckling methods is presented, analyzing their performance when applied to images containing natural oil slicks. The assessment is performed on Copernicus Sentinel-1 images acquired with various temporal and environmental conditions. The assessment covers a diverse area of filters that employ Bayesian and non-linear statistics in the spatial, transform and wavelet domains, focusing on their demonstrated performance and capabilities for edge and texture retention. In summary, the results reveal that filters using local statistics in the spatial domain produce consistent desired effects. The novel SAR-BM3D algorithm can be used effectively, albeit with a higher computational demand.

Supplementary material: Implementations of the speckle filters used in this paper are made available at: <https://github.com/cavrinceanu/specklefilters> under an MIT license. All figures are available at: [10.6084/m9.figshare.12935159](https://doi.org/10.6084/m9.figshare.12935159) . All table data is available at: [10.6084/m9.figshare.13010405](https://doi.org/10.6084/m9.figshare.13010405).

The offshore discharge of oil can have significant effects on marine ecology, the impact of which is dependent on the sensitivity of specific living organisms to the exposed surfactant. According to Migliaccio *et al.* (2005), the presence of oil can disrupt the life cycle of marine coastal communities. This disruption is dependent on the quantity, physical and chemical characteristics, location, seasonality, water depth and other metocean conditions. The main sources of oil pollution in the marine environment are linked to accidents involving tankers, leaking pipelines or damaged oil rigs, or intentional discharges such as bilge dumping and ship tank cleaning (National Research Council (US) Committee, 2003). Another common source is oil runoff into the ocean from land and coastal facilities following rainfall. A quantity ranging from 20×10^3 to 60×10^3 tonnes per year has been estimated to enter the oceans as a result of anthropogenic activities, accounting for approximately 53% of the total oil in global marine waters (National Research Council (US) Committee, 2003).

It is less widely acknowledged that the remaining 47% of the total is released naturally through seepage of oil from reservoirs and the erosion of hydrocarbon bearing sediments. An early estimate of the rate of natural oil discharge was provided by Wilson *et al.* (1974) at 600×10^3 tonnes per year, while Farrington (1985) estimated this at 250×10^3 tonnes per year a decade later. The most recent attempt to quantify the total natural hydrocarbon content in the ocean was by Kvenvolden and Cooper (2003), who note that a rate of 200×10^3 to 2×10^6 tonnes per year offers an accurate range for evaluation, which is also supported by National Research Council (US) Committee (2003). Current estimates vary considerably due to a shortfall in accurate and comprehensive assessments of the petroleum input into the marine environment. Thus, there is a clear need for an effective programme for detecting, mapping and quantifying the volume of both natural and anthropogenic petroleum discharges.

Synthetic Aperture Radar (SAR) images are usually acquired from spaceborne or unmanned aerial vehicles using active sensors that operate in the microwave region of the electromagnetic spectrum. The wavelengths at which SAR systems operate (from centimeters to meters) offers the advantage of high spatial sampling and wide area coverage regardless of the cloud cover or sun illumination conditions. SAR has therefore been a valuable resource for both land and oceanic applications. On land, SAR data has been successfully used in research and operational workflows across multiple fields: geology, agriculture, natural hazards assessment, forestry, urban and infrastructure monitoring being some of the most common examples. Offshore, marine environmental monitoring and ocean surveillance are just two of the many uses of SAR data. In this regard, SAR data has been traditionally used in the analysis of metocean phenomena (e.g. internal waves (Apel, 2004), surface circulation (Lyzenga *et al.*, 2004) or sea-ice (Pichierri and Rabus, 2018), monitoring marine traffic (Pichel *et al.*, 2004) and surface slicks (Alpers and Espedal, 2004)).

In marine waters, wind stress creates surface roughness which translates into a short and a long wave spectrum, and the presence of oil affects both. Periodic short surface waves travelling towards or away from the radar sensor, with a length comparable to the radar wavelength, act to scatter some of the radar signal back towards the sensor, a mechanism described as Bragg scattering (Holt, 2004); the primary mechanism for backscattering radar pulses (Valenzuela, 1978). The strength of the signal reflected by a surface is represented in terms of its brightness in a radar amplitude image. Hence, due to its roughness, the water surface will appear radiant (Holt, 2004). However, oil slicks, independent of their origin, manifest as dark features against the luminous surrounding environment in an amplitude image. This is because hydrocarbon fluids are interacting with the smaller scale waves by dampening them (Holt, 2004; Brekke and Solberg, 2005) through what was described as the Marangoni Effect

(Hühnerfuss *et al.*, 1983; Girard-Ardhuin *et al.*, 2003). Capillary and shortgravity waves (i.e., short surface waves driven by the effects of surface tension and gravity) produced by wind stress at liquid surfaces have regular transverse motion. Areas covered by oil experience a change in visco-elastic properties producing a difference in the surface stress gradient, opposing normal dissipation patterns, and creating longitudinal motion. Dampening of the high frequency ripples occurs when the two kinds of waves are in resonance and is controlled by the nature, density and viscosity of the film layer (Girard-Ardhuin *et al.*, 2003). Natural hydrocarbons resulting from seepage usually create thin, monomolecular layers, whereas thick crude oils, fuels and other derivatives will coat the surface differently and introduce further changes in the dampening process. This latter process is still a subject of ongoing debate (Migliaccio *et al.* 2005). However, a consensus exists that when microwave pulses transmitted by the SAR instrument are incident upon the flattened area, the Bragg scattering mechanism is inhibited, which translates into a dark patch delineating the oil slick on a SAR image.

Due to the distinct contrast between the open sea and an oil slick, SAR imagery has been extensively exploited in semi-automatic operational workflows for oil slick detection and mapping (Solberg *et al.*, 1999; Girard-Ardhuin *et al.*, 2003; Keramitsoglou *et al.* 2003; Brekke and Solberg, 2005; Solberg and Brekke, 2008). Slick identification on SAR data is highly dependent on the exact air-sea conditions pertaining during the acquisition, the SAR system configuration and position and the performance of the detection algorithm. The latter of these relies on the ability to recognize slick-like structures and correctly classify them as of hydrocarbon nature against similar surfactant slicks. In many cases – particularly within the oil industry – this task is performed manually through expert interpretation, owing to the challenges of implementing automated algorithms and a degree of ambiguity about their efficacy in being capable of detecting the subtleties of oil spill phenomena. Nonetheless, manual interpretation can be laborious when mapping slicks spanning large areas and somewhat subjective, and so progression towards a more reliable, automated, and objective processing chain has long been sought and debated within the scientific community.

A semi-automatic workflow involving the use of single-polarized SAR data from ERS-1 was proposed by Solberg *et al.* (1999) and has been adopted as a standard algorithm for operational processes and research. The procedure involves basic image processing steps that make use of local statistics. Several subsequent studies retained the same processing steps (pre-processing, dark feature extraction, classification and analysis) but have suggested various improvements (Brekke and Solberg, 2005; Solberg and Brekke, 2008; Suresh *et al.*, 2015). A key step in the workflow is the initial image pre-processing performed in preparation for segmentation, which comprises geometric and radiometric calibration and, importantly, image enhancement.

Due to the coherent nature of SAR imagery (Migliaccio *et al.*, 2005), images are affected by speckle ‘noise’, inducing a grainy appearance and introducing a large backscatter variation even over homogeneous areas. The ‘salt and pepper’ effect, generated by the interference of echoes returning from individual scatterers (e.g., ocean wave geometries) within a resolution cell (Woodhouse 2017), diminishes the quality of the image. This alternating pattern of dark and bright pixels affects the performance of computer vision algorithms, with dark pixels often classified and grouped as pertaining to a dark formation, regardless of their distribution across the scene. Images in which the speckle effect has been mitigated present a much better distribution of the pixel values, similar to a smoothing or blurring operation, where the granular variability has been reduced. This can facilitate the grouping of pixels with similar values into contiguous dark objects or regions within an image. Therefore, successful pixel clustering and

extraction of dark formations through segmentation is highly dependent on effective suppression of this speckle artefact during the image enhancement pre-processing stage.

The published literature presents a wide variety of speckle filtering techniques applied to SAR imagery, while also examining their efficiency (Argenti *et al.*, 2013). However, the performance of such filters is generally assessed using synthetic images or simulated SAR images. The absence of ground-truth data means that these studies provide only an approximate estimation of the practical efficiency of speckle filters. In reality, SAR data displays a great radiometric and geometric complexity that cannot be fully recreated artificially. Frequently, after an initial analysis on artificial imagery, the same despeckling methods are also applied to real SAR acquisitions (Mansourpour *et al.*, 2006; Nezry, 2014; Kupidura, 2016). Very few such studies, however, perform assessments on scenes acquired over marine environments. While the speckle principle remains the same, the variations induced by the distributed presence of local scatterers does provide a distinct noise reflectivity pattern.

Furthermore, studies related to oil slick detection rarely justify their decision to opt for a particular speckle filter over other candidates. Accordingly, common practice in the literature tends to dictate the choice of filtering technique employed in many other studies. The general consensus is that the filter should be able to effectively smooth large homogenous areas, retain edges and linear features and, most importantly, not alter image statistics significantly. Methods that have frequently exhibited these characteristics in the literature are often presumed to be viable candidates in any case. However, this may not necessarily be a valid assumption, especially given that every scene is unique in terms of the air-sea conditions and SAR imaging configuration at the time of acquisition.

Another factor that requires consideration is the implementation of a given despeckle filtering algorithm across the various software packages and toolboxes widely utilized for SAR image processing. Whilst it could be assumed that this is consistent, subtle differences in the coding of the algorithms are likely between different programming languages. Therefore, the failure to perform a prior assessment of a method could result in substandard despeckling performance, which will ultimately affect the oil slick detection capability.

This study offers a review of the use of a series of common speckle filtering algorithms over a set of real SAR images containing confirmed natural marine oil slicks. The objective is to provide a quantitative assessment of their effectiveness in suppressing speckle and recommendations on which filters to adopt. To the best of our knowledge, only a handful of studies have approached this application from the perspective of speckle filtering efficiency (Bharaneswari *et al.*, 2015). Specifically, a study by de Souza *et al.* (2006) appears to be the only previous attempt to provide a brief assessment of speckle filter behavior when applied to SAR data containing oil slicks.

In this analysis, the performance of despeckling is assessed only over incoherent SAR data, where the expression of noise is found in the amplitude or intensity information. Methods pertaining to the use of polarimetric SAR are beyond the scope of this study, although polarimetric oil slick detection techniques have received attention in recent years (Migliaccio *et al.*, 2015); comprehensive reviews on the effectiveness of these techniques are provided elsewhere (Touzi and Lopes, 1994; Jong-Sen Lee *et al.*, 1999, 2009; Lee and Pottier, 2009). A selection of speckle filters is presented, together with their literature sources and performance metrics. The selection is based on a wide spectrum of definitions as reported in Argenti *et al.* (2013) and a review of the oil spill detection literature. The chosen set of filters captures the

diversity in the different types of filters available and permits the timely comparison of classical filters alongside more modern and complex approaches to evaluate the benefits they may offer. The despeckling procedure on two separate datasets (Normalized-Radar Cross Section (NRCS) and digital number (DN) intensity) and performance metrics are presented. The results are discussed with respect to these performance metrics and a visual analysis.

DESPECKLING METHODS

Speckle manifests itself as the distinctive “salt and pepper” appearance on SAR imagery. The effect is caused by the presence of multiple elementary scatterers generating electromagnetic fading within a single SAR resolution cell. Goodman (1976) explains how the distance between the surface scatterers induced by surface microscopic roughness (i.e., at wavelength scale) and the SAR system can be translated into a coherent transmission of frequency, but a loss of phase coherence. When the returned echoes combine constructively the signal is amplified, and conversely, if the waves are out of phase, the signal strength decreases. The pixel-by-pixel variation in signal intensity is translated into speckle.

In the case of marine surfaces, phase decorrelation is caused by the random change of surface scatterers, the position of the instrument with respect to the illuminated cell area, and the amplitude of each generated wave, which is also dependent on the surface characteristics. In general, the speckle model can be described either in relation to the phase or to amplitude/intensity, both of which are polarimetric properties. Here, we consider the single polarization multiplicative model (Figure 1).

The hypothesis is that a single resolution cell contains a random distribution of many scatterers (Woodhouse, 2017). In this case, the real (Re, z_i) and imaginary (Im, z_j) components of the return SAR signal are Gaussian distributed. The mean is zero and the variance is $m/2$, where m is determined as the average between the individual amplitudes/intensities of each scatterer. Oliver and Quegan (2004) propose a normal probability distribution function (PDF), P , used to approximate the probability of the z_i and z_j values to occur at any point location (Equation 1):

$$P(z_i, z_j) = \left(\frac{1}{\pi m}\right)^{\frac{z_i^2 + z_j^2}{m}}, \quad (1)$$

If the result of P is 1, the phase angle is uniformly distributed and all the real and imaginary z values are equally likely to occur, with any amplitude, $A \in [0, \infty]$. In the case of SAR scenes acquired over land, A follows the Rayleigh distribution (Equation 2) that is defined by the diffuse scattering model (Ulaby and Lang, 2014):

$$P(A) = \frac{2A}{m} e^{-A^2/m}, \quad A \geq 0 \quad (2)$$

Since the intensity (I) is the square-root of the amplitude, the value of I can be easily retrieved (Equation 3):

$$P(I) = \frac{1}{m} e^{-I/m}, \quad I \geq 0 \quad (3)$$

As the intensity varies exponentially towards 0, the mean and the standard deviation are both equal to m . Since m is the expression of the power, it can be translated as the power radiated from one target and, when averaged, referred to as the radar cross-section (RCS) (Nezry, 2014; Woodhouse, 2017). The RCS will give the value of the target pixel when the SAR image is constructed. To understand speckle distribution, knowledge about the power is essential. However, since the distribution of the intensities is not Gaussian, but skewed following the scattering model, the power estimation has a 0-100% uncertainty signifying a large variation (Oliver and Quegan, 2004).

Ocean speckle mechanisms differ from that for standard land scenes described above. Instead, the scattering characteristics over the ocean are explained by the joint contribution of the short and long wave spectrum. In this particular case, the K-distribution model is more convenient, fitting the theoretical framework of wind-wave relationship and induced electromagnetic scattering interaction (Migliaccio *et al.* 2019). At ocean level, a SAR resolution cell covers an area comparable to the scale of long waves, therefore, the measured intensities are combined contributions of small- and large-scale roughness. Since the marine surface is in constant dynamic, the number of scatterers varies randomly, causing variability in the observed RCS values due to minute changes in geometric configuration and radiated power. It is already known that the RCS follows a negative exponential distribution model (Equation 3), explicitly, the gamma-distribution. Hence, the scattered coherent radiation is K-distributed (Equation 4) for explaining the randomness of the intensities (Redding, 1999).

$$P(I) = \frac{2}{\Gamma(\nu)\mu^{\nu+1}} \nu^{\frac{\nu+1}{2}} I^{\frac{\nu-1}{2}} K_{\nu-1} \left(\frac{2}{\mu} \sqrt{\nu I} \right) \quad (4)$$

Here, the $K_{\nu-1}(\cdot)$ is the modified Bessel function of the second order of $\nu - 1$, used here for explaining the radar signal model, ν is the shape parameter which explains the non-Gaussian distribution of intensities, $\Gamma(\cdot)$ is the Gamma density function and μ refers to the backscatter mean local variance.

To reduce the variation, the spatial distribution of the independent target measurements must be equalized. While a simple moving window averaging the various measurements may appear sufficient, the precision of it is not sufficient. As the window is moved around the image, different targets measurements might be cumulated, resulting in erroneous values, and reducing the spatial resolution. An elegant manner for overcoming this issue is to apply a procedure specific to SAR systems known as multilooking (Franceschetti and Lanari, 2018), prior to pixel ground detection.

Multilooking takes advantage of the multiple “sub-apertures” that synthetically compose the full aperture of the SAR. Each “sub-aperture” will register a different measurement of the same target in the radar cell at a reduced azimuth resolution, which will be reconstructed into a single value composed of multiple “L-looks”. In this manner, same-cell retention is guaranteed. “L-looks” are recomposed incoherently over the amplitude only, this time. The incoherent average is not dependent on the phase angle; thus, it will allow the estimation of the amplitude and intensity value without considering the phase shift.

While multilooking is an effective step for mitigating the speckle present in a SAR image, the trade-off is still a reduction in spatial resolution, which will be degraded by the same number of

looks. To compromise, multilooking is often performed with a lower number of looks as a pre-processing step.

To further reduce the variability of speckled images, other methods requiring incoherent averaging may follow an initial application of multilooking on Single Look Complex (SLC) images. However, SLC SAR data processing results in a change in the speckle model such that it no longer follows the initial electromagnetic fading model. Therefore, speckle noise can instead be treated as a spatial variation of reflectivity of the illuminated surfaces (changes in brightness and contrast), rather than a spatial distribution of coherent signal returns.

In practice it is convenient to describe power distribution using a multiplicative noise model (Lee 1980, 1981) as:

$$z(i, j) = x(i, j) \times v(i, j), \quad (5)$$

where $z(i, j)$ is the amplitude/intensity power of the SAR image for a given image pixel, $x(i, j)$ is the reflectance value of the pixel and $v(i, j)$ is the estimated noise.

The main objective of speckle filtering is to create a denoised image with enhanced amplitude/power and suppressed noise, without sacrificing any of the information content. The ideal method should smooth in homogenous areas and preserve boundaries of structural elements and textural (fine-detail) patterns (Lee *et al.*, 1994; Nezry, 2014). For marine surfaces with oil slicks, the key requirements target the smoothing efficiency and edge and fine-detail retention.

Reviews of generic speckle filters used for denoising SAR images are provided by several authors (Lee *et al.*, 1994; Zhenghao Shi and Fung, 1994; Touzi, 2002; Argenti *et al.*, 2013; Li *et al.*, 2018). Specific novel filters not covered by the reviews are typically presented in standalone studies. These filtering techniques are constructed using different combinations across different signal domains for speckle estimation, such as in the spatial, homomorphic or wavelet space (Argenti *et al.*, 2013).

Research involving oil spills should consider the specifics of marine spatial speckle, which are explained for the polarimetric case by Gambardella (2007), but can be reduced to the single-look case. Based on an extensive review of the literature, the following filtering techniques were identified as being amongst the most commonly utilised: only multilooking (Leberl, 1990), the Enhanced Lee Filter (Suresh *et al.*, 2015), Lee filter and a custom morphological filter (Gasull *et al.*, 2002), Lee filter (Brekke and Solberg, 2005; de Souza *et al.*, 2006), Median filter (Mera *et al.*, 2012), and a succession of Lee filters and Median filters (Karathanassi *et al.*, 2006). From this it is evident that filters applied in the spatial domain are the most preferred.

This study aims to provide a comprehensive evaluation of the performance of a diverse array of different types of filters. These chosen filters were selected with the following criteria in mind:

1. Classical filters: classical techniques that have been widely described and applied in the published literature (e.g., Lee Filter, Enhanced Lee Filter, Median filter, Frost Filter, Gamma Map).
2. Refined filters: filters that have undergone subsequent refinement and has improved in comparison to the original version (e.g., Enhanced Lee Filter, Refined Lee Filter, Enhanced Frost, Lee Sigma).

3. Emerging filters: new and emerging filters that reflect recent developments in the field (e.g., SRAD, Bilateral filtering, SAR-BM3D, i-DWT).
4. New filters applied to ocean applications: techniques that, to the best of the authors knowledge, have not yet been assessed in relation to ocean applications (e.g., SAR-BM3D, Guided Filter, SRAD, i-DWT)
5. Accessible filters: widely accessible filters that are commonly implemented in standard SAR processing software/toolboxes (e.g., Lee filter and variations, Frost filter, Gamma Map).
6. Non-Bayesian filters: filters that expand the diversity beyond the abundance of techniques based on Bayesian statistics in the spatial domain (e.g., Bilateral, Guided filter, SAR-BM3D, SRAD).

Eleven of the filters chosen for comparison in this study operate in the spatial domain using Bayesian statistics. Eight of those use linear statistics for estimating noise levels and approximate intensities (one simple: Median; seven complex: Lee, Lee Sigma, Enhanced Lee, Refined Lee, Frost, Enhanced Frost, Gamma Map), whereas one is defined using a non-linear approach (Symmetric Nearest Neighbor). To enhance the diversity and include contemporary methods, three common non-Bayesian filters were also considered (Speckle reducing anisotropic diffusion – SRAD, Bilateral filtering, Guided Filter). For enhanced comprehensiveness, a filter operating in the transform domain, SAR Block Matching 3-D (SAR-BM3D), a recent and popular multi-resolution method, was chosen for comparison. SAR-BM3D is based on integrating wavelets and non-local weighted averaging. Finally, a hybrid Improved Discrete Wavelet Transformation (i-DWT) using an implementation proposed by Choi and Jeong (2019) was selected for demonstrating the capabilities of combined approaches in the frequency domain.

Bayesian methods in the spatial domain (filters based on linear statistics)

Median filter

The Median filter is a simplistic local-statistical technique that does not account for the distribution of speckle. A moving window replaces the value of the center pixel with that of the median value of all the surrounding pixels in the kernel. The filter has a good smoothing capability but is rudimentary when encountering edges. Small windows provide considerable edge smoothing and fine-detail loss with little speckle removal (Woodhouse, 2017).

Lee filter and Lee Sigma filter

The original Lee filter (Lee, 1980, 1981) utilizes the statistical distribution of values in a local moving window for estimating the value of the center pixel. An assumption is made that the distribution of noise will be Gaussian. The center pixel (DN_{in}) is replaced with a new value (DN_{out}) based on the mean and variance of surrounding kernel pixels (Equation 6):

$$DN_{out} = \mu + K(DN_{in} - \mu),$$

$$K = \frac{Var(x)}{\mu^2\sigma^2 + Var(x)} \quad , \quad (6)$$

where μ is the mean of the moving window pixels (x), σ is the standard deviation and $Var(x)$ is the variance of pixels within the window. The K factor represents a weighting factor. An advantage of the Lee filter is that it can preserve edge sharpness while suppressing noise.

The Lee Sigma filter (Lee, 1983) also assumes a Gaussian distribution of noise, but unlike the Lee filter, the presumption is that the samples will fall within 95% of a two standard deviation range (Mansourpour *et al.*, 2006). An improved version of the Lee Sigma filter has been proposed by Jong-Sen Lee *et al.* (2009).

Enhanced Lee filter

The Enhanced Lee filter represents an adaptation of the Lee filter, as presented by Lopes *et al.* (1990). Similarly, it uses local statistics within a moving window, where local heterogeneity in the image is classified according to three possible scenarios:

1. The area is homogenous, and the center pixel value is replaced by the average in the filter window.
2. The area is heterogenous, and the new value of the center pixel is replaced by the weighted average in the filter window.
3. An area defined by a point target where the initial value of the pixel is preserved.

Refined Lee filter

The Refined Lee filter is different from the Enhanced Lee filter. The Refined Lee Filter (Lee and Pottier, 2009) uses a method adapted to utilise larger moving windows, a computational requirement that was difficult to achieve when the Lee filter was first proposed. The window used by the Refined Lee filter is non-square, but adapted to fit multiple directions (vertical, horizontal and diagonal) across the four possible axes of an image. This adaptation provides an increased capacity for detecting edges. Eight possible edge-masks are described in Equation 7.

$$\begin{aligned}
 & \begin{bmatrix} -1 & 0 & 1 \\ -1 & 0 & 1 \\ -1 & 0 & 1 \end{bmatrix} ; \begin{bmatrix} 0 & 1 & 1 \\ -1 & 0 & 1 \\ -1 & -1 & 0 \end{bmatrix} ; \begin{bmatrix} 1 & 1 & 1 \\ 0 & 0 & 0 \\ -1 & -1 & -1 \end{bmatrix} ; \begin{bmatrix} 1 & 1 & 0 \\ 1 & 0 & -1 \\ 0 & -1 & -1 \end{bmatrix} \\
 & \begin{bmatrix} 1 & 0 & -1 \\ 1 & 0 & -1 \\ 1 & 0 & -1 \end{bmatrix} ; \begin{bmatrix} 0 & -1 & -1 \\ 1 & 0 & -1 \\ 1 & 1 & 0 \end{bmatrix} ; \begin{bmatrix} -1 & -1 & -1 \\ 0 & 0 & 0 \\ 1 & 1 & 1 \end{bmatrix} ; \begin{bmatrix} -1 & -1 & 0 \\ -1 & 0 & 1 \\ 0 & 1 & 1 \end{bmatrix} \tag{7}
 \end{aligned}$$

An original fixed 7x7 (or greater) window is defined with this filter, although when applied, the window is subdivided into 3x3 sub-windows where the mean of each is computed. The reconstruction of the original window enhances the weighting of pixels closer to the center pixel.

Frost filter and Enhanced Frost

The Frost method (Frost *et al.*, 1982) is similar to the Lee filter in that it also possesses capabilities for edge preservation. In this method, a circular kernel is used instead of a square one. The pixel's gray level or intensity is estimated by computing the weighted sum of the center

pixel value, and the mean and variance within the kernel. Unlike the Lee filter, the Frost method does not use a simple linear weighted expression.

The Frost filter is defined as:

$$P(i, j) = \frac{\sum_i \sum_j p_{i,j} k_{i,j}}{\sum_i \sum_j k_{i,j}}, \quad k_{i,j} = e^{-K C_I^2 d_{i,j}}, \quad (8)$$

where $P(i, j)$ is the value of the center pixel with the positional attributes i and j , k is the weighting factor, C_I is the coefficient of variation and d is the distance between pixels in the kernel window, centered on the center pixel. Small values of k indicate good speckle suppression but a loss in detail. A greater k will reduce the efficiency in smoothing but retain texture and edges.

An enhanced version was also described by Lopes *et al.* (1990) following a similar rationale as that for the case of the Enhanced Lee filter.

Gamma Map

The Gamma Maximum A Posteriori (Γ -MAP; Gamma Map) filter developed by Lopes *et al.* (1993) is based on the idea that when the radar reflectivity undergoes significant variation due to a large distribution of scatterers and complex structure, linear local statistics computed using a moving window are not sufficient. Whereas previous filters assumed a Gaussian distribution of values, the Gamma Map filter is based on a Gamma distribution. In SAR scenes that have been previously multilooked, the Gamma Map filter is expected to perform better. The filter combines a hybrid approach of calculating the local mean and variance statistics in a moving window and replacing the center pixel's value where needed and employing a second geometric assessment across edges along the four possible directions (similar to the Refined Lee filter). The Gamma Map filter was originally defined to meet the three class division criteria (homogeneity, heterogeneity and point target preservation), hence it is by itself an "enhanced" method.

Bayesian methods in the spatial domain (filters based on non-linear statistics)

Symmetric Nearest Neighbor (SNN)

The SNN filter (Hall, 2007) is a non-linear technique that has been designed specifically for edge preservation. A moving window is moved across the image, and at each position symmetric pixel-pairs are computed around the central pixel. A comparison between each pixel-pair and the central pixel is performed and the closest value to the center pixel is saved. The resulting value of the center pixel is computed by using a sum of all of the closest values. The SNN filter originated as a method for smoothing seismic acquisitions, therefore, it assumes that there is a coherent signal model.

Bayesian methods in the transform domain

Improved Discrete Wavelet Transform (i-DWT)

Gagnon and Jouan (1997) provide a comprehensive assessment of the capabilities of several 2-D wavelet filters and their performance compared to a standard spatial-defined technique. On the contrary, Hervet *et al.* (1998) argue that while the wavelet-based methods exhibit several advantages over global spatial filters, adaptive spatial despeckling achieves better results. Nevertheless, when combined with other methods, wavelet transformation can yield similar promising results.

A series of filtering methods based on discrete wavelet transform (DWT) in the homomorphic space are considered here for their complexity and potential efficiency. The rationale behind using a DWT method is that it can analyse signal positioning in both the frequency and time domains. Filters that incorporate wavelet transformation and edge preserving methods are common (Rosa-Zurera *et al.*, 2007; Choi and Jeong, 2019).

In this study, the Improved DWT (i-DWT) filter (Choi and Jeng, 2019), which is an enhanced algorithm using a succession of filtering steps, is utilized with some adjustments. The input images are initially denoised using a speckle reducing anisotropic diffusion (SRAD) filter (Yu and Acton 2002). Multilevel wavelet decomposition is then performed on the resulting images. Daubechies wavelets are shown to produce desired outcomes, however, any other suitable fitting-function can be used for approximating the signal fluctuations (Leguizamón, 1997; Argenti *et al.*, 2013). Choi and Jeong (2019) do not specify the wavelet method used in their algorithm, so in this case an arbitrary wavelet (the Haar wavelet in Pywavelets (Lee *et al.*, 2019) has been chosen based on a best-fit analysis. Haar (also known as Daubachies 1 or db1) is a simple wavelet constructed as a sequence of rescaled 'square-shaped' functions that adapt well to sudden transitions in the signal. The SRAD image noise is multiplicative. For the wavelet to adapt correctly, the noise model has to be readjusted to an additive format. A simple logarithmic transformation is applied for this purpose.

Wavelet transformation uses a scale parameter and a shift parameter to create a time-frequency sliding operator. The scale parameter modulates the compressions and expansions of the width of the wavelet, without affecting its structure. Larger amplitudes of the signal generate larger widths of the wavelet. When the amplitude is low, high-frequency components can be isolated. The shifting component determines the slide, namely the position of the wavelet on the time axis. A sparse representation containing low and high frequency information is stored in distinct coefficients (Mallat, 2009). The number of coefficients fluctuates depending on the level of decomposition applied. For a 2-D iteration, there will be 8 coefficients. The first step produces an approximation image of the original input, containing the low-frequency information (LL1) and three coefficients that encompass the high-frequency information on the vertical (LH1), horizontal (HL1) and diagonal (HH1) axes. On the second iteration, the approximation image LL1 is further decomposed in a similar fashion, resulting in the LL2 low frequency approximation and the LH2, HL2, HH2 high-frequency coefficients. Each step reduces the length of the original signal by half.

The majority of the noise is retained in the high-frequency sub-bands. Smoothing is performed on the vertical and horizontal sub-bands (which have similar low energy) using a soft threshold, reducing the effect of abrupt peaks resulting from absolute values and preserving the original signal. The diagonal and approximation sub-bands are smoothed using a Guided filter. Choi and Jeong (2019) propose an improved version of the Guided filter, however, in this implementation the original filter is preferred. The Guided filter is employed in order to retain the low and high frequency components at edge level. A 2-D wavelet-reconstruction of the image is performed using an inverse wavelet decomposition with the Haar wavelet. Finally, an exponential function

is applied to convert to a multiplicative noise model and the despeckled image is produced. The algorithm is documented in Figure 2.

Non-Bayesian methods

Bilateral

Contrary to most of the previously outlined methods, the bilateral filter uses non-linear statistics (Tomasi and Manduchi, 1998). The technique is known for its good edge preservation and noise reducing smoothing. The filter does not use a sliding window, but it can be applied iteratively. The intensity of each pixel is replaced by a weighted average of the intensity values of the surrounding pixels, as controlled by the spatial and radiative ranges (Equation 9). A notable aspect of this filter is that at edge level, differences in contrast (spikes in intensities) will be treated as similar. The filter is dependent only on the size of the moving window and the contrast between encountered features.

$$BF[I]_p = \frac{1}{W_p} \sum_{q \in S} G_{\sigma_s(\|p-q\|)} G_{\sigma_r(\|I_p - I_q\|)} I_q$$

$$W_p = \sum_{q \in S} G_{\sigma_s(\|p-q\|)} G_{\sigma_r(\|I_p - I_q\|)} \quad (9)$$

where σ_s and σ_r represent the amount by which the Gaussian function (G) is adjusted in the spatial and range dimensions, respectively. The spatial extent is given by the positions of the center pixel (p) and the adjacent pixels (q) of the image (I). As σ_r increases, the bilateral filter (BF) becomes a Gaussian filter, averaging by a constant. Increasing σ_s will result in smoothing larger areas. Since the weights (W_p) are multiplied, the balance between the effects of fluctuating Gaussians forces the edge preservation (Paris *et al.*, 2007). The limitations of the bilateral filter arise when the edge complexity is too high, resulting in gradient reversal.

Guided Filter

The Guided filter was developed by He *et al.* (2013) as an improvement to the Bilateral filter. According to the authors, the method possesses enhanced edge retention capabilities. The Guided filter offers an iterative method that implies the use of a “guide” image for matching the edges of the original input image. The “guide” can be created using high pass filters or can be defined as the original input image itself. A linear relationship exists between the guide and the input. A regression model is applied for suppressing noise and maintaining edges. This capability was confirmed through experiments conducted by He *et al.* (2013).

Speckle reducing anisotropic diffusion (SRAD)

Anisotropic diffusion filters are based on the partial differential equation delivery of non-linear diffusion for smoothing. The principle accounts for the generation of multiple structure-matching

gradients that change throughout the image iteration, hence large-area blurring and edge retention is possible. The speckle model that the technique assumes is that of coherent noise, therefore, SRAD can be matched with SAR images. SRAD gradients are built using the instantaneous coefficient of variation and a series of Laplacian operators for edge and detail isolation. A full description of the algorithm is provided by Yongjian Yu and Acton (2002). A shortcoming of SRAD is the unrealistic appearance of images after smoothing, meaning that fine detail might be lost without a prior fine tuning of the parameters.

Non-local methods

SAR-Block-Matching 3-D filter

The structure of the block-matching 3-D filtering algorithm was proposed by Parrilli *et al.* (2012). The despeckling method is based on the combined concepts of non-local filtering (NL) and wavelet filtering. The first operations utilize a NL approach, which implies that throughout images, a repetitive representation of the signal can be found. Once these homogeneous patches are identified, only these regions are smoothed. This process involves the creation of “blocks”; aggregations of pixels with similar brightness formed using the Euclidian distance criterion. Furthermore, each block undergoes a wavelet filtering and, in converse to i-DWT, a hard thresholding of the high frequency coefficients. Blocks are rearranged to their original location. The same step is repeated, but this time the wavelet transformation can differ, and hard thresholding is replaced by a Wiener filter. The final image will consist of the newly recomposed blocks.

The downside of BM3D is that it is suited to additive noise, whereas SAR noise is treated as multiplicative. Therefore, an adapted method has to be used (SAR-BM3D). Whereas i-DWT uses a homomorphic approach by simply converting the multiplicative noise using a logarithm function – which has the disadvantage of modifying the dynamic of the data – BM3D forces noise conversion through the use of a locally adaptive linear minimum mean squared error.

Other types of filter

New and emerging methods for speckle filtering use convolutional neural networks for estimating the quantity of noise. These techniques are not yet well-established and have only been reported in recent studies. They usually require large computational resources and, although they often achieve superior results when compared to traditional methods, the resource consumption is not yet compatible with the needs of an operational fast model design (Wang *et al.*, 2017; Lattari *et al.*, 2019; Zhang *et al.*, 2020). For this reason, they are not included in this comparative study.

METHODOLOGY

Assessing and validating the performance of speckle filters is a challenging task when applied to real SAR imagery. SAR scenes provide a noisy image input within which the real noise reflectivity that we wish to quantify is unknown, which makes estimating the ground-truth impossible (Argenti *et al.*, 2013; Zhang *et al.*, 2020). Typical performance assessment

approaches use a sample noise-free dataset of non-SAR imagery to which noise is added synthetically and then a despeckling filter applied. This practice allows for the control of the speckle patterns introduced and a straightforward case for inspecting smoothing and edge and texture preservation.

In this study, the intention is not to evaluate the intrinsic performance of speckle filters, but to assess their specific capacity to perform denoising of SAR data acquired over marine surfaces where natural oil slicks are present. In theory, a simulated SAR image can be used to mimic a real SAR acquisition. However, dynamic sea conditions can substantially change the noise reflectivity pattern, hence the statistical properties chosen for the simulated image will differ from the actual ground-truth. Consequently, to capture the true sea conditions, the speckle filters are applied to real SAR imagery.

Dataset

Five Copernicus Sentinel-1 High resolution, Level-1 Ground Range Detected (GRD) SAR scenes in interferometric wide (IW) swath mode were selected, covering two different locations at multiple time points in order to capture a range of dynamic sea conditions. The original 20 m x 22 m scene resolution in range and azimuth, as reported in the Sentinel-1 Product definition (Collecte Localisation Satellites 2016), was maintained for each scene. All scenes were subset to preserve only the vertical transmitted-vertical received (VV) polarization.

The scenes cover areas in the Black Sea, where known persistent and productive natural seepage activity has been well documented (Körber *et al.*, 2014). These areas are portrayed in Figure 3 as '1' the coastal area of the town of Çayeli (Turkey) – the Rize oil seep; and '2' the area of the Kobuleti Ridge (off-shore Georgia), where the Colkhети and Pechori sea mounds provide a cluster of natural oil seeps. The Sentinel-1 SAR data were acquired in ascending and descending modes and on different dates in order to provide sufficient variability in the sea surface conditions (Table 1). Each image was sampled separately, and four regions of interest (ROI) were created: one including the outline of the known seep slick, one including faint slick-like structures, and two homogenous areas where the incidence angle varies with the SAR view (Figure 4). The ROIs were subset to localised areas in order to focus on the characteristics of important slick/dark structures, and as a trade-off between computational requirements and processing time associated with extensive experimentation using the array of filters. Nonetheless, whilst expanding the size of the area to a full scene increases the processing time and the computational requirements, initial tests indicated that this does increase the performance of the results due to a larger statistical sample size.

Pre-processing

Data was pre-processed using the existing well-established workflow of Suresh *et al.* (2015), as depicted in Figure 5. The workflow was chosen for its design, which allows the exploitation of a SAR acquisition in two distinct manners: as grey-level estimation (DNs) and radiometrically calibrated data (NRCS). Therefore, the effects of speckle filtering over the two common types of pre-processed images (radiance and "reflectance") can be assessed. First, precise orbit ephemerides were applied for accurate orbit determination and correcting geo-positioning anomalies. It is to be noted that speckle levels are already reduced through an initial multilooking process during the SLC (Single Look Complex) to GRD conversion (Collecte Localisation Satellites 2016). Next, the two approaches for pre-processing were followed:

1. Grey-level estimation – where resulting pixels contain real SAR numbers (digital numbers).
2. Normalized radar cross section estimation – where the amplitude and intensity levels are computed.

The resulting ROIs were divided into images where reflectivity information is described by digital numbers (DN) and images where the normalized radar cross-section (NRCS) was outputted after radiometric calibration. The goal was to analyze how denoising performs when applied to each case, as a next logical step towards future optimized algorithm development.

Filtering

Various speckle filters are available in numerous variants in SAR processing software or as freely distributed code packages. To enhance the accessibility and wider implications of the study, the most common implementations of the despeckling methods were used. Hence, for this processing, two popular open platforms were utilised: the Sentinel Application Platform (SNAP) and the Python programming language. The preference was placed on SNAP since it already has most of the filters implemented and it is arguably more widely accessible as no programming experience is required.

The speckle filters were applied by maintaining the same parameters over all image ROIs. An initial evaluation of code implementations in SNAP v.7.04 (SNAP - ESA Sentinel Application Platform v7.0.4 n.d.) was performed to ensure compliance with their original definition. The Java implementation in the Sentinel-1 Toolbox (component of SNAP) was compared to the filter's mathematical body in the definition paper. If the algorithm was respected, the filter was considered to be correct. However, this evaluation revealed that whilst the majority of the filters offered in SNAP were correctly implemented, a popular choice, the Lee filter was corrupt in that it was not functioning as expected. The Gamma Map, Frost, Median, Lee Sigma (v. 2009) and Refined Lee were applied using SNAP, which is provided as free and open software by the European Space Agency.

The remaining filters, including the corrupt Lee filter, were implemented independently using a Python 3.7 version in an Anaconda v.4.8.3 distribution custom environment. Python-based filters were coded following the original source manuscript or by using embedded library functions (Bradski, 2000; Bianco *et al.*, 2020; SciPy 1.0 Contributors *et al.*, 2020) and openly distributed independent implementations (e.g., SAR-BM3D by Makinen *et al.* (2019)).

A generic moving window size of 5x5 was maintained where appropriate, although the Refined Lee filter inherently uses a 7x7 kernel. Other filters, such as the Guided filter, SAR-BM3D and the i-DWT estimate appropriate kernel sizes. Various computation parameters specific to each method were trialed beforehand. The trials were run individually in order to select the values that provide the optimum result for every filter. The selected parameter values allow for a trade-off of computational performance and changes in the statistical variation of the values within each moving kernel. Generally, a 5x5 moving window was found to be ideal in producing a sufficient degree of smoothing whilst ensuring edge retention. A final list of the respective parameters is provided in Table 2.

Performance Assessment

In order to evaluate the performance of the speckle filters, a set of complementary quantitative metrics were selected. These were chosen specifically to evaluate the despeckling process, based on a review of popular, well-established indices (Mansourpour *et al.*, 2006; Argenti *et al.*, 2013; Choi and Jeong, 2019). These indices can be divided into “with-reference indices” – typically used with a reference image that is previously known and “without-reference indices” – that do not require *a priori* complete knowledge of the reflectivity (Argenti *et al.*, 2013). The chosen methods (described below) estimate the statistical effects of noise over the image structure, the global performance of the filter and the capability of the denoising technique to smooth over homogeneous areas and retain edges. The selection combines “with-reference” and “without-reference indices” as a means to ensure that the effects of each filter can be rigorously assessed.

Peak Signal to Noise Ratio (PSNR)

The Peak Signal-to-Noise Ratio (PSNR) (Walessa and Datcu, 2000) evaluates the qualitative properties of the denoised image and the ground-truth image using the Mean Squared Error (MSE) (Equation 10). The error quantifies the amount by which the values in the original image differ from the noisy image. PSNR is defined as the ratio between the maximum possible value (power) of a signal and the power of the noise (Equation 11). The signal has a wide dynamic range; therefore, the ratio values are adjusted using a logarithmic scale (dB). Larger PSNR values imply a better despeckling capability.

$$MSE = E(\hat{f} - f)^2 \quad (10)$$

$$PSNR = 10 \times \log_{10} \left[\frac{var[f_{PEAK}^2]}{MSE} \right], \quad (11)$$

where f and \hat{f} are the original and the despeckled image, respectively, f_{PEAK} is the maximum value that can be attributed to samples in their dynamic range and $var[f]$ is the speckle-free image variance. In the absence of a “true” reflectivity model, the denoised image is used as the ground-truth and the original image is used for estimating the noise.

Mean Structural Similarity Index Measurement (MSSIM)

While the MSE describes the global performance of filters, the mean structural similarity index measurement (MSSIM) is used for assessing changes that occur at a higher structural level (Wang *et al.*, 2004). As such, it offers a better discrimination between images with similar MSE. The MSSIM index is defined in Equation 12. The index takes values in the [0;1] interval, with 0 indicating no structural similarity and 1, perfect similarity.

$$MSSIM = \frac{1}{M} \sum_p^{M-1} \left[\frac{2 \times E[f_p] \times E[\hat{f}_p] + C1}{E[f_p^2] + E[\hat{f}_p^2] + C1} \times \frac{2 \times Cov[f_p, \hat{f}_p] + C2}{var[f_p] + var[\hat{f}_p] + C2} \right], \quad (12)$$

where f_p , \hat{f}_p are the original and despeckled image patched areas determined by $p = (0; M-1)$ where $p \in \mathbb{Z}$, and M , which is the size of the kernel matrix. $C1$ and $C2$ are constants. As for PSNR, the despeckled image is considered to reflect the ground-truth and the noisy image is used to estimate noise estimate.

Equivalent Number of Looks (ENL)

Unlike PSNR and MSSIM, the equivalent number of looks (ENL) index is a “without-reference” method used in the evaluation of speckle filter performance in the homogeneous regions of the image. Therefore, only the despeckled image (\hat{f}) serves as an input. The ratio between the squared mean ($\mu_{\hat{f}}^2$) and the squared standard deviation ($\sigma_{\hat{f}}^2$) (Equation 13) reveals if the nominal number of looks has increased after filtering. An initial 4.4 ENL corresponds to Ground Range Detected High Resolution (GRD-HR) Copernicus Sentinel-1 products (Collecte Localisation Satellites, 2016). In the multilooking step during the pre-processing, the slant-to-ground range conversion of the SAR pixels has been done at a 1x1 ENL in range and azimuth for preserving spatial resolution. Larger ENL values represent better smoothing capabilities of the filter.

$$ENL = \frac{\mu_{\hat{f}}^2}{\sigma_{\hat{f}}^2} \quad (13)$$

Edge Correlation (EC) and the Edge Preservation Index (EPI)

Edge retaining capabilities are a key requirement for a speckle filtering technique, given that real SAR data exhibits a higher structural complexity of features than synthetically generated data or dummy imagery. In oceanic environments, these structures vary from slicks to footprints of the metocean phenomena. An essential condition is for the despeckle method to have the capacity to resolve sudden changes in the signal, retaining the edge boundary as unaltered as possible. Oil slicks usually induce a variability in contrast, which translates into an abrupt peaking of the signal. However, when local meteorological conditions are unfavorable, faint expressions of the slick do not produce an equally strong peak. The goal is for the despeckling method to provide sufficient smoothing of the surrounding homogeneous area while maintaining the less-developed structures. To evaluate the capability of each speckle filtering method in this regard, two key indexes were computed.

The edge correlation (EC) index (Equation 14) was proposed by Sattar *et al.* (1997) as a method for assessing echographic images and later adapted to SAR imagery by Achim *et al.* (2003). The method makes use of an additional high-pass filter to obtain an edge-map of the original image and the despeckled image. The correlation coefficient is calculated between the two images. Values of EC closer to unity indicate a better performance.

$$EC = \frac{Cov[f^H \hat{f}^H]}{\sqrt{Var[f^H] \times Var[\hat{f}^H]}}, \quad (14)$$

where f^H, \hat{f}^H are the high-pass filtered original and despeckled images. The original SAR image is used for estimating noise, while the despeckled image approximates the ground-truth. Mansourpour *et al.* (2006) and Gonzalez and Woods (2008) propose a custom high-pass Laplacian kernel, however, in this current study a Sobel operator (Sobel and Feldman, 1968) was used for heightened edge emphasis.

The edge correlation method is prone to distortion caused by any residual noise (Argenti *et al.*, 2013), therefore, a second quantitative method was utilized to confirm filter efficiency. The Edge Preservation Index (EPI), or the Edge Saving Index (ESI), originated as an evaluation method in medical image processing (Joseph *et al.*, 2017) and has been adopted as an evaluation index in other studies (Wu and Yuan, 2008; Zhang *et al.*, 2020). In similarity to the EC method, EPI uses a non-linear spatial filter for denoising the original and despeckled images and obtaining a binary edge-map (Equation 15). The two edge maps are then correlated. EPI range is [0,1], where 1 is defined as perfect correlation.

$$EPI = \frac{\sum_0^{M-1} |p_{s(i,j)} - p_{s(i+1,j)}| + |p_{s(i,j)} - p_{s(i,j+1)}|}{\sum_0^{M-1} |p_{o(i,j)} - p_{o(i+1,j)}| + |p_{o(i,j)} - p_{o(i,j+1)}|}, \quad (15)$$

where M is the size of the moving window matrix, $p_{(i,j)}, p_{(i+1,j)}$ are adjacent vertical pixels and $p_{(i,j)}, p_{(i,j+1)}$ are adjacent horizontal pixels of the despeckled (s) and original images (o).

RESULTS AND DISCUSSION

To assess the performance of the 14 selected speckle filters, the quality indices were computed and compared across the different filters and the two pre-processing approaches. In total, 40 denoised subsets were generated (20 DN and 20 NRCS) for both Kobuleti and Rize. Each initial ROI was compared against its corresponding despeckled ROI. These results are shown in Tables 3-11, with the best filtering method highlighted in red and the second and third in blue.

PSNR

The results evaluating the qualitative properties with PSNR (dB) are shown in Table 3 for DN images and in Table 4 for NRCS images. Larger PSNR values are associated with better despeckling capabilities, marking the prevalence of the signal in the waveform compared to the amount of noise. PSNR offers an absolute estimate and does not provide any information about structural preservation.

For the DN images, the best performance is achieved using the Enhanced Frost filter over 90% of the samples. The range of values obtained in all cases sets the PSNR for the Enhanced Frost filter between 45.91 dB and 50.14 dB where sudden changes in contrast and texture are found (all ROIs 1), 31.97–100 dB in all ROIs 2 where fine details introduce a slight change in contrast, and 37.01–59.74 dB in homogenous areas (all ROIs 3 and 4). The Refined Lee and SAR-BM3D methods also provide satisfactory results. For the SAR-BM3D, the range of values varies between 23.82–32.80 dB in ROIs1, 22.70–32.98 dB in ROIs2 and 23.35–38.64 dB in ROIs 3 and ROIs 4. The Refined Lee filter's performs consistently across all ROIs, varying between 24.26 dB and 28.45 dB. In this case, the filter performs slightly better in non-homogenous areas than in regions where ocean features are included in the ROI.

For the NRCS images, the best results are achieved for the Lee filter, the Refined Lee and the SNN filter in both study area ROIs. The Lee filter is effective for almost all of the analyzed ROIs, demonstrating its consistent behavior. For the heterogeneous regions at both locations and at all time points (ROIs 1), the Lee filter PSNR values span a range of 29.31–32.2 dB, while in the textured regions (ROIs 2) they show a slight decrease (26.75–29.67 dB). In homogenous areas, the filter displays similar values (26.47–33.11 dB) which only vary if the texture of the image is

more enhanced. Both Refined Lee and SNN filter exhibit PSNR values lower, but close, to the Lee filter (between 20–25 dB) and a similar variation over all the ROIs.

On the other side of the spectrum, the lowest performing filters can be categorized as follows:

- When applied to DN images, anisotropic diffusion-based filters (SRAD and i-DWT), the Enhanced Lee filter and the Frost filter do not show a strong denoising performance. It was suggested previously that the Frost filter in its original definition does not necessarily produce satisfactory results (Mascarenhas, 1997). It was however expected to exhibit better results for the Enhanced Lee filter as recommended by Suresh *et al.* (2015). In fact, they produce low PSNR values (in the range of 18–22 dB). Low values are also generated by the Lee Filter (20–23 dB) and the Gamma Map, Median and the Lee Sigma (20–22 dB). When compared to other filters from the Lee family, the reason for the Refined Lee filter achieving higher PSNR might be attributed to the larger moving window at which it operates.
- PSNR values for NRCS images are lowest for the SAR-BM3D, the Enhanced Frost filter and the Median filter. This suggests that the three algorithms do not produce a good enhancement in denoising, altering the overall image aspect.

MSSIM

MSSIM offers a complementary perspective to PSNR, as it helps to understand the extent to which the structure of the image was altered considerably by the filter. In Table 5, the similarity at structural level is quantified using the MSSIM. The index is assessed over the DN images only, as the low range of backscatter values does not produce significant variation for a consistent analysis for the NRCS images.

Similarly to the PSNR, the Enhanced Frost, Refined Lee and SAR-BM3D filters manage to best retain the structural composition of the image, offering the highest degree of similarity. The Enhanced Frost filter exhibits very high structural similarity and, in some cases, perfect alignment with the original image, with values ranging between 0.969 and 1. Such high similarity signifies excellent preservation of image structure. Indeed, the Frost filter, a precursor of the Enhanced Frost filter, despite performing poorly in this analysis, has been successfully used in the past for simultaneously despeckling scenes and preserving texture (European Space Agency, 2000). The enhanced version of the Frost filter was expected to generate better results by treating speckle variation more in-depth.

The SAR-BM3D algorithm results also indicate good structural similarity, with most values being between of 0.887–0.949 over heterogeneous areas for both Kobuleti and Rize (ROIs 1 and 2). Slightly higher correlation is observed in the homogeneous areas (0.928–0.985) which are the ROIs 3 and 4. One exception is given by the ROIs from the Rize image (20.07.2019), the SNN filter provides a better performance (0.731 ROI1, 0.727 ROI2, 0.723 ROI3, 0.744 ROI4 when compared to the 0.57 ROI1, 0.538 ROI2, 0.693 ROI3, 0.612 ROI4 values produced by SAR-BM3D). The explanation for the loss of performance in preserving the local structural elements can be explained by perhaps a stronger degradation of the samples due to the existence of either more similar pixel areas or fine detail when compared to the other ROI samples. The existence of pronounced demarcation is supported by the higher performance of the SNN on the image samples from the Rize image (20.07.2019) The Refined Lee filter is the third best

performing method following the SAR-BM3D and the Enhanced Frost filters. For the Refined Lee, the MSSIM was calculated as between 0.757 and 0.798 in heterogeneous areas (all ROIs 1 and ROIs 2). In homogeneous regions, the Refined Lee performed consistently, achieving values of 0.748–0.812 (all ROIs 3 and ROIs 4).

Low structural similarity is showcased by the i-DWT filter, which has an anomalous range of very low values (<0.06 in all samples). This behavior strongly suggests very low preservation of local structure and heavy alteration of the image. Median, Enhanced Lee, Lee Sigma and the Gamma Map filters also perform poorly (0.200–0.350 in all samples) when compared to other methods, highlighting that the algorithms only rely on the calculation of local statistics tend to overestimate the noise levels. Another possible explanation might be related to the small sliding window that was used for this assessment, which could reduce the overall effectiveness of a filter by reducing the area of estimation.

ENL

Table 6 and Table 7 show the results associated with the equivalent number of looks (ENL) in homogeneous areas at all locations (Rize and Kobuleti) and time points (ROIs 3 and 4) and the analysed values refer to all the samples. For DN subsets, the improved Discrete Wavelet Transformation (i-DWT) method produces very high values of ENL (in the range of 482.35–3576.02), which indicates an overestimation of the signal and a poor performance. Other high ENL producers are the Lee filter (86.27–133.14) and SRAD (154.3–281.89). A higher number of looks is displayed by the Guided filter only in the case of the samples from the Rize (20.07.2019) image. In general, such an elevated ENL is associated with alteration of the image.

Low DN ENL values are provided by the Enhanced Frost filter (9.07–18.08), the SAR-BM3D (18.30–56.64), Refined Lee (41.99–52.89) and the SNN (37.17–48.55). When analyzed together with the MSSIM and PSNR figures, the lower ENL can signify that the samples were not highly altered. Indeed, the ENL level is closer to original ROIs ENL values, with an average value of 17, which suggests that the overall denoising performance was not exaggerated.

For the NRCS pre-processing, the values indicate that the Guided filter is the best performing filter at smoothing homogeneous area (8.2–56.64), closely followed by the Frost methods (Enhanced Frost and Frost) whose values are between 12.46–18.15 ENL. Again, contrary to the presumption that a high ENL means better performance, the high values can suggest that these filters are overestimating the level of noise. An average level of 2.5 ENL has been computed for all ROIs. Moreover, algorithms that exhibit lower ENL figures (less than 10 ENL for the Lee, Refined Lee and SNN filters), were also found to produce better PSNR and MSSIM results.

EC and EPI

In order to evaluate the edge retention capabilities, the edge correlation (EC) and edge preservation index (EPI) were computed. Table 8 and Table 9 show the EC values for DN and NRCS, and Table 10 and Table 11 for EPI values, respectively.

In DN subsets, high edge retention is exhibited by the Enhanced Frost Filter, the Guided Filter, and the SAR-BM3D. The EC values for the Enhanced Frost filter are elevated (between 0.982–

1 in all ROIs), while for the Guided Filter the values are slightly lower at 0.939–0.985 for ROIs 1, 0.941–0.992 for ROIs 2, and 0.948–0.995 for homogenous ROIs 3 and 4. The SAR-BM3D algorithm produces similar values as the Guided Filter (0.796–0.971 for ROIs 1, 0.782–0.987 for ROIs 2, and 0.813–0.986 for ROIs 3 and ROIs 4). The lower range of values is associated with the Rize 20.07.2019 samples, indicating the same loss of structure as for the MSSIM. Although not highlighted as best performing, it is notable that the Refined Lee displays consistent high correlation values, which are slightly lower than previously mentioned algorithms (0.911–0.932 for all ROIs).

The lowest EC values for DN ROIs are given by the i-DWT filter (>0.300) and the Enhanced Lee filter (>0.400) further supporting the notion of increased image alteration. Deficient edge correlation is also seen for the Lee Sigma, SRAD, Frost, Gamma Map and Median filters as all the values fall within the 0.300–0.450 interval.

The EPI displays a similar behavior for the Enhanced Frost Filter (0.991–0.999 for ROIs 1, 0.99–1 for ROIs 2, and 0.994–0.999 for ROIs 3 and ROIs 4) and the Guided filter (0.97–0.99 for ROIs 1, 0.992–0.993 for ROIs 2, and 0.981–0.995 for ROIs 3 and ROIs 4). However, in this case, the Lee filter outperforms SAR-BM3D for most of the heterogeneous samples (e.g., 0.84–0.89 for the Lee filter in ROIs 1 compared to 0.54–0.85 for SAR-BM3D on the same samples), while performing similarly in some homogeneous regions (both filters display values in the range of 0.82–0.94). Once again, lower edge preservation is associated with the SAR-BM3D over the Rize imagery (20.07.2019) ROIs, confirming the presumption that edge structure was not preserved correctly. The Refined Lee filter and the SNN filter, which are performing well for other indices, have only modest capability in fully conserving fine detail and edges (0.600–0.750 across all samples).

Similar to what has been described for the EC index, accentuated loss of edge retention is indicated by the very low EPI values of the SRAD, Enhanced Lee, Gamma Map and Frost filters (<0.200 for all ROIs). Moreover, edge loss is also apparent with the i-DWT and Lee Sigma filters (<0.100 for all ROIs).

With regards to the NRCS images, the best edge correlation (EC) is achieved with the Lee filter (0.982–0.991 for ROIs 1, 0.982–0.993 for ROIs 2, and 0.978–0.986 for ROIs 3 and ROIs 4), followed by the Guided filter (0.593–0.988 across all ROIs) and the Refined Lee filter (0.900–0.930 across all ROIs). The same performance trend is observed in Edge preservation with the Lee filter achieving the highest EPI (0.985–0.9926 for ROIs 1, 0.984–0.993 for ROIs 2, and 0.981–0.987 for ROIs 3 and ROIs 4), followed by the Guided filter (0.921–0.987 for all regions) and the Refined Lee filter (0.713–0.736 for all ROIs). Notably, the worst performing methods are the Frost, Enhanced Frost and Lee Sigma filters, with EC values of 0.300–0.400 in all ROIs. This lack of high correlation for these filters is also supported by their very low EPI values (<0.200). Poor edge retention is also apparent for the Gamma Map, Median and Bilateral filters (<0.200 EPI).

Visual Analysis and Overall Performance

A visual analysis of the image was also conducted in order to verify the quantitative analysis. Examples of the filtered ROIs are provided for DN (Figures 6, 8, 10, 12) and NRCS images (Figures 7, 9, 11, 13). For DN images, in heterogeneous areas, the Enhanced Frost (Figure 6h,8h), Refined Lee (Figure 6f, 8f) and SAR-BM3D (Figure 6n,8n) filters exhibit satisfactory smoothing and edge retention when analyzed from both a quantitative and visual perspective.

The Enhanced Frost filter produces a smoothed image that succeeds at preserving the statistical information from the original input (as confirmed by the PSNR and MSSIM values) and uses a limited amount of looks (low ENL). The filter also displays maximum edge correlation and preservation, which is supported by the lack of a smudge effect at oil slick boundaries. SAR-BM3D despeckled images also display good textural preservation, where homogenous areas retain the statistical distribution of values, but the aspect is overall improved (i.e., high PSNR and MSSIM). A slight increase in the number of dark pixels can be observed when visually compared to the original image. This could be due to the manner in which block aggregation is formed during filtering. The high values of the EC and EPI indices are reinforced by the sharp aspect of the feature edges, as well as the preservation of fine details where the difference in contrast is not evident. The Refined Lee filter also displays a higher degree of smoothing, however, textural information is preserved and the blur effect is not intense. Based on an analysis of the PSNR and MSSIM indices for the Refined Lee filter, the extracted values indicate a satisfactory performance of the filter. The edge preservation parameters show that the Refined Lee filter is capable of resolving the sharp contrast change, which is evident through a visual analysis, although some loss of detail is observable where faint details were present in the original image. Similar to the results produced by the Refined Lee filter, the SNN filter (Figures 6i, 8i) exhibits textural preservation and low blur levels. Edge smudging is not visible in this case either, with visible slick boundaries and good separation between the slick feature and the surrounding sea at both the Rize and Kobuleti study areas. The Guided filter (Figure 6k, 8k) offers a high degree of blurring, although it still manages to retain edges.

The Enhanced Lee (Figure 6e, 8e), Lee Sigma (Figures 6d, 8d), Frost (Figures 6g, 8g), Gamma Map (Figures 6o, 8o) and SRAD (Figures 6l, 8l) filters all introduce visible blur to the image, as confirmed by their low MSSIM, EC and EPI values. A high level of image alteration is seen in the SRAD images, supported by the good overall performance with respect to PSNR, and low MSSIM, EC and EPI. A small number of artefacts are visible in the final Lee Sigma and Enhanced Lee images, perhaps induced by small point targets. The same two filters produce an increase in image contrast, therefore an overestimation of the dark pixels and different distribution of the image statistics. The i-DWT filter severely alters the structure of the image (Figure 6m, 8m), as corroborated quantitatively by the very low MSSIM, very high ENL and the loss of in EC and EPI.

In homogenous regions of the DN images, the same observations highlighted above also apply. The Enhanced Frost filter (Figure 10h, 12h) produces very good textural and structural preservation of the signal, as confirmed by the high PSNR and MSSIM, with a low ENL. However, some structural degradation is visible for the SAR-BM3D (Figure 10n, 12n) and the Refined Lee (Figure 10f, 12f). The SNN filter (Figure 10i, 12i) offers good textural preservation and enhancement of contrasting pixels. A finer estimation of the speckle levels in the homogenous areas within the sample is given by the Guided Filter (Figure 10k, 12k), confirming the good indices performance and higher ENL.

It is to be noted that, whilst the SAR-BM3D filter produces good results in terms of PSNR, MSSIM, EC and EPI, the algorithm was found to require significantly more computational resources during the processing than any of the other methods (e.g., the Guided Filter, Enhanced Frost, Lee filter, Refined Lee filter). This concurs with the observations of Argenti *et al.* (2013), and somewhat limits its use in an operational capacity.

The same blurring effect observed for heterogeneous regions is also observed for the homogeneous ROIs filtered with Enhanced Lee (Figure 10e, 12e), Lee Sigma (Figure 10d, 12d),

Frost (Figure 10g, 12g), Bilateral (Figure 10j, 12j) and Gamma Map (Figure 10o, 12o). Contrast levels are higher, and artefacts are present in the Lee Sigma and Enhanced Lee filter. The SRAD (Figure 10l, 12l) produces a highly blurred effect, which gives it a high ENL. Ultimately, a visual inspection of the i-DWT filtering results (Figure 10m, 12m) confirms its overall poor performance, by rendering a structurally altered image.

Local statistics-based filters such as Lee (Figure 7c, 9c), the Refined Lee (Figure 7f, 9f) and SNN (Figure 7i, 9i) approximate the level of multiplicative noise in NRCS images very well. Their overall visual appearance is supported by their high PSNR values. The Lee filter provides the best quantitative and qualitative results, through its smoothing of the homogenous areas, edge sharpening and its good preservation of the signal, which are further confirmed by the highest values for the PSNR, EC and EPI indices. The Refined Lee and the SNN filters also exhibit good textural retention, especially visible in the sea area, and good edge retention at the slick boundary.

Enhanced smoothness and contrast is observed in the Enhanced Lee (Figure 7e, 9e) and Lee Sigma (Figure 7d, 9d) filtered images, however, the blurring effect is pronounced (poor edge correlation and retention confirmed by EC and EPI values), and artefacts are present in the images. The Guided filter (Figure 7k, 9k) provides general blurred homogenization whilst managing edge retention, although it alters the signal significantly and loses fine detail. The SAR-BM3D filtering (Figure 7n, 9n) produces anomalous results for NRCS images, rendering a highly smoothed representation of the original image. This effect is most likely associated with the sub-unitary range of values of the NRCS. Unexpectedly, the good quantitative result produced with the i-DWT filter was not confirmed by the visual appearance of the images (Figure 7m, 9m). The homogenous areas are clustered, leading to contrasting pixel isolation. The low degree of edge retention is supported by the altered look of slick and other feature edges. This effect is more evident in the case of ROI2 (Figure 9m), where overestimation in homogenous areas is considerable. Furthermore, the SRAD filter (Figure 7l, 9l) also exhibits similar behavior as the i-DWT, which is not directly apparent through the quantitative analysis. The performance of the filters for the homogeneous NRCS ROIs (Figures 11, 13) is consistent with that for the heterogeneous areas.

When comparing the filters' performance on the Rize samples and the Kobuleti samples, no significant differences are encountered. Both sites display fairly consistent behavior that relates to the metocean conditions at the time of the acquisition: all samples were acquired during the summer months and episodes of calm sea state and no significant biological activity. However, these conditions are greatly dynamic and subsequent scenes might display a different statistical distribution of the pixels, indicating diverse marine and atmospheric processes (e.g., rain cells, upwelling events, algal blooms). Nevertheless, we anticipate that even though the statistical variation of the values would change, the computational efficiency of each filtering method should remain similar.

CONCLUSIONS

This study has presented an evaluation of the performance of a variety of different speckle filters applied to Sentinel-1 SAR images. The results demonstrate that the process of despeckling Sentinel-1 SAR imagery containing natural oil slicks is beneficial. This is because speckle-contaminated imagery can be effectively processed in order to reduce the strong backscatter variation in the image. As a result, this can decisively improve the visual quality of

the imagery, which has the potential to enhanced subsequent segmentation and dark formation extraction.

However, a number of aspects regarding despeckling have to be taken into consideration. The nature of the SAR data acquisition and image formation induces a specific pattern of signal and noise distribution within the data. Speckle cannot be treated as ordinary noise since much of the useful radiometric information is embedded within it. Preserving this information as much as possible is one of the main objectives of despeckling. To achieve this, the desired method needs to perform with minimum invasiveness.

It is clear that prior to despeckling, pre-processing through multilooking can offer a good quality input image in preparation for denoising. However, as multilooking comes at the expense of spatial resolution, the procedure needs to be kept to a minimum and a second type of despeckling step should be considered. An important argument is that speckle filtering is further degrading the spatial resolution of the imagery through changing image statistics. Therefore, a careful selection of filter parameter settings must be made prior to the operation. A moving window of 5x5 or 7x7 was considered to be sufficient for this evaluation as they ensure the filter is computationally efficient and introduces enough smoothing while being able to estimate edge statistics without much altering them significantly.

From both the quantitative and qualitative assessments it is clear that denoising radiometrically distinct images requires separate workflows depending on the nature of the pre-processing. Traditional filters (Enhanced Frost, Refined Lee, Lee filter) were found to perform well on both types of pre-processed images (DN and NRCS). Adaptive filtering using local statistics is simple, effective and computationally efficient, unlike wavelet-based methods. If used in an operational context, filters like Lee or the Refined Lee are adequate for efficient denoising and in retaining the signal structural information that is critical for the next processing steps in an oil slick detection workflow. These filters also perform well at feature boundary level, hence in scenarios covering edge separation and segmentation, they will offer a satisfactory result.

If image speckle is treated in acquired amplitude/power (DN) datasets, an Enhanced Frost filter or a filter from the Lee class (Lee or Refined Lee) is recommended for despeckling. Larger window sizes (7x7) and a higher number of looks increase the performance of the algorithm but contribute to a reduced spatial resolution of the resulting image. If analyzing a small number of images, then the SAR-BM3D model is recommended for improved contrast and fine detail preservation. For cases where the images have been radiometrically calibrated (i.e., NRCS), the Lee class filters provide the best solution. Moreover, in any despeckling scenario, the use of several denoising steps may yield better efficiency. For example, this could include applying the same filter or a combination of filters for more than one iteration and with different window sizes (e.g., Lee 5x5 + Lee 3x3 or Lee 5x5 + Guided Filter 3x3).

Overall, this study confirms the general consensus that filters based on linear statistics provide fast, effective, and resource-friendly solutions for despeckling Copernicus Sentinel-1 SAR images containing oil slicks and metocean phenomena. Further work is needed to determine an optimum combination of filters that could be used successfully on a large dataset, based on the required computational resources and image denoising performance. Additionally, with future advances in computing efficiency, the potential use of convolutional neural networks in an operational capacity should also be explored. The findings of this study are likely to be applicable to other C-band sensors, such as ERS-1, ENVISAT, RADARSAT or new generation

sensors, although the performance of speckle filters on data for oil slicks captured using other radar wavebands requires further attention. Finally, while the present study focusses on seeps in the Black Sea, the method used in the evaluation and the findings are applicable to similar marine environments, provided that the metocean dynamic conditions and surfactant presence combine to produce a similar level of signal variability within the scene.

CONFLICT OF INTEREST: The authors declare no known conflicts of interest associated with this publication.

ACKNOWLEDGEMENTS

The work was primarily supported through a Vice-Chancellor Scholarship for Research Excellence awarded by the University of Nottingham to C.A.V. The authors would like to thank Mr. Américo Ambrózio (Deimos Engenharia c/o European Space Agency) for his invaluable help and suggestions during code development and Dr. Gordon Campbell and Dr. Zoltan Bartalis (European Space Agency) for their continuous support during C.A.V's placement at the Agency.

REFERENCES

- Achim, A., Tsakalides, P. and Bezerianos, A. 2003. SAR image denoising via Bayesian wavelet shrinkage based on heavy-tailed modeling. *IEEE Transactions on Geoscience and Remote Sensing*, **41**, 1773–1784, <https://doi.org/10.1109/TGRS.2003.813488>.
- Alpers, W. and Espedal, H. 2004. Oils and Surfactants. *In: Jackson, C. R. and Apel, J. R. (eds) Synthetic Aperture Radar Marine User's Manual*. **25**, 263.
- Apel, J.R. 2004. Oceanic Internal Waves and Solitons. *In: Jackson, C. R. and Apel, J. R. (eds) Synthetic Aperture Radar Marine User's Manual*. **25**, 189–207.
- Argenti, F., Lapini, A., Bianchi, T. and Alparone, L. 2013. A Tutorial on Speckle Reduction in Synthetic Aperture Radar Images. *IEEE Geoscience and Remote Sensing Magazine*, **1**, 6–35, <https://doi.org/10.1109/MGRS.2013.2277512>.
- Bharaneswari, M., Arulmozhivarman, P., Tatavarti, R. and Senthilnathan, K. 2015. Speckle noise suppression in SAR images (Oil spill images) using wavelet based methods and ICA technique. *In: 2015 IEEE International Conference on Signal Processing, Informatics, Communication and Energy Systems (SPICES) – 2015 IEEE International Conference on Signal Processing, Informatics, Communication and Energy Systems (SPICES)*. 1–5., <https://doi.org/10.1109/SPICES.2015.7091521>.
- Bianco, E., Boughter, B., Hall, M., Amato del Monte, A., Hamlyn, W. and Ross-Ross, S. 2020. Bruges.

- Bradski, G. 2000. Open Source Computer Vision Library.
- Brekke, C. and Solberg, A.H.S. 2005. Oil spill detection by satellite remote sensing. *Remote Sensing of Environment*, **95**, 1–13, <https://doi.org/10.1016/j.rse.2004.11.015>.
- Choi, H. and Jeong, J. 2019. Speckle Noise Reduction Technique for SAR Images Using Statistical Characteristics of Speckle Noise and Discrete Wavelet Transform. *Remote Sensing*, **11**, 1184, <https://doi.org/10.3390/rs11101184>.
- Collecte Localisation Satellites. 2016. Sentinel-1 Product Definition.
- de Souza, D.L., Neto, A.D.D. and da Mata, W. 2006. Intelligent System for Feature Extraction of Oil Slick in SAR Images: Speckle Filter Analysis. In: King, I., Wang, J., Chan, L.-W. and Wang, D. (eds) *Neural Information Processing*. Lecture Notes in Computer Science, 729–736., https://doi.org/10.1007/11893257_81.
- European Space Agency. 2000. ERS Radar Courses: Radar Course III - Image interpretation: Speckle. *ESA Earth Online* https://earth.esa.int/web/guest/missions/esa-operational-eo-missions/ers/instruments/sar/applications/radar-courses/content-3/-/asset_publisher/mQ9R7ZVkkG5P/content/radar-course-3-image-interpretation-tone.
- Farrington, J. 1985. Oil pollution: a decade of research and monitoring. *Oceanus*, **28**, 2–12.
- Franceschetti, G. and Lanari, R. 2018. *Synthetic Aperture Radar Processing*, 1st ed., <https://doi.org/10.1201/9780203737484>.
- Frost, V.S., Stiles, J.A., Shanmugan, K.S. and Holtzman, J.C. 1982. A Model for Radar Images and Its Application to Adaptive Digital Filtering of Multiplicative Noise. *IEEE Transactions on Pattern Analysis and Machine Intelligence*, **PAMI-4**, 157–166, <https://doi.org/10.1109/TPAMI.1982.4767223>.
- Gagnon, L. and Jouan, A. 1997. Speckle filtering of SAR images: a comparative study between complex-wavelet-based and standard filters. In: Aldroubi, A., Laine, A. F. and Unser, M. A. (eds) *Optical Science, Engineering and Instrumentation '97*. 80–91., <https://doi.org/10.1117/12.279681>.
- Gambardella, A. 2007. *Oil Spill Detection by Means of Synthetic Aperture Radar*. Tesi di Dottorato, Università degli Studi di Cagliari.
- Gasull, A., Fabregas, X., Jiménez, J., Marqués, F., Moreno, V. and Herrero, M. 2002. Oil spills detection in SAR images using mathematical morphology. *Proceedings of EUSIPCO*, **1**.
- Girard-Ardhuin, Mercier, and Garello. 2003. Oil slick detection by SAR imagery: potential and limitation. In: *Oceans 2003. Celebrating the Past ... Teaming Toward the Future (IEEE Cat. No.03CH37492)* – Oceans 2003. Celebrating the Past ... Teaming Toward the Future. 164-169 Vol.1., <https://doi.org/10.1109/OCEANS.2003.178539>.
- Gonzalez, R.C. and Woods, R.E. 2008. *Digital Image Processing*, 3rd ed.

- Goodman, J.W. 1976. Some fundamental properties of speckle*. *Journal of the Optical Society of America*, **66**, 1145, <https://doi.org/10.1364/JOSA.66.001145>.
- Hall, M. 2007. Smooth operator: Smoothing seismic interpretations and attributes. *The Leading Edge*, **26**, 16–20, <https://doi.org/10.1190/1.2431821>.
- He, K., Sun, J. and Tang, X. 2013. Guided Image Filtering. *IEEE Transactions on Pattern Analysis and Machine Intelligence*, **35**, 1397–1409, <https://doi.org/10.1109/TPAMI.2012.213>.
- Hervet, E., Fjortoft, R., Marthon, P. and Lopes, A. 1998. Comparison of wavelet-based and statistical speckle filters. In: Posa, F. (ed.) *Remote Sensing*. 43–54., <https://doi.org/10.1117/12.331361>.
- Holt, B. 2004. SAR imaging of the ocean surface. In: Jackson, C. R. and Apel, J. R. (eds) *Synthetic Aperture Radar Marine User's Manual*. **25**, 25–80.
- Hühnerfuss, H., Alpers, W., et al. 1983. The modification of X and L band radar signals by monomolecular sea slicks. *Journal of Geophysical Research: Oceans*, **88**, 9817–9822, <https://doi.org/10.1029/JC088iC14p09817>.
- Jong-Sen Lee, Grunes, M.R. and de Grandi, G. 1999. Polarimetric SAR speckle filtering and its implication for classification. *IEEE Transactions on Geoscience and Remote Sensing*, **37**, 2363–2373, <https://doi.org/10.1109/36.789635>.
- Jong-Sen Lee, Jong-Sen Lee, Jen-Hung Wen, Ainsworth, T.L., Kun-Shan Chen and Chen, A.J. 2009. Improved Sigma Filter for Speckle Filtering of SAR Imagery. *IEEE Transactions on Geoscience and Remote Sensing*, **47**, 202–213, <https://doi.org/10.1109/TGRS.2008.2002881>.
- Joseph, J., Jayaraman, S., Periyasamy, R. and Renuka, S. 2017. An Edge Preservation Index for Evaluating Nonlinear Spatial Restoration in MR Images. *Current Medical Imaging Reviews*, **13**, 58–65, <https://doi.org/10.2174/1573405612666160609131149>.
- Karathanassi, V., Topouzelis, K., Pavlakis, P. and Rokos, D. 2006. An object-oriented methodology to detect oil spills. *International Journal of Remote Sensing*, **27**, 5235–5251, <https://doi.org/10.1080/01431160600693575>.
- Keramitsoglou, I., Cartalis, C. and Kassomenos, P. 2003. Decision Support System for Managing Oil Spill Events. *Environmental Management*, **32**, 290–298, <https://doi.org/10.1007/s00267-003-2969-7>.
- Körber, J.-H., Sahling, H., Pape, T., dos Santos Ferreira, C., MacDonald, I. and Bohrmann, G. 2014. Natural oil seepage at Kobuleti Ridge, eastern Black Sea. *Marine and Petroleum Geology*, **50**, 68–82, <https://doi.org/10.1016/j.marpetgeo.2013.11.007>.
- Kupidura, P. 2016. COMPARISON OF FILTERS DEDICATED TO SPECKLE SUPPRESSION IN SAR IMAGES. *ISPRS - International Archives of the Photogrammetry, Remote Sensing and Spatial Information Sciences*, **XLI-B7**, 269–276, <https://doi.org/10.5194/isprsarchives-XLI-B7-269-2016>.
- Kvenvolden, K.A. and Cooper, C.K. 2003. Natural seepage of crude oil into the marine environment. *Geo-Marine Letters*, **23**, 140–146, <https://doi.org/10.1007/s00367-003-0135-0>.

- Lattari, F., Gonzalez Leon, B., Asaro, F., Rucci, A., Prati, C. and Matteucci, M. 2019. Deep Learning for SAR Image Despeckling. *Remote Sensing*, **11**, 1532, <https://doi.org/10.3390/rs11131532>.
- Leberl, F.W. 1990. *Radargrammetric Image Processing*. Artech House remote sensing library.
- Lee, G., Gommers, R., Waselewski, F., Wohlfahrt, K. and O'Leary, A. 2019. PyWavelets: A Python package for wavelet analysis. *Journal of Open Source Software*, **4**, 1237, <https://doi.org/10.21105/joss.01237>.
- Lee, J.-S. 1980. Digital Image Enhancement and Noise Filtering by Use of Local Statistics. *IEEE Transactions on Pattern Analysis and Machine Intelligence*, **PAMI-2**, 165–168, <https://doi.org/10.1109/TPAMI.1980.4766994>.
- Lee, J.-S. 1981. Speckle analysis and smoothing of synthetic aperture radar images. *Computer Graphics and Image Processing*, **17**, 24–32, [https://doi.org/10.1016/S0146-664X\(81\)80005-6](https://doi.org/10.1016/S0146-664X(81)80005-6).
- Lee, J.-S. 1983. Digital image smoothing and the sigma filter. *Computer Vision, Graphics, and Image Processing*, **24**, 255–269, [https://doi.org/10.1016/0734-189X\(83\)90047-6](https://doi.org/10.1016/0734-189X(83)90047-6).
- Lee, J.-S. and Pottier, E. 2009. *Polarimetric Radar Imaging: From Basics to Applications*. Optical science and engineering **142**.
- Lee, J.S., Jurkevich, L., Dewaele, P., Wambacq, P. and Oosterlinck, A. 1994. Speckle filtering of synthetic aperture radar images: A review. *Remote Sensing Reviews*, **8**, 313–340, <https://doi.org/10.1080/02757259409532206>.
- Leguizamón, S. 1997. Speckle Reduction in SAR Images by Using Discrete Wavelet Transform. In: *Image Processing Techniques, First Latino-American Seminar on Radar Remote Sensing: Proceedings*. 205.
- Li, C., Wang, Y. and Zhong, L. 2018. Review and research of speckle reducing filters for SAR image. In: Jiang, X. and Hwang, J.-N. (eds) *Tenth International Conference on Digital Image Processing (ICDIP 2018)* – Tenth International Conference on Digital Image Processing (ICDIP 2018). 338., <https://doi.org/10.1117/12.2503799>.
- Lopes, A., Touzi, R. and Nezry, E. 1990. Adaptive speckle filters and scene heterogeneity. *IEEE Transactions on Geoscience and Remote Sensing*, **28**, 992–1000, <https://doi.org/10.1109/36.62623>.
- Lopes, A., Nezry, E., Touzi, R. and Laur, H. 1993. Structure detection and statistical adaptive speckle filtering in SAR images. *International Journal of Remote Sensing*, **14**, 1735–1758, <https://doi.org/10.1080/01431169308953999>.
- Lyzenga, D.R., Marmorino, G.O. and Johannessen, J.A. 2004. Ocean Current and Currents Gradients. In: Jackson, C. R. and Apel, J. R. (eds) *Synthetic Aperture Radar Marine User's Manual*. **25**, 207–221.
- Makinen, Y., Azzari, L. and Foi, A. 2019. Exact Transform-Domain Noise Variance for Collaborative Filtering of Stationary Correlated Noise. In: *2019 IEEE International Conference on Image*

- Processing (ICIP)* – 2019 IEEE International Conference on Image Processing (ICIP). 185–189., <https://doi.org/10.1109/ICIP.2019.8802964>.
- Mallat, S.G. 2009. *A Wavelet Tour of Signal Processing: The Sparse Way*, 3rd ed.
- Mansourpour, M., Rajabi, M.A. and Blais, J.A.R. 2006. Effects and performance of speckle noise reduction filters on active radar and SAR images. *In: International Archives of ISPRS XXXVI 1/W41*.
- Mascarenhas, N.D.A. 1997. An Overview of Speckle Noise Filtering in SAR Images. *In: Quegan, S. and Moreira, J. R. (eds) Image Processing Techniques, First Latino-American Seminar on Radar Remote Sensing: Proceedings of a Conference Held 2-4 December, 1996 – First Latino-American Seminar on Radar Remote Sensing: Proceedings*.
- Mera, D., Cotos, J.M., Varela-Pet, J. and Garcia-Pineda, O. 2012. Adaptive thresholding algorithm based on SAR images and wind data to segment oil spills along the northwest coast of the Iberian Peninsula. *Marine Pollution Bulletin*, **64**, 2090–2096, <https://doi.org/10.1016/j.marpolbul.2012.07.018>.
- Migliaccio, M., Tranfaglia, M. and Ermakov, S.A. 2005. A Physical Approach for the Observation of Oil Spills in SAR Images. *IEEE Journal of Oceanic Engineering*, **30**, 496–507, <https://doi.org/10.1109/JOE.2005.857518>.
- Migliaccio, M., Nunziata, F. and Buono, A. 2015. SAR polarimetry for sea oil slick observation. *International Journal of Remote Sensing*, **36**, 3243–3273, <https://doi.org/10.1080/01431161.2015.1057301>.
- Migliaccio, M., Huang, L. and Buono, A. 2019. SAR Speckle Dependence on Ocean Surface Wind Field. *IEEE Transactions on Geoscience and Remote Sensing*, **57**, 5447–5455, <https://doi.org/10.1109/TGRS.2019.2899491>.
- National Research Council (US) Committee. 2003. Natural Seepage of Crude Oil into the Marine Environment. *In: Oil in the Sea III: Inputs, Fates, and Effects*.
- Nezry, E. 2014. Adaptive Speckle Filtering in Radar Imagery. *In: Closson, D., Holecz, F., Pasquali, P. and Milisavljević, N. (eds) Land Applications of Radar Remote Sensing*, <https://doi.org/10.5772/58593>.
- Oliver, C. and Quegan, S. 2004. *Understanding Synthetic Aperture Radar Images*. The SciTech radar and defense series.
- Paris, S., Kornprobst, P., Tumblin, J. and Durand, F. 2007. A gentle introduction to bilateral filtering and its applications. *In: ACM SIGGRAPH 2007 Courses on - SIGGRAPH '07 – ACM SIGGRAPH 2007 courses*. 1., <https://doi.org/10.1145/1281500.1281602>.
- Parrilli, S., Poderico, M., Angelino, C.V. and Verdoliva, L. 2012. A Nonlocal SAR Image Denoising Algorithm Based on LMMSE Wavelet Shrinkage. *IEEE Transactions on Geoscience and Remote Sensing*, **50**, 606–616, <https://doi.org/10.1109/TGRS.2011.2161586>.

- Pichel, W.G., Clemente-Colon, P., Wackerman, C.C. and Friedman, K.S. 2004. Ship and Wake Detection. *In: Jackson, C. R. and Apel, J. R. (eds) Synthetic Aperture Radar Marine User's Manual*. **25**, 277–305.
- Pichierri, M. and Rabus, B. 2018. Applications of SAR Remote Sensing in the Arctic: A Review. *In: 2018 18th International Symposium on Antenna Technology and Applied Electromagnetics (ANTEM) – 2018 18th International Symposium on Antenna Technology and Applied Electromagnetics (ANTEM)*. 1–4., <https://doi.org/10.1109/ANTEM.2018.8573026>.
- Redding, N.J. 1999. *Estimating the Parameters of the K Distribution in the Intensity Domain*. Technical Report **DSTO-TR-0839**.
- Rosa-Zurera, M., Cóbreces-Álvarez, A.M., Nieto-Borge, J.C., Jarabo-Amores, M.P. and Mata-Moya, D. 2007. Wavelet denoising with edge detection for speckle reduction in SAR images. *In: EUSIPCO, Domański, M., Stasiński, R., Bartkowiak, M. and European Association for Speech, Signal and Image Processing (eds) Wavelet Denoising with Edge Detection for Speckle Reduction in SAR Images – EUSIPCO*.
- Sattar, F., Floreby, L., Salomonsson, G. and Lovstrom, B. 1997. Image enhancement based on a nonlinear multiscale method. *IEEE Transactions on Image Processing*, **6**, 888–895, <https://doi.org/10.1109/83.585239>.
- SciPy 1.0 Contributors, Virtanen, P., et al. 2020. SciPy 1.0: fundamental algorithms for scientific computing in Python. *Nature Methods*, **17**, 261–272, <https://doi.org/10.1038/s41592-019-0686-2>.
- SNAP - ESA Sentinel Application Platform v7.0.4. n.d.
- Sobel, I. and Feldman, G. 1968. A 3x3 Isotropic Gradient Operator for Image Processing. *In: Stanford Artificial Intelligence Project (SAIL)*.
- Solberg, A.H.S. and Brekke, C. 2008. Oil Spill Detection in Northern European Waters: Approaches and Algorithms. *In: Barale, V. and Gade, M. (eds) Remote Sensing of the European Seas*. 359–370., https://doi.org/10.1007/978-1-4020-6772-3_27.
- Solberg, A.H.S., Storvik, G., Solberg, R. and Volden, E. 1999. Automatic detection of oil spills in ERS SAR images. *IEEE Transactions on Geoscience and Remote Sensing*, **37**, 1916–1924, <https://doi.org/10.1109/36.774704>.
- Suresh, G., Melsheimer, C., Korber, J.-H. and Bohrmann, G. 2015. Automatic Estimation of Oil Seep Locations in Synthetic Aperture Radar Images. *IEEE Transactions on Geoscience and Remote Sensing*, **53**, 4218–4230, <https://doi.org/10.1109/TGRS.2015.2393375>.
- Tomasi, C. and Manduchi, R. 1998. Bilateral filtering for gray and color images. *In: Sixth International Conference on Computer Vision (IEEE Cat. No.98CH36271) – IEEE 6th International Conference on Computer Vision*. 839–846., <https://doi.org/10.1109/ICCV.1998.710815>.
- Touzi, R. 2002. A review of speckle filtering in the context of estimation theory. *IEEE Transactions on Geoscience and Remote Sensing*, **40**, 2392–2404, <https://doi.org/10.1109/TGRS.2002.803727>.

- Touzi, R. and Lopes, A. 1994. The principle of speckle filtering in polarimetric SAR imagery. *IEEE Transactions on Geoscience and Remote Sensing*, **32**, 1110–1114, <https://doi.org/10.1109/36.312901>.
- Valenzuela, G.R. 1978. Theories for the interaction of electromagnetic and oceanic waves ? A review. *Boundary-Layer Meteorology*, **13**, 61–85, <https://doi.org/10.1007/BF00913863>.
- Walessa, M. and Datcu, M. 2000. Model-based despeckling and information extraction from SAR images. *IEEE Transactions on Geoscience and Remote Sensing*, **38**, 2258–2269, <https://doi.org/10.1109/36.868883>.
- Wang, P., Zhang, H. and Patel, V.M. 2017. SAR Image Despeckling Using a Convolutional Neural Network. *IEEE Signal Processing Letters*, **24**, 1763–1767, <https://doi.org/10.1109/LSP.2017.2758203>.
- Wang, Z., Bovik, A.C., Sheikh, H.R. and Simoncelli, E.P. 2004. Image Quality Assessment: From Error Visibility to Structural Similarity. *IEEE Transactions on Image Processing*, **13**, 600–612, <https://doi.org/10.1109/TIP.2003.819861>.
- Wilson, R.D., Monaghan, P.H., Osanik, A., Price, L.C. and Rogers, M.A. 1974. Natural Marine Oil Seepage. *Science*, **184**, 857–865, <https://doi.org/10.1126/science.184.4139.857>.
- Woodhouse, I.H. 2017. *Introduction to Microwave Remote Sensing*, 1st ed., <https://doi.org/10.1201/9781315272573>.
- Wu, Y. and Yuan, X. 2008. Wavelet speckle reduction for SAR imagery based on edge detection.
- Yu, Y. and Acton, S.T. 2002. Speckle reducing anisotropic diffusion. *IEEE Transactions on Image Processing*, **11**, 1260–1270, <https://doi.org/10.1109/TIP.2002.804276>.
- Zhang, G., Li, Z., Li, X. and Xu, Y. 2020. Learning synthetic aperture radar image despeckling without clean data. *Journal of Applied Remote Sensing*, **14**, 1, <https://doi.org/10.1117/1.JRS.14.026518>.
- Zhenghao Shi and Fung, K.B. 1994. A comparison of digital speckle filters. In: *Proceedings of IGARSS '94 - 1994 IEEE International Geoscience and Remote Sensing Symposium – IGARSS '94 - 1994 IEEE International Geoscience and Remote Sensing Symposium*. 2129–2133., <https://doi.org/10.1109/IGARSS.1994.399671>.

Table 1. Sentinel-1 SAR data product details

Name	SAR Dataset	Acquisition Date	Orbit
Kobuleti_25_07_2018	S1A_IW_GRDH_1SDV_20180725T032439_20180725T032504_022945_027D64_42BA.SAFE	25.07.2018	DESCENDING
Rize_25_07_2018	S1A_IW_GRDH_1SDV_20180725T032504_20180725T032529_022945_027D64_B9F7.SAFE	25.07.2018	DESCENDING
Rize_31_08_2018	S1A_IW_GRDH_1SDV_20180831T151017_20180831T151042_023492_028EBF_1D2A.SAFE	31.08.2018	ASCENDING
Kobuleti_20_07_2019	S1A_IW_GRDH_1SDV_20190720T032445_20190720T032510_028195_032F5B_1B62.SAFE	20.07.2019	DESCENDING
Rize_20_07_2019	S1B_IW_GRDH_1SDV_20190720T151738_20190720T151803_017219_020623_C67C.SAFE	20.07.2019	ASCENDING

Table 2. Speckle filtering input parameters

Speckle filtering method	Kernel size	Computation parameters
Guided Filter	Estimated	$r = 4, \epsilon = 2e-10^3$
SAR-BM3D	Estimated	$\sigma = 10$ for DN images $\sigma = 0.1$ for NRCS images
Enhanced Lee Filter	5x5	NLOOKS= 4.4, damping factor = 1 DWT: HAAR
Improved DWT	Estimated	SRAD: $k= 30, m= 0.5, q_0 = 1, \rho=1, \epsilon=0.05,$ number of iterations=150 Guided Filter $r = 4, \epsilon = 2e-10^3$ Soft threshold: 0.02 for Level 1, 0.06 at Level 2
Refined Lee	7x7 (default)	N/A
Lee Sigma	Kernel = 5x5, Target window= 5x5	$\sigma = 0.9, NLOOKS=1,$
Frost	5x5	Damping factor =1
Gamma Map	5x5	N/A
Median	5x5	N/A
Enhanced Frost	5x5	NLOOKS= 4.4, damping factor = 1
Lee	5x5	NLOOKS= 4.4, damping factor = 1
Bilateral	5x5	$\sigma = 80$
SNN	5x5	N/A (geometric method)
SRAD	Estimated	$k= 30, m= 0.5, q_0 = 1, \rho=1, \epsilon=0.05,$ number of iterations=150

Table 3. PSNR values for DN images

SAR data name DN	ROI	Guided Filter	SAR-BM3D	Enhanced Lee	i-DWT	Refined Lee	Lee Sigma	Frost	Gamma Map	Median	Enhanced Frost	Lee	Bilateral	SNN	SRAD
Kobuleti 25.07.2018	ROI1	25.28	30.71	21.80	20.48	26.14	21.89	21.89	21.80	21.76	47.46	22.94	24.01	25.51	21.22
	ROI2	25.15	30.99	21.61	20.22	25.89	21.68	21.70	21.62	21.59	48.68	22.72	23.83	25.36	21.00
	ROI3	25.73	32.31	21.88	20.42	26.35	21.95	21.97	21.88	21.86	47.65	22.89	24.28	25.62	21.22
	ROI4	30.49	38.64	23.91	22.43	28.45	24.00	24.00	23.91	23.88	59.74	25.00	26.83	27.64	23.24
Kobuleti 20.07.2019	ROI1	26.23	30.96	23.21	21.90	27.52	23.32	23.30	23.21	23.17	45.91	24.38	25.34	26.91	22.66
	ROI2	25.95	32.98	21.16	19.70	25.54	21.24	21.25	21.16	21.14	50.40	22.22	23.65	24.90	20.52
	ROI3	24.33	29.72	21.18	19.87	25.40	21.24	21.26	21.18	21.15	45.74	22.29	23.30	24.89	20.60
	ROI4	25.98	32.69	21.46	20.07	25.83	21.55	21.55	21.47	21.45	53.60	22.52	23.87	25.21	20.84
Rize 20.07.2019	ROI1	22.16	23.82	21.57	20.46	25.67	21.63	21.65	21.57	21.51	33.97	22.83	23.21	25.16	7.54
	ROI2	21.21	22.70	20.71	19.61	24.77	20.75	20.80	20.72	20.66	31.97	21.99	22.33	24.31	20.30
	ROI3	21.51	23.82	20.33	19.30	24.26	20.37	20.42	20.34	20.27	37.01	21.65	22.00	23.96	19.94
	ROI4	21.31	23.35	20.89	19.60	25.02	20.95	20.98	20.89	20.84	31.76	22.07	22.67	24.53	20.35
Rize 25.07.2018	ROI1	26.70	32.08	22.78	21.48	27.03	22.86	22.86	22.78	22.75	50.14	23.90	24.92	26.51	22.22
	ROI2	24.72	30.73	20.64	19.34	24.61	20.69	20.73	20.65	20.61	100.00	21.72	22.80	24.34	20.09
	ROI3	23.86	29.26	20.43	19.19	24.58	20.49	20.51	20.43	20.40	49.70	21.52	22.51	24.14	19.90
	ROI4	24.63	31.22	20.72	19.19	25.07	20.80	20.81	20.72	20.72	45.45	21.68	23.09	24.51	20.00
Rize 31.08.2018	ROI1	25.20	30.24	22.14	20.83	26.45	22.21	22.22	22.14	22.10	47.32	23.26	24.23	25.85	21.56
	ROI2	23.55	28.43	20.69	19.38	24.80	20.74	20.77	20.69	20.64	44.44	21.81	22.68	24.38	20.13
	ROI3	25.01	31.32	21.55	20.01	25.87	21.65	21.64	21.55	21.51	48.81	22.56	23.91	25.32	20.85
	ROI4	25.33	32.14	20.79	19.40	25.04	20.86	20.88	20.79	20.76	49.20	21.84	23.18	24.53	20.16

Table 4. PSNR values for NRCS images

SAR data name NRCS	ROI	Guided Filter	SAR- BM3D	Enhanced Lee	i-DWT	Refined Lee	Lee Sigma	Frost	Gamma Map	Median	Enhanced Frost	Lee	Bilateral	SNN	SRAD
Kobuleti 25.07.2018	ROI1	24.27	21.29	23.81	24.27	26.54	22.87	23.22	22.90	22.51	22.68	29.31	24.46	26.17	25.23
	ROI2	23.98	20.97	23.38	23.71	26.24	22.54	22.91	22.87	22.24	22.40	28.77	24.18	25.91	24.66
	ROI3	26.53	22.73	24.85	24.89	28.23	24.26	24.59	25.58	23.97	24.12	29.96	26.04	27.66	25.82
	ROI4	33.17	25.85	27.98	27.99	31.34	27.37	27.66	27.69	26.98	27.16	33.11	29.19	30.63	28.96
Kobuleti 20.07.2019	ROI1	26.54	23.80	26.57	27.12	29.14	25.58	25.90	25.41	25.17	25.34	32.12	27.11	28.82	28.08
	ROI2	24.53	20.10	22.33	22.58	25.40	21.61	21.95	21.89	21.30	21.44	27.64	23.34	24.96	23.50
	ROI3	22.66	20.04	22.94	23.66	25.12	21.63	22.09	22.02	21.34	21.49	28.68	23.22	25.01	24.74
	ROI4	24.77	20.74	22.98	23.25	25.96	22.21	22.57	22.59	21.92	22.06	28.33	23.90	25.58	24.23
Rize 20.07.2019	ROI1	21.95	18.50	25.00	26.18	25.88	22.64	23.22	22.80	22.27	22.49	31.11	23.99	25.87	27.61
	ROI2	20.28	16.60	23.50	24.72	24.19	20.96	21.61	21.25	20.63	20.86	29.67	22.33	24.24	26.26
	ROI3	19.87	17.18	23.02	24.25	19.92	20.22	20.89	20.53	19.85	20.10	29.22	21.53	23.49	25.87
	ROI4	20.31	16.62	22.34	22.97	24.68	21.20	21.62	21.54	20.87	21.05	28.05	22.73	24.51	24.04
Rize 25.07.2018	ROI1	27.00	23.18	25.53	25.99	28.23	24.64	24.98	24.55	24.32	24.46	31.02	26.12	27.98	26.94
	ROI2	22.79	19.06	21.27	21.73	23.80	20.41	20.83	20.75	20.19	20.33	26.75	21.98	23.83	22.69
	ROI3	21.40	18.61	20.95	21.44	23.54	20.04	20.43	20.51	19.77	19.90	26.47	21.59	23.44	22.41
	ROI4	22.91	19.03	21.05	20.91	24.43	20.62	20.91	21.02	20.36	20.48	25.99	22.35	24.10	21.82
Rize 31.08.2018	ROI1	24.46	21.89	24.40	24.85	27.18	23.49	23.86	23.63	23.18	23.35	29.90	25.07	26.85	25.82
	ROI2	21.25	18.93	21.67	22.26	24.04	20.58	21.01	20.96	20.29	20.46	27.31	22.11	23.96	23.29
	ROI3	23.74	20.52	23.19	23.53	25.86	22.26	22.64	22.59	21.90	22.07	28.63	24.00	25.64	24.54
	ROI4	23.61	19.40	21.52	21.62	24.57	20.85	21.20	21.28	20.56	20.72	26.73	22.54	24.23	22.58

Table 5. MSSIM values for DN images

SAR data name DN	ROI	Guided Filter	SAR- BM3D	Enhanced Lee	i-DWT	Refined Lee	Lee Sigma	Frost	Gamma Map	Median	Enhanced Frost	Lee	Bilateral	SNN	SRAD
Kobuleti 25.07.2018	ROI1	0.706	<i>0.921</i>	0.317	0.064	<i>0.793</i>	0.360	0.330	0.317	0.326	0.998	0.467	0.615	0.757	0.177
	ROI2	0.724	<i>0.942</i>	0.316	0.042	<i>0.793</i>	0.354	0.330	0.316	0.329	0.999	0.463	0.620	0.760	0.167
	ROI3	0.745	<i>0.956</i>	0.319	0.031	<i>0.802</i>	0.356	0.332	0.319	0.335	0.999	0.447	0.636	0.761	0.160
	ROI4	0.883	<i>0.985</i>	0.329	0.035	<i>0.812</i>	0.391	0.343	0.329	0.342	1.000	0.475	0.694	0.765	0.169
Kobuleti 20.07.2019	ROI1	0.658	<i>0.887</i>	0.317	0.064	<i>0.792</i>	0.378	0.331	0.317	0.327	0.997	0.477	0.609	0.757	0.179
	ROI2	0.800	<i>0.968</i>	0.319	0.037	<i>0.798</i>	0.349	0.331	0.317	0.332	1.000	0.453	0.643	0.759	0.164
	ROI3	0.680	<i>0.928</i>	0.293	0.025	<i>0.781</i>	0.325	0.306	0.292	0.309	0.999	0.443	0.596	0.749	0.146
	ROI4	0.783	<i>0.963</i>	0.306	0.029	<i>0.793</i>	0.338	0.319	0.306	0.322	1.000	0.444	0.629	0.755	0.155
Rize 20.07.2019	ROI1	0.334	0.570	0.263	0.035	<i>0.763</i>	0.304	0.276	0.263	0.273	0.975	0.444	0.524	<i>0.731</i>	0.000
	ROI2	0.312	0.538	0.254	0.025	<i>0.757</i>	0.277	0.267	0.253	0.262	0.971	0.438	0.518	<i>0.727</i>	0.134
	ROI3	0.412	0.693	0.240	0.019	<i>0.748</i>	0.266	0.253	0.240	0.251	0.990	0.430	0.513	<i>0.723</i>	0.123
	ROI4	0.330	0.612	0.285	0.027	<i>0.775</i>	0.313	0.299	0.285	0.297	0.969	0.446	0.555	<i>0.744</i>	0.147
Rize 25.07.2018	ROI1	0.728	<i>0.923</i>	0.306	0.056	<i>0.786</i>	0.366	0.319	0.306	0.319	0.999	0.466	0.605	0.755	0.167
	ROI2	0.746	<i>0.949</i>	0.284	0.032	<i>0.770</i>	0.308	0.296	0.283	0.294	1.000	0.433	0.593	0.743	0.145
	ROI3	0.696	<i>0.931</i>	0.281	0.022	<i>0.774</i>	0.306	0.293	0.281	0.294	1.000	0.427	0.584	0.743	0.140
	ROI4	0.753	<i>0.957</i>	0.329	0.031	<i>0.802</i>	0.355	0.342	0.329	0.346	0.999	0.449	0.640	0.766	0.162
Rize 31.08.2018	ROI1	0.669	<i>0.910</i>	0.308	0.046	<i>0.787</i>	0.350	0.319	0.306	0.317	0.998	0.455	0.599	0.753	0.164
	ROI2	0.650	<i>0.910</i>	0.288	0.026	<i>0.776</i>	0.314	0.301	0.287	0.298	0.998	0.437	0.580	0.745	0.145
	ROI3	0.722	<i>0.949</i>	0.330	0.033	<i>0.803</i>	0.366	0.343	0.330	0.342	1.000	0.457	0.640	0.765	0.168
	ROI4	0.784	<i>0.965</i>	0.303	0.026	<i>0.787</i>	0.330	0.316	0.302	0.315	0.999	0.440	0.626	0.754	0.147

Table 6. ENL values over homogenous DN subsets

SAR data name DN	ROI	Guided Filter	SAR- BM3D	Enhanced Lee	i-DWT	Refined Lee	Lee Sigma	Frost	Gamma Map	Median	Enhanced Frost	Lee	Bilateral	SNN	SRAD
Kobuleti 25.07.2018	ROI3	67.95	22.43	84.36	741.94	41.99	76.27	83.59	84.49	73.76	17.68	101.44	52.25	41.03	185.96
	ROI4	39.04	18.30	74.04	482.35	37.59	64.71	73.28	74.10	65.74	16.33	86.27	44.36	37.17	154.30
Kobuleti 20.07.2019	ROI3	92.86	25.55	101.15	3545.55	47.59	90.06	100.15	101.35	86.28	18.08	122.49	60.24	45.32	261.80
	ROI4	62.80	22.03	91.52	1842.81	44.23	80.57	90.69	91.73	79.04	17.83	110.43	54.71	42.93	218.06
Rize 20.07.2019	ROI3	208.95	48.02	110.91	2514.65	52.89	103.07	110.05	111.31	94.04	17.57	127.89	67.94	48.20	271.16
	ROI4	221.41	53.84	90.16	2033.04	45.07	82.02	89.41	90.43	78.55	16.17	104.75	57.38	42.04	206.45
Rize 25.07.2018	ROI3	92.30	26.44	108.19	3576.02	51.23	96.15	107.46	108.64	93.22	18.90	133.14	64.39	48.55	281.89
	ROI4	69.92	22.80	88.77	1850.42	43.62	78.65	88.05	89.07	76.64	18.05	108.91	53.68	41.80	215.12
Rize 31.08.2018	ROI3	92.30	26.44	108.19	1960.80	51.23	96.15	107.46	108.64	93.22	18.90	133.14	64.39	48.55	281.89
	ROI4	69.92	22.80	88.77	1893.84	43.62	78.65	88.05	89.07	76.64	18.05	108.91	53.68	41.80	215.12

Table 7. ENL values over homogenous NRCS subsets

SAR data name NRCS	ROI	Guided Filter	SAR- BM3D	Enhanced Lee	i-DWT	Refined Lee	Lee Sigma	Frost	Gamma Map	Median	Enhanced Frost	Lee	Bilateral	SNN	SRAD
Kobuleti 25.07.2018	ROI3	18.40	9.03	14.33	17.30	8.51	13.76	15.41	9.90	13.94	16.50	8.35	10.65	7.79	11.23
	ROI4	8.20	6.44	12.75	15.70	7.87	11.78	13.84	12.37	12.91	14.78	7.65	9.76	7.36	10.10
Kobuleti 20.07.2019	ROI3	27.27	12.47	10.89	8.84	7.74	12.41	13.55	11.53	11.90	14.97	5.96	9.36	6.50	6.59
	ROI4	16.65	10.71	13.43	4.54	8.38	13.34	15.01	13.05	13.54	16.18	7.54	10.32	7.49	9.50
Rize 20.07.2019	ROI3	46.78	8.28	6.51	9.89	16.99	11.02	10.82	9.93	9.07	12.46	3.76	7.77	5.03	3.58
	ROI4	56.64	8.76	11.15	12.89	7.82	12.10	13.33	11.73	12.02	14.53	6.17	9.36	6.70	7.06
Rize 25.07.2018	ROI3	28.57	13.45	13.97	15.22	9.11	14.55	16.26	13.26	14.54	17.62	7.49	11.04	7.77	9.07
	ROI4	20.39	12.17	16.25	22.67	9.43	15.04	17.05	14.78	15.18	18.15	9.50	11.59	8.40	13.70
Rize 31.08.2018	ROI3	20.35	9.67	11.13	10.73	7.50	11.47	12.90	11.25	11.93	14.04	6.53	9.00	6.59	7.75
	ROI4	17.14	12.91	14.94	17.46	9.14	14.73	16.41	14.08	15.02	17.64	8.35	11.15	8.07	11.12

Table 8. EC values for DN images

SAR data name DN	ROI	Guided Filter	SAR - BM3D	Enhanced Lee	DWT	Refined Lee	Lee Sigma	Frost	Gamma Map	Median	Enhanced Frost	Lee	Bilateral	SNN	SRAD
Kobuleti 25.07.2018	ROI1	0.984	0.971	0.360	0.224	0.923	0.389	0.392	0.361	0.364	0.999	0.796	0.801	0.893	0.379
	ROI2	0.989	0.975	0.376	0.240	0.923	0.396	0.407	0.377	0.387	1.000	0.805	0.802	0.898	0.393
	ROI3	0.991	0.980	0.390	0.260	0.928	0.408	0.419	0.390	0.399	0.999	0.797	0.817	0.897	0.405
	ROI4	0.995	0.994	0.371	0.259	0.932	0.403	0.405	0.371	0.386	1.000	0.806	0.860	0.897	0.406
Kobuleti 20.07.2019	ROI1	0.978	0.957	0.355	0.264	0.923	0.391	0.387	0.356	0.362	0.999	0.805	0.795	0.893	0.389
	ROI2	0.992	0.987	0.383	0.270	0.924	0.411	0.414	0.384	0.393	1.000	0.801	0.826	0.896	0.401
	ROI3	0.989	0.968	0.369	0.239	0.921	0.389	0.400	0.370	0.373	0.999	0.807	0.795	0.895	0.397
	ROI4	0.992	0.985	0.381	0.255	0.925	0.406	0.412	0.382	0.392	1.000	0.800	0.821	0.897	0.401
Rize 20.07.2019	ROI1	0.939	0.796	0.326	0.227	0.917	0.352	0.360	0.328	0.329	0.875	0.800	0.742	0.887	0.401
	ROI2	0.941	0.782	0.320	0.226	0.915	0.354	0.612	0.325	0.982	0.801	0.739	0.887	0.779	0.375
	ROI3	0.970	0.854	0.325	0.221	0.911	0.347	0.359	0.326	0.328	0.995	0.815	0.742	0.886	0.374
	ROI4	0.948	0.813	0.344	0.238	0.919	0.364	0.378	0.345	0.348	0.982	0.805	0.755	0.893	0.383
Rize 25.07.2018	ROI1	0.983	0.974	0.368	0.234	0.922	0.393	0.398	0.369	0.374	1.000	0.802	0.797	0.894	0.384
	ROI2	0.991	0.980	0.357	0.288	0.913	0.369	0.389	0.359	0.360	1.000	0.803	0.793	0.893	0.391
	ROI3	0.990	0.973	0.351	0.216	0.918	0.375	0.383	0.353	0.360	1.000	0.798	0.789	0.894	0.391
	ROI4	0.991	0.981	0.404	0.264	0.925	0.423	0.433	0.406	0.415	0.999	0.801	0.815	0.899	0.413
Rize 31.08.2018	ROI1	0.985	0.964	0.364	0.238	0.925	0.389	0.395	0.365	0.369	0.999	0.805	0.793	0.895	0.389
	ROI2	0.987	0.960	0.374	0.235	0.917	0.388	0.404	0.375	0.373	0.999	0.801	0.783	0.894	0.390
	ROI3	0.989	0.976	0.420	0.262	0.922	0.442	0.448	0.420	0.421	1.000	0.801	0.816	0.901	0.422
	ROI4	0.993	0.986	0.393	0.241	0.924	0.412	0.425	0.395	0.402	1.000	0.806	0.821	0.899	0.403

Table 9. EC values for NRCS

SAR data name NRCS	ROI	Guided Filter	SAR-BM3D	Enhanced Lee	DWT	Refined Lee	Lee Sigma	Frost	Gamma Map	Median	Enhanced Frost	Lee	Bilateral	SNN	SRAD
Kobuleti 25.07.2018	ROI1	0.958	0.108	0.644	0.755	0.917	0.417	0.531	0.433	0.360	0.356	0.982	0.755	0.897	0.800
	ROI2	0.964	0.105	0.630	0.735	0.918	0.417	0.538	0.521	0.387	0.375	0.982	0.757	0.900	0.785
	ROI3	0.975	0.103	0.593	0.687	0.927	0.435	0.540	0.693	0.406	0.398	0.978	0.774	0.902	0.747
	ROI4	0.988	0.101	0.596	0.707	0.930	0.428	0.527	0.534	0.387	0.369	0.978	0.787	0.901	0.758
Kobuleti 20.07.2019	ROI1	0.940	0.100	0.656	0.763	0.915	0.426	0.532	0.376	0.358	0.351	0.983	0.753	0.896	0.809
	ROI2	0.961	0.095	0.696	0.719	0.911	0.408	0.554	0.522	0.372	0.365	0.986	0.146	0.897	0.837
	ROI3	0.976	0.105	0.624	0.792	0.918	0.426	0.541	0.539	0.396	0.382	0.981	0.767	0.900	0.781
	ROI4	0.977	0.103	0.616	0.727	0.918	0.537	0.733	0.395	0.382	0.981	0.162	0.769	0.899	0.770
Rize 20.07.2019	ROI1	0.639	0.104	0.797	0.873	0.902	0.379	0.569	0.431	0.321	0.318	0.991	0.724	0.891	0.906
	ROI2	0.593	0.102	0.807	0.881	0.900	0.350	0.569	0.448	0.315	0.308	0.992	0.718	0.891	0.913
	ROI3	0.812	0.096	0.824	0.889	0.327	0.372	0.585	0.469	0.319	0.316	0.993	0.712	0.891	0.921
	ROI4	0.644	0.101	0.670	0.778	0.909	0.393	0.534	0.502	0.348	0.344	0.985	0.741	0.897	0.825
Rize 25.07.2018	ROI1	0.965	0.102	0.635	0.743	0.915	0.416	0.530	0.396	0.369	0.363	0.983	0.742	0.897	0.794
	ROI2	0.976	0.090	0.613	0.733	0.902	0.376	0.520	0.492	0.360	0.354	0.983	0.736	0.896	0.788
	ROI3	0.968	0.094	0.631	0.740	0.909	0.397	0.525	0.532	0.359	0.350	0.983	0.742	0.897	0.796
	ROI4	0.977	0.102	0.560	0.652	0.919	0.436	0.534	0.552	0.417	0.404	0.976	0.767	0.903	0.718
Rize 31.08.2018	ROI1	0.950	0.097	0.638	0.745	0.919	0.411	0.532	0.458	0.370	0.364	0.983	0.752	0.899	0.796
	ROI2	0.949	0.108	0.668	0.765	0.907	0.407	0.548	0.523	0.372	0.372	0.984	0.744	0.898	0.815
	ROI3	0.966	0.121	0.670	0.747	0.913	0.461	0.576	0.556	0.423	0.421	0.982	0.774	0.905	0.800
	ROI4	0.980	0.097	0.610	0.694	0.920	0.432	0.545	0.555	0.405	0.395	0.980	0.766	0.901	0.759

Table 10. EPI values for DN

SAR Data Name DN	ROI	Guided Filter	SAR - BM3D	Enhanced Lee	i-DWT	Refined Lee	Lee Sigma	Frost	Gamma Map	Median	Enhanced Frost	Lee	Bilateral	SNN	SRAD
Kobuleti 25.07.2018	ROI1	0.9882	0.8514	0.2007	0.0289	0.7416	0.0786	0.1574	0.2023	0.0875	0.9958	0.8904	0.3309	0.6462	0.1641
	ROI2	0.9930	0.8617	0.1938	0.0255	0.7382	0.0928	0.1504	0.1955	0.0768	0.9970	0.8917	0.3415	0.6452	0.1689
	ROI3	0.9928	0.8867	0.1998	0.0311	0.7372	0.0969	0.1544	0.2009	0.0758	0.9952	0.8834	0.4017	0.6199	0.1812
	ROI4	0.9955	0.9469	0.1922	0.0305	0.7373	0.0671	0.1431	0.1930	0.0702	0.9995	0.8974	0.5516	0.6151	0.1872
Kobuleti 20.07.2019	ROI1	0.9777	0.8168	0.2031	0.0295	0.7418	0.0587	0.1598	0.2043	0.0888	0.9916	0.8883	0.2971	0.6494	0.1623
	ROI2	0.9939	0.9102	0.1989	0.0253	0.7375	0.0784	0.1544	0.2000	0.0787	0.9979	0.8942	0.4380	0.6309	0.1766
	ROI3	0.9925	0.8416	0.1954	0.0291	0.7405	0.1011	0.1538	0.1976	0.0861	0.9943	0.8905	0.2988	0.6467	0.1644
	ROI4	0.9940	0.9000	0.1918	0.0254	0.7409	0.0793	0.1476	0.1929	0.0722	0.9990	0.8931	0.4055	0.6375	0.1731
Rize 20.07.2019	ROI1	0.9816	0.5418	0.2204	0.0276	0.7515	0.1015	0.1791	0.2219	0.1065	0.9400	0.8429	0.0622	0.6737	0.1246
	ROI2	0.9847	0.5353	0.2275	0.0259	0.7505	0.1105	0.1857	0.2285	0.1079	0.9074	0.8365	0.0621	0.6719	0.1432
	ROI3	0.9881	0.6271	0.2286	0.0275	0.7480	0.1374	0.1902	0.2322	0.1137	0.9704	0.8725	0.0835	0.6837	0.1431
	ROI4	0.9838	0.5658	0.2130	0.0196	0.7413	0.1065	0.1699	0.2158	0.0989	0.8915	0.8283	0.1301	0.6505	0.1608
Rize 25.07.2018	ROI1	0.9839	0.8639	0.1896	0.0248	0.7454	0.0689	0.1493	0.1913	0.0818	0.9972	0.8986	0.3185	0.6629	0.1574
	ROI2	0.9929	0.8810	0.1944	0.0314	0.7394	0.1106	0.1555	0.1975	0.0865	1.0000	0.8959	0.3267	0.6568	0.1609
	ROI3	0.9929	0.8492	0.2056	0.0241	0.7459	0.1003	0.1663	0.2074	0.0948	0.9981	0.8916	0.2894	0.6602	0.1579
	ROI4	0.9933	0.8883	0.1812	0.0280	0.7350	0.0776	0.1393	0.1842	0.0683	0.9942	0.8836	0.3874	0.6249	0.1837
Rize 31.08.2018	ROI1	0.9880	0.8282	0.1952	0.0287	0.7467	0.0810	0.1530	0.1962	0.0869	0.9952	0.8903	0.2832	0.6537	0.1627
	ROI2	0.9924	0.8150	0.1849	0.0130	0.7463	0.1031	0.1461	0.1885	0.0820	0.9938	0.8901	0.2532	0.6602	0.1575
	ROI3	0.9918	0.8716	0.1954	0.0210	0.7295	0.0660	0.1521	0.1988	0.0758	0.9969	0.8797	0.3887	0.6192	0.1837
	ROI4	0.9946	0.9034	0.1845	0.0278	0.7414	0.0877	0.1420	0.1868	0.0727	0.9975	0.8941	0.4075	0.6401	0.1743

Table 11. EPI values for NRCS

SAR Data Name NRCS	ROI	Guided Filter	SAR - BM3D	Enhanced Lee	i-DWT	Refined Lee	Lee Sigma	Frost	Gamma Map	Median	Enhanced Frost	Lee	Bilateral	SNN	SRAD
Kobuleti 25.07.2018	ROI1	<i>0.9676</i>	0.0188	0.4172	0.4163	<i>0.7279</i>	0.0189	0.1006	0.0104	0.0857	0.2052	0.9853	0.1222	<i>0.6470</i>	0.5103
	ROI2	<i>0.9748</i>	0.0179	0.3709	0.3859	<i>0.7295</i>	0.0098	0.0917	0.1342	0.0726	0.1963	0.9848	0.1289	<i>0.6445</i>	0.4797
	ROI3	<i>0.9786</i>	0.0214	0.2646	0.3261	<i>0.7292</i>	0.0077	0.0703	0.3850	0.0685	0.1970	0.9824	0.1906	<i>0.6193</i>	0.4199
	ROI4	<i>0.9878</i>	0.0223	0.2882	0.3378	<i>0.7335</i>	0.0213	0.0775	0.1432	0.0668	0.1987	0.9813	0.2280	<i>0.6130</i>	0.4261
Kobuleti 20.07.2019	ROI1	<i>0.9461</i>	0.0132	0.4487	0.4374	<i>0.7257</i>	0.0472	0.1100	0.1369	0.0871	0.2069	0.9854	0.1172	<i>0.6491</i>	0.5306
	ROI2	<i>0.9795</i>	0.0197	0.3284	0.3692	<i>0.7286</i>	0.0257	0.0756	0.1098	0.0760	0.2057	0.9842	0.1757	<i>0.6291</i>	0.4601
	ROI3	<i>0.9740</i>	0.0198	0.5098	0.4702	<i>0.7156</i>	0.0223	0.1384	0.1585	0.0837	0.2011	0.9884	0.1046	<i>0.6525</i>	0.5713
	ROI4	<i>0.9800</i>	0.0219	0.3492	0.3704	<i>0.7280</i>	0.0095	0.0896	0.1501	0.0698	0.1967	0.9847	0.1533	<i>0.6370</i>	0.4669
Rize 20.07.2019	ROI1	<i>0.9219</i>	0.0176	0.6986	0.6148	<i>0.7326</i>	0.0026	0.2247	0.0614	0.1032	0.2181	0.9926	0.0069	<i>0.6895</i>	0.7163
	ROI2	<i>0.9238</i>	0.0164	0.7176	0.6272	<i>0.7368</i>	0.0629	0.2364	0.1136	0.1023	0.2220	0.9934	0.0029	<i>0.6940</i>	0.7328
	ROI3	<i>0.9538</i>	0.0177	0.7460	0.6463	0.0267	0.0412	0.2581	0.1353	0.1040	0.2143	0.9939	0.0220	0.7082	0.7527
	ROI4	<i>0.9228</i>	0.0206	0.4653	0.4431	<i>0.7271</i>	0.0102	0.1098	0.1292	0.0983	0.2194	0.9876	0.0751	<i>0.6537</i>	0.5472
Rize 25.07.2018	ROI1	<i>0.9648</i>	0.0187	0.4148	0.4155	<i>0.7268</i>	0.0220	0.0972	0.1063	0.0819	0.1952	0.9859	0.0726	<i>0.6625</i>	0.5135
	ROI2	<i>0.9783</i>	0.0192	0.3801	0.3923	<i>0.7176</i>	0.0567	0.0809	0.1020	0.0870	0.1986	0.9860	0.0677	<i>0.6607</i>	0.4894
	ROI3	<i>0.9780</i>	0.0170	0.3994	0.4108	<i>0.7218</i>	0.0259	0.0833	0.1750	0.0959	0.2127	0.9867	0.0806	<i>0.6606</i>	0.5116
	ROI4	<i>0.9812</i>	0.0182	0.1915	0.2893	<i>0.7235</i>	0.0130	0.0503	0.1497	0.0655	0.1866	0.9812	0.1668	<i>0.6260</i>	0.3839
Rize 31.08.2018	ROI1	<i>0.9616</i>	0.0188	0.4059	0.4076	<i>0.7306</i>	0.0007	0.0941	0.0373	0.0845	0.1997	0.9861	0.0947	<i>0.6538</i>	0.5054
	ROI2	<i>0.9720</i>	0.0207	0.4604	0.4335	<i>0.7261</i>	0.0174	0.1202	0.1496	0.0787	0.1909	0.9875	0.0694	<i>0.6643</i>	0.5339
	ROI3	<i>0.9724</i>	0.0267	0.3915	0.3827	<i>0.7117</i>	0.0150	0.1090	0.1305	0.0748	0.2006	0.9845	0.1949	<i>0.6262</i>	0.4866
	ROI4	<i>0.9832</i>	0.0203	0.3086	0.3470	<i>0.7309</i>	0.0119	0.0776	0.1715	0.0705	0.1896	0.9837	0.1502	<i>0.6412</i>	0.4428

Figure captions

Figure 1. Single-polarization multiplicative speckle model.

Figure 2. The i-DWT workflow for constructing the improved wavelet transformation filter.

Figure 3. Location of the Rize oil seep and the Kobuleti ridge seepage cluster on a SAR Copernicus Sentinel-1 image (31.08.2018).

Figure 4. (a) ROI1 containing heterogeneous water-oil slick area. (b) ROI2 containing heterogeneous water-oceanic structure area. (c) ROI3 containing homogeneous area. (d) ROI4 containing homogeneous area.

Figure 5. The general processing workflow for natural oil slick detection and mapping. The framework has been proposed by Suresh et al. (2015) as the Automatic Seep Location Estimator (ASLE). Pre-processing of current images includes orbit corrections with precise orbit vectors and multilooking for obtaining DN images and, in addition, radiometric calibration for extracting the NRCS values.

Figure 6. Speckle filtering results on the DN Rize 25.07.2018 ROI1 image using (a) Original Image. (b) Median filter (c) Lee filter. (d) Lee Sigma. (e) Enhanced Lee filter. (f) Refined Lee filter. (g) Frost filter. (h) Enhanced Frost filter. (i) Symmetric Nearest Neighbor filter. (j) Bilateral filter. (k) Guided filter. (l) Speckle reducing anisotropic diffusion filter. (m) Improved Discrete Wavelet Transform filter. (n) SAR-BR3D filter, (o) Gamma Map.

Figure 7. Speckle filtering results on the NRCS Rize 25.07.2018 ROI1 image using (a) Original Image. (b) Median filter (c) Lee filter. (d) Lee Sigma. (e) Enhanced Lee filter. (f) Refined Lee filter. (g) Frost filter. (h) Enhanced Frost filter. (i) Symmetric Nearest Neighbor filter. (j) Bilateral filter. (k) Guided filter. (l) Speckle reducing anisotropic diffusion filter. (m) Improved Discrete Wavelet Transform filter. (n) SAR-BR3D filter, (o) Gamma Map.

Figure 8. Speckle filtering results on the DN Rize 25.07.2018 ROI2 image using (a) Original Image. (b) Median filter (c) Lee filter. (d) Lee Sigma. (e) Enhanced Lee filter. (f) Refined Lee filter. (g) Frost filter. (h) Enhanced Frost filter. (i) Symmetric Nearest Neighbor filter. (j) Bilateral filter. (k) Guided filter. (l) Speckle reducing anisotropic diffusion filter. (m) Improved Discrete Wavelet Transform filter. (n) SAR-BR3D filter, (o) Gamma Map.

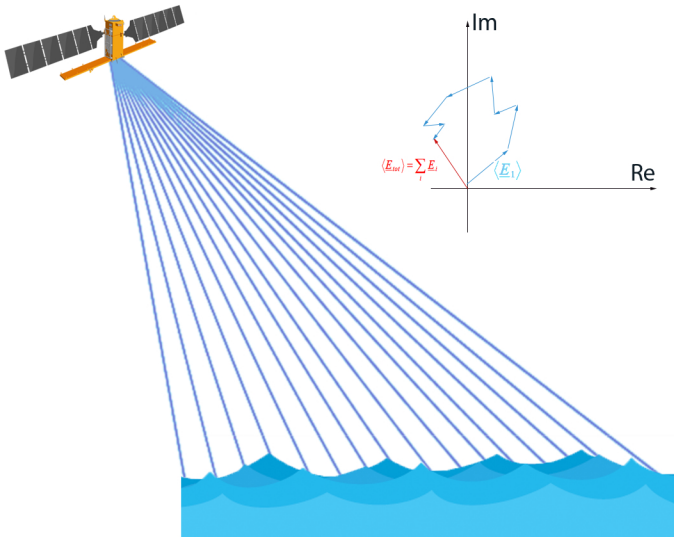
Figure 9. Speckle filtering results on the NRCS Rize 25.07.2018 ROI2 image using (a) Original Image. (b) Median filter (c) Lee filter. (d) Lee Sigma. (e) Enhanced Lee filter. (f) Refined Lee filter. (g) Frost filter. (h) Enhanced Frost filter. (i) Symmetric Nearest Neighbor filter. (j) Bilateral filter. (k) Guided filter. (l) Speckle reducing anisotropic diffusion filter. (m) Improved Discrete Wavelet Transform filter. (n) SAR-BR3D filter, (o) Gamma Map.

Figure 10. Speckle filtering results on the DN Rize 25.07.2018 ROI3 image using (a) Original Image. (b) Median filter (c) Lee filter. (d) Lee Sigma. (e) Enhanced Lee filter. (f) Refined Lee filter. (g) Frost filter. (h) Enhanced Frost filter. (i) Symmetric Nearest Neighbor filter. (j) Bilateral filter. (k) Guided filter. (l) Speckle reducing anisotropic diffusion filter. (m) Improved Discrete Wavelet Transform filter. (n) SAR-BR3D filter, (o) Gamma Map.

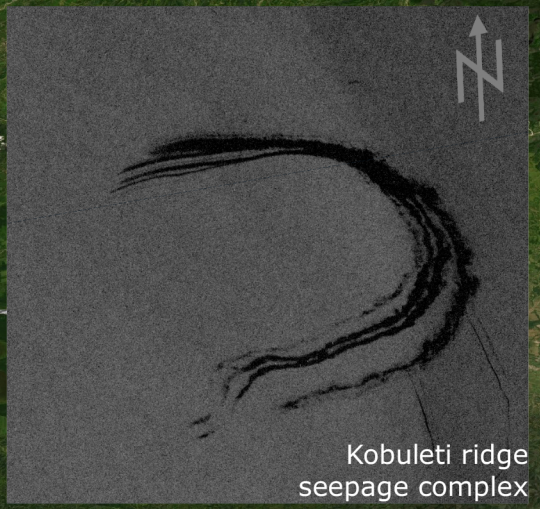
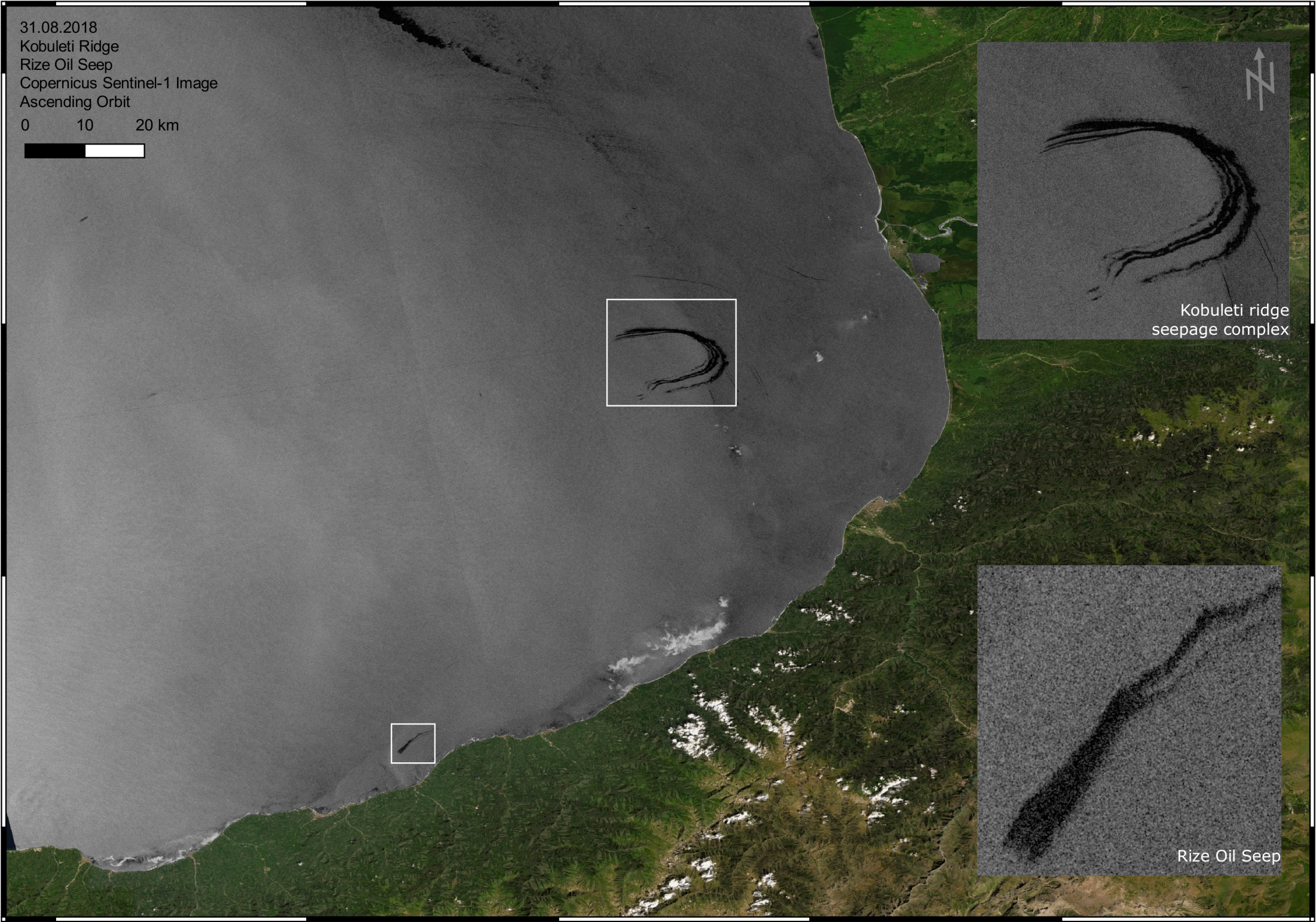
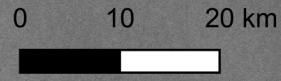
Figure 11. Speckle filtering results on the NRCS Rize 25.07.2018 ROI3 image using (a) Original Image. (b) Median filter (c) Lee filter. (d) Lee Sigma. (e) Enhanced Lee filter. (f) Refined Lee filter. (g) Frost filter. (h) Enhanced Frost filter. (i) Symmetric Nearest Neighbor filter. (j) Bilateral filter. (k) Guided filter. (l) Speckle reducing anisotropic diffusion filter. (m) Improved Discrete Wavelet Transform filter. (n) SAR-BR3D filter, (o) Gamma Map.

Figure 12. Speckle filtering results on the DN Rize 25.07.2018 ROI4 image using (a) Original Image. (b) Median filter (c) Lee filter. (d) Lee Sigma. (e) Enhanced Lee filter. (f) Refined Lee filter. (g) Frost filter. (h) Enhanced Frost filter. (i) Symmetric Nearest Neighbor filter. (j) Bilateral filter. (k) Guided filter. (l) Speckle reducing anisotropic diffusion filter. (m) Improved Discrete Wavelet Transform filter. (n) SAR-BR3D filter, (o) Gamma Map.

Figure 13. Speckle filtering results on the NRCS Rize 25.07.2018 ROI4 image using (a) Original Image. (b) Median filter (c) Lee filter. (d) Lee Sigma. (e) Enhanced Lee filter. (f) Refined Lee filter. (g) Frost filter. (h) Enhanced Frost filter. (i) Symmetric Nearest Neighbor filter. (j) Bilateral filter. (k) Guided filter. (l) Speckle reducing anisotropic diffusion filter. (m) Improved Discrete Wavelet Transform filter. (n) SAR-BR3D filter, (o) Gamma Map.



31.08.2018
Kobuleti Ridge
Rize Oil Seep
Copernicus Sentinel-1 Image
Ascending Orbit



40°0'0"E 40°30'0"E 41°0'0"E 41°30'0"E 42°0'0"E

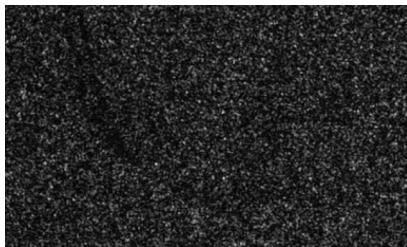
42°30'0"N
42°0'0"N
41°30'0"N
41°0'0"N

Rize 31.08.2018

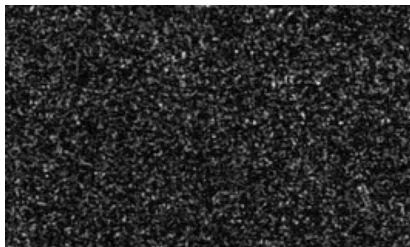
a) ROI1 - Oil slick area



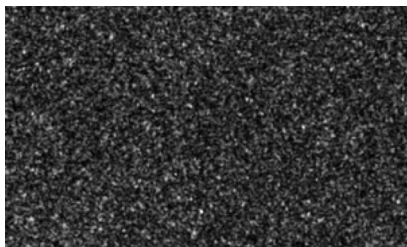
b) ROI2 - Ocean structure area

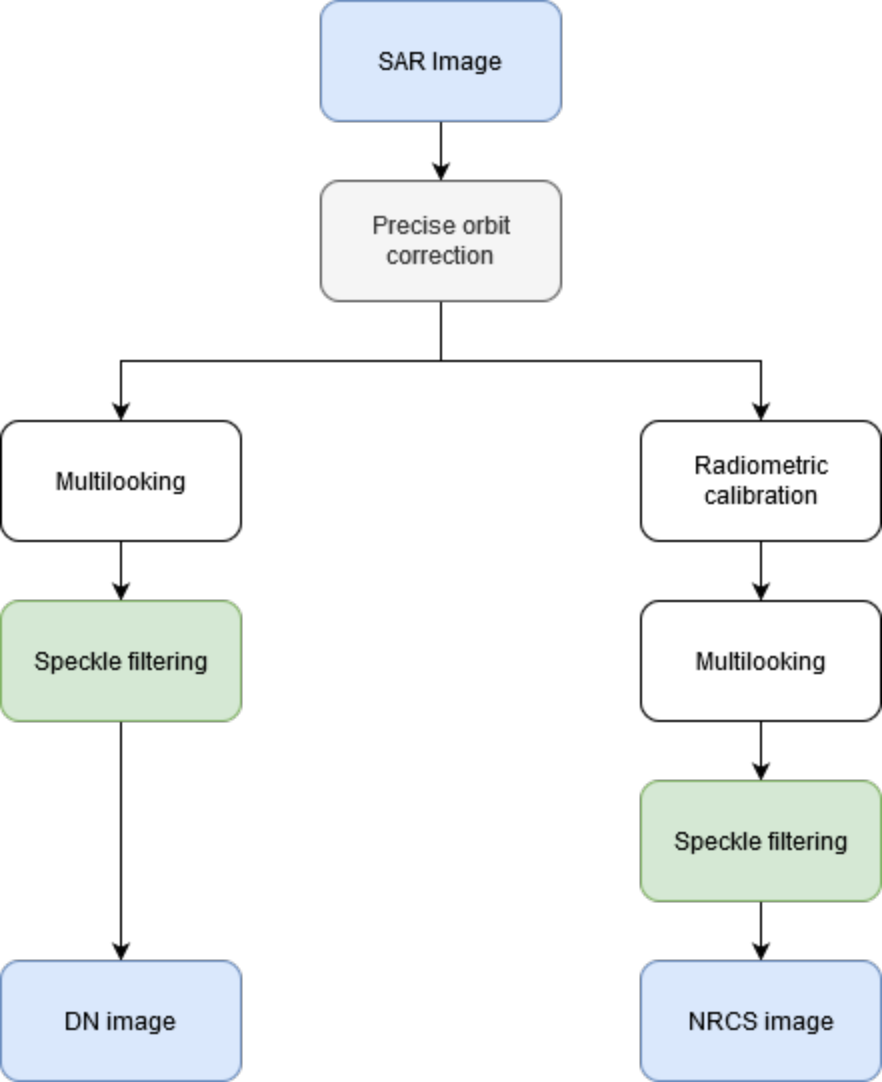


c) ROI3 - Homogenous area

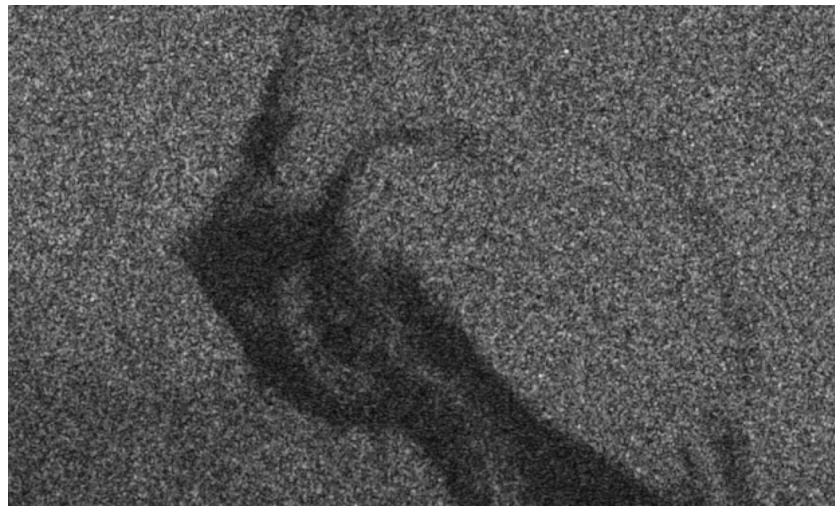


d) ROI4 - Homogenous area

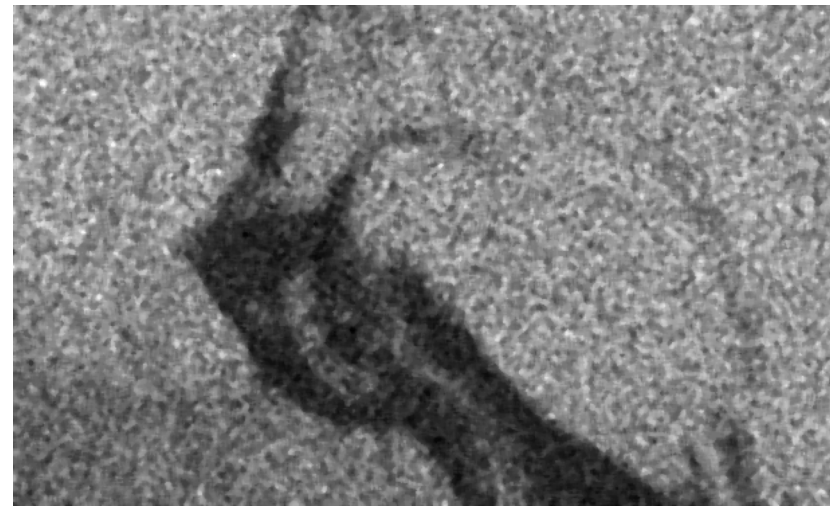




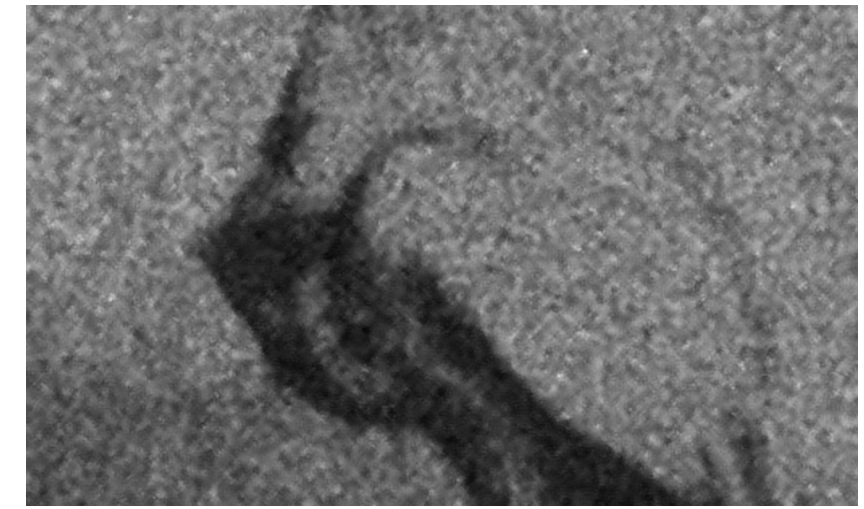
a) DN image



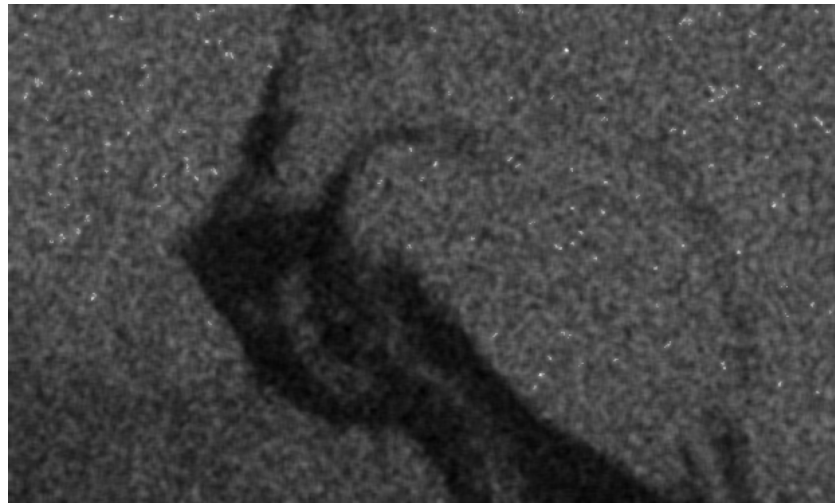
b) Median



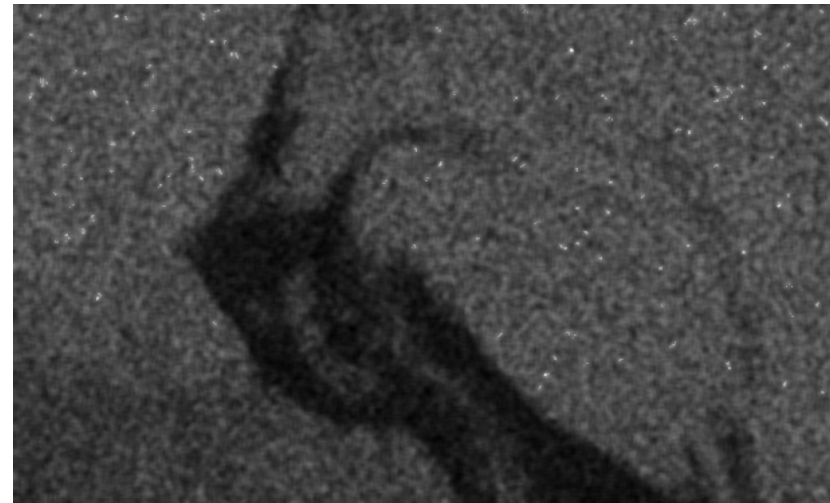
c) Lee



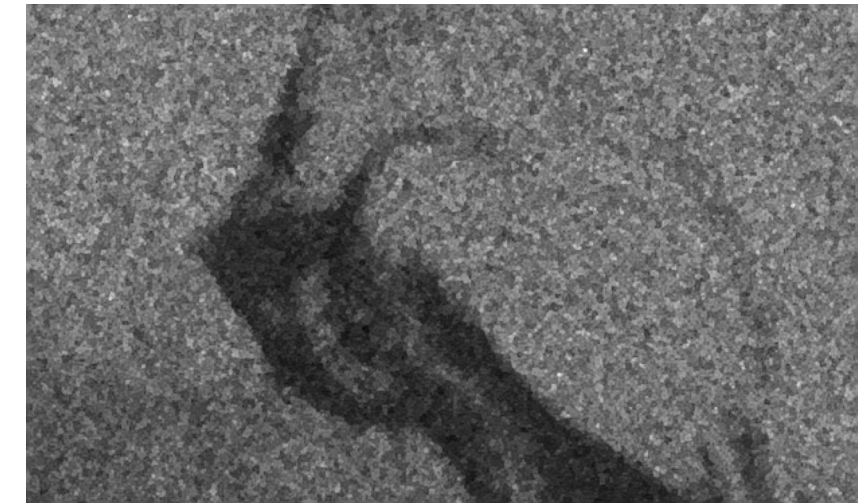
d) Lee Sigma



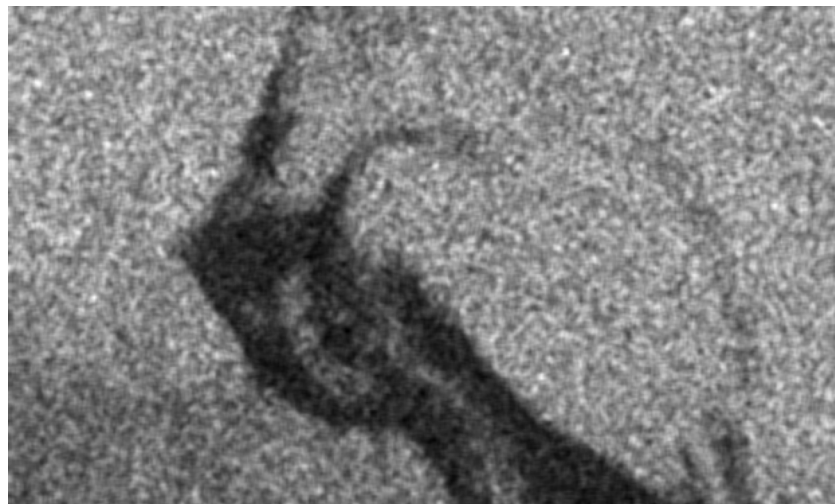
e) Enhanced Lee



f) Refined Lee



g) Frost



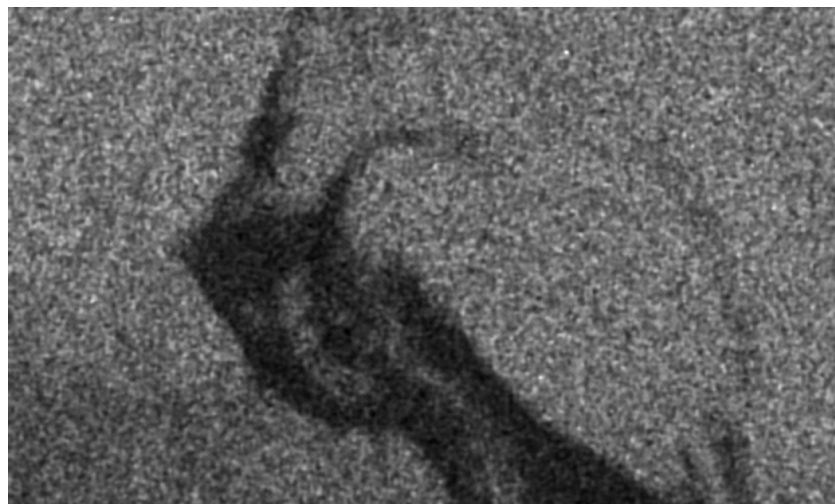
h) Enhanced Frost



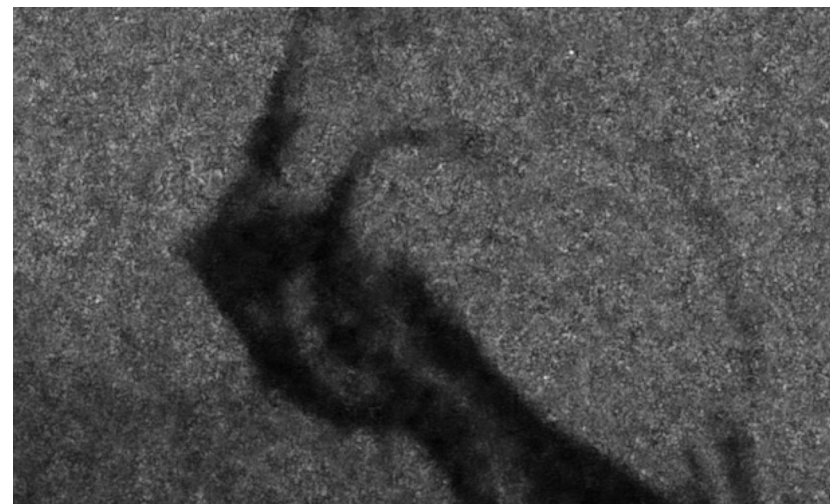
i) SNN



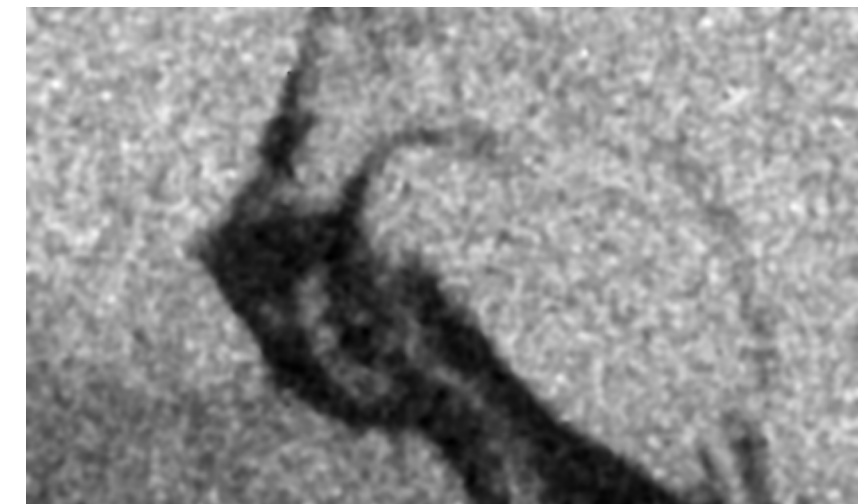
j) Bilateral



k) Guided filter



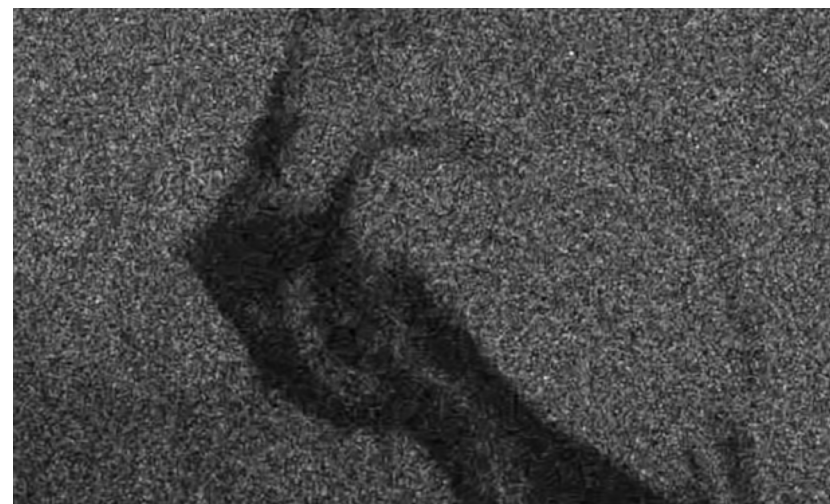
l) SRAD



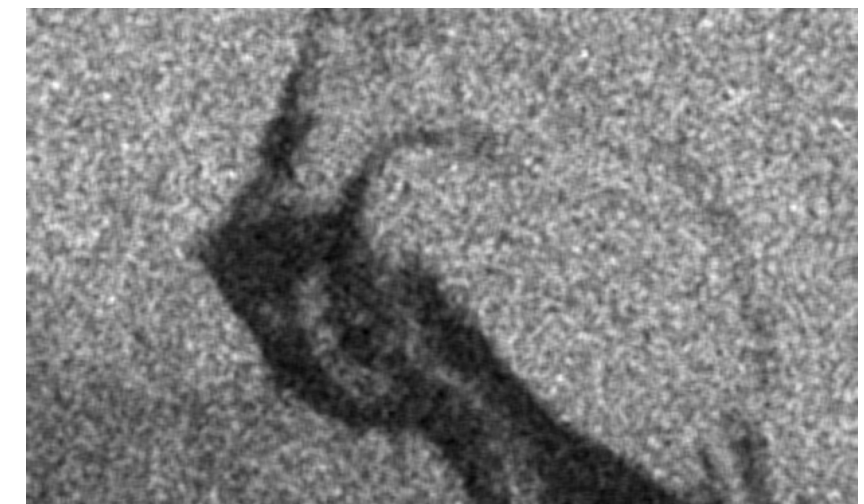
m) Improved DWT



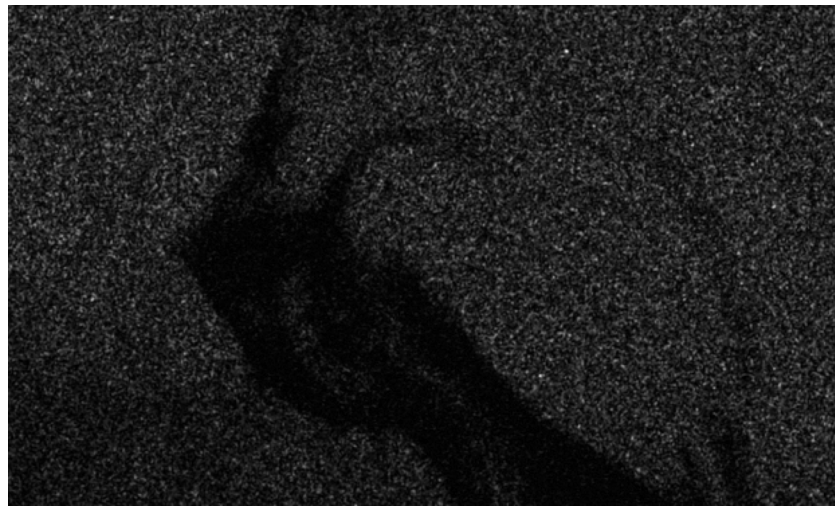
n) SAR BM3D



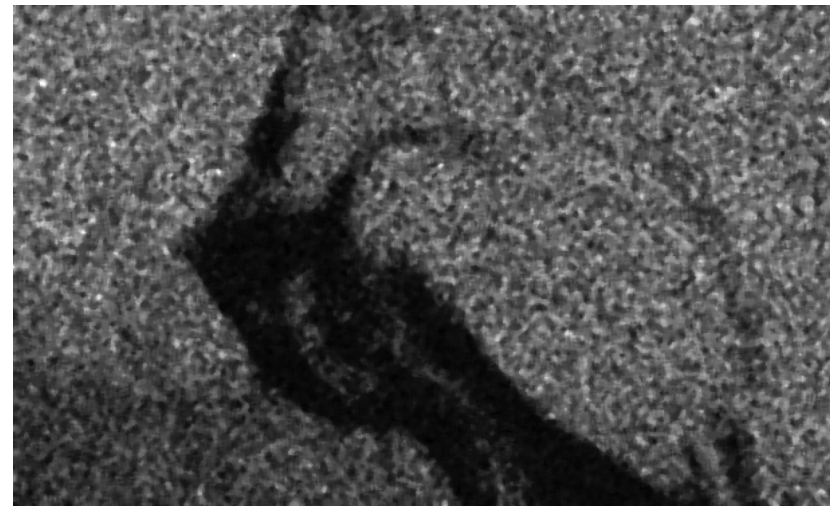
o) Gamma Map



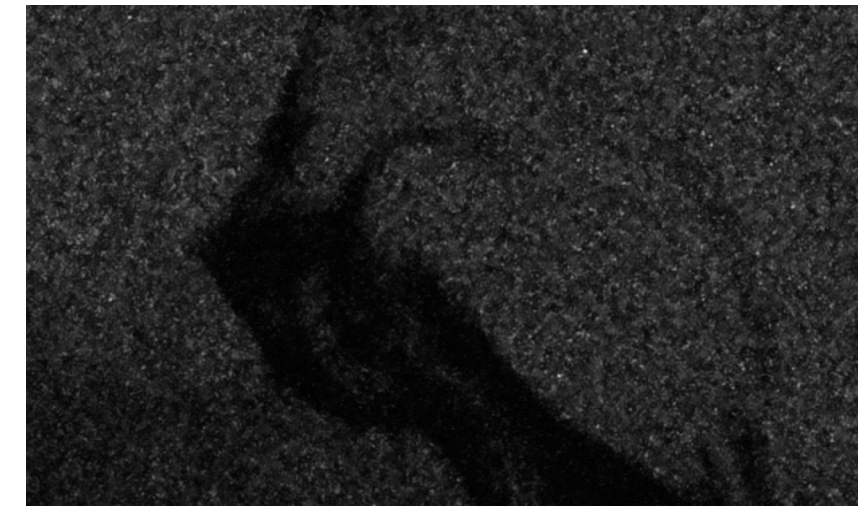
a) NRCS image



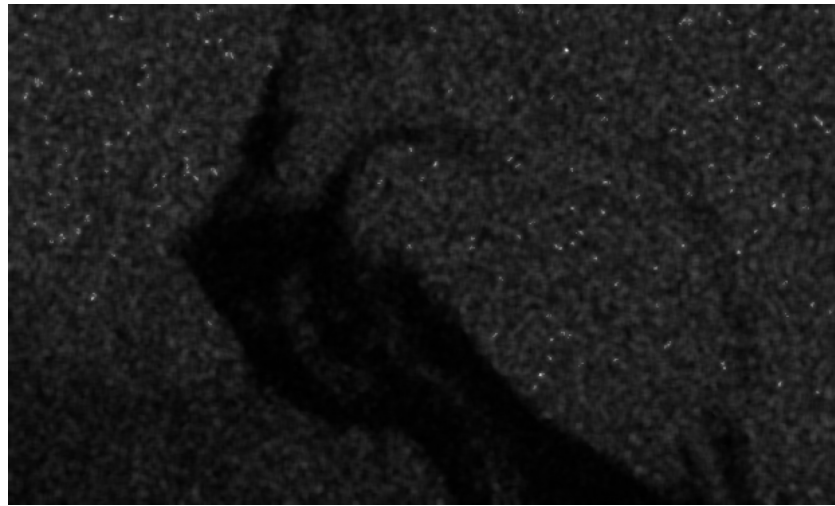
b) Median



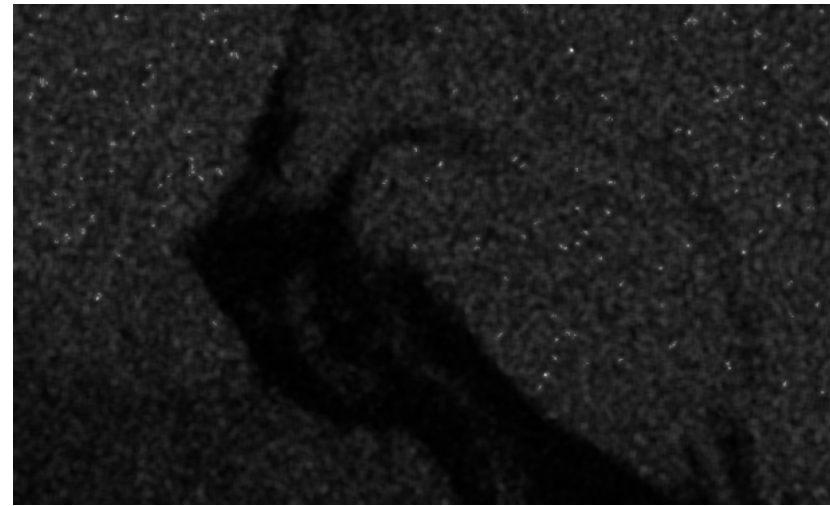
c) Lee



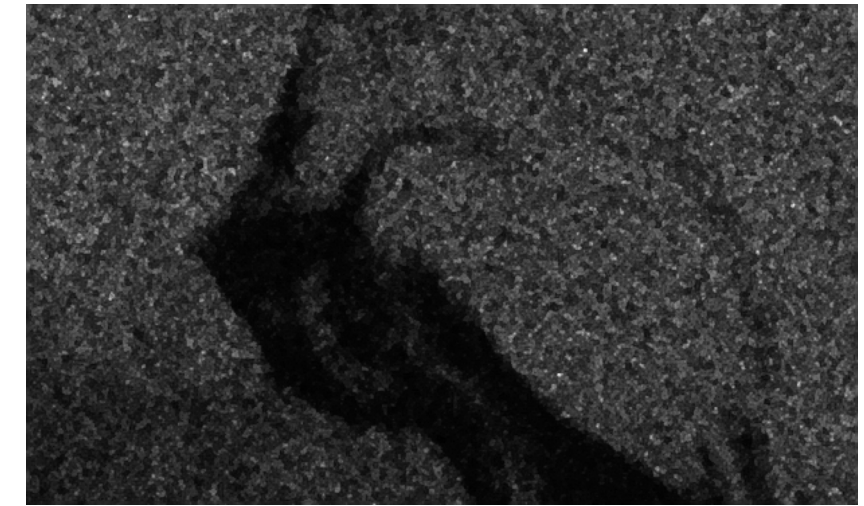
d) Lee Sigma



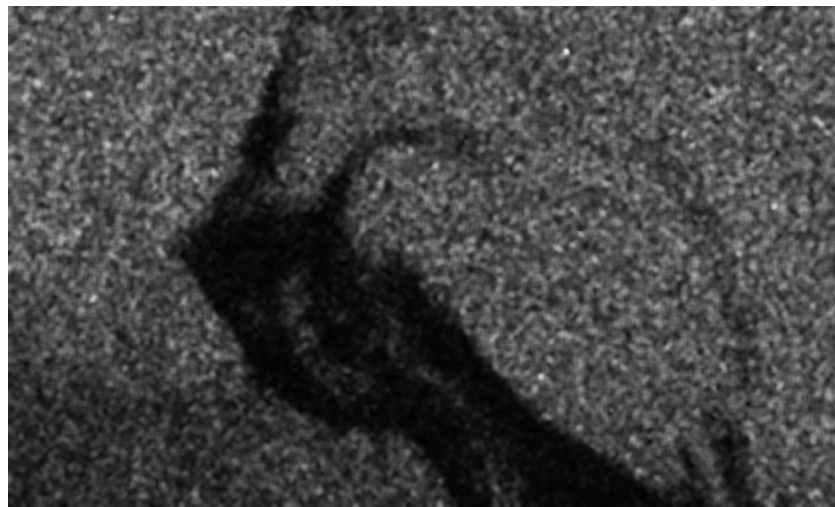
e) Enhanced Lee



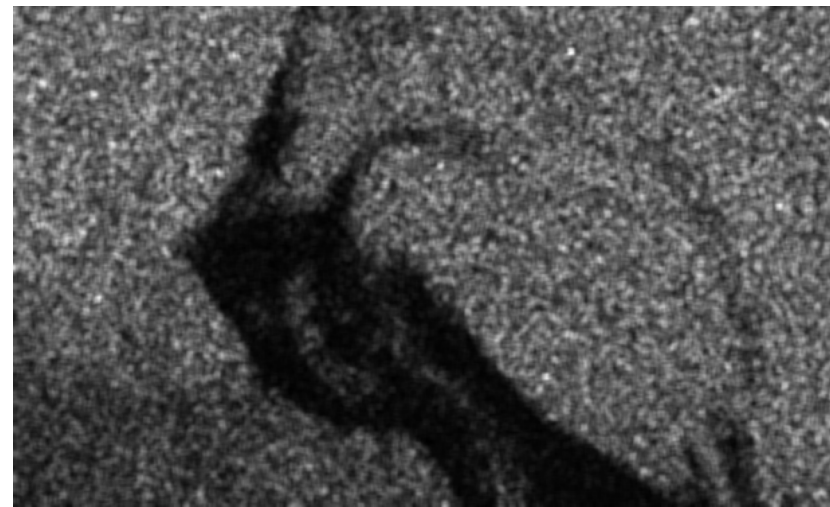
f) Refined Lee



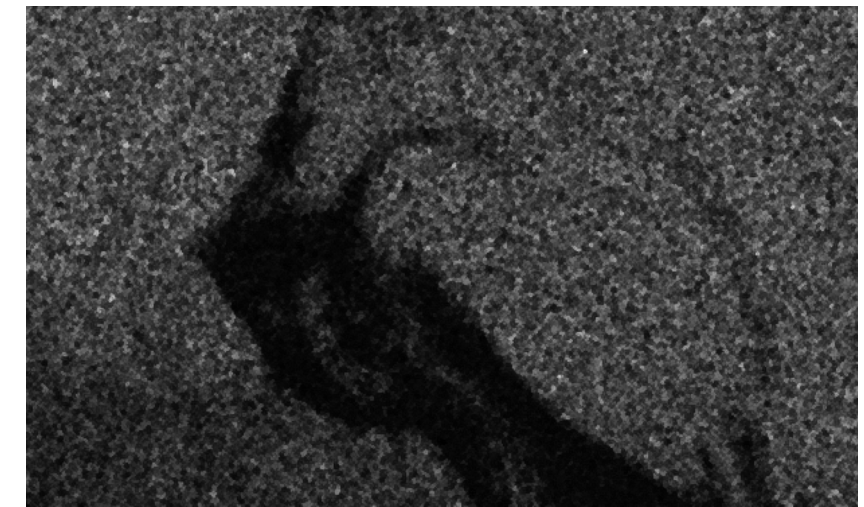
g) Frost



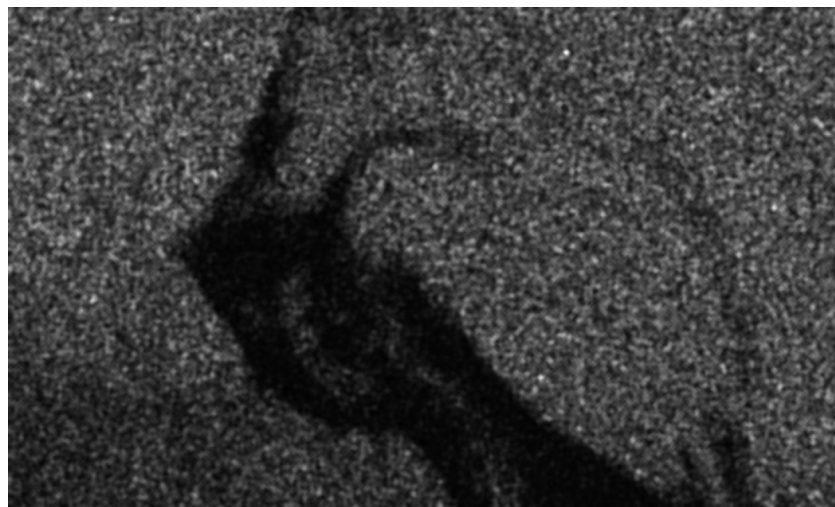
h) Enhanced Frost



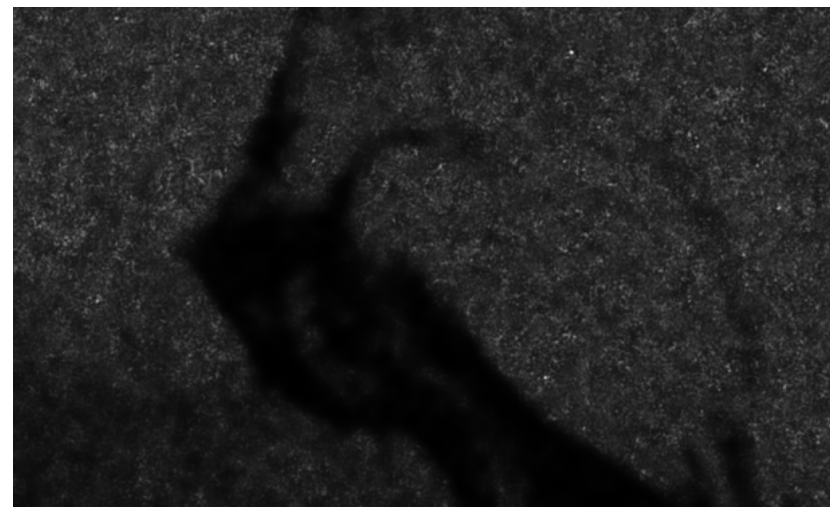
i) SNN



j) Bilateral



k) Guided filter



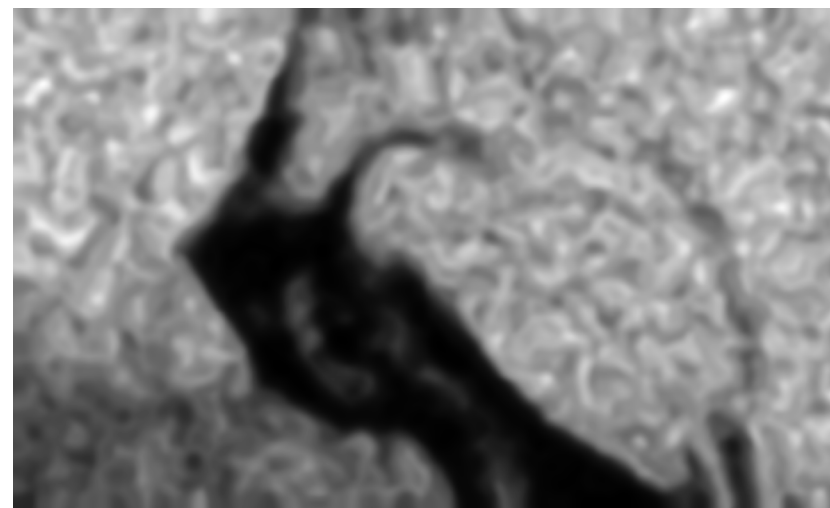
l) SRAD



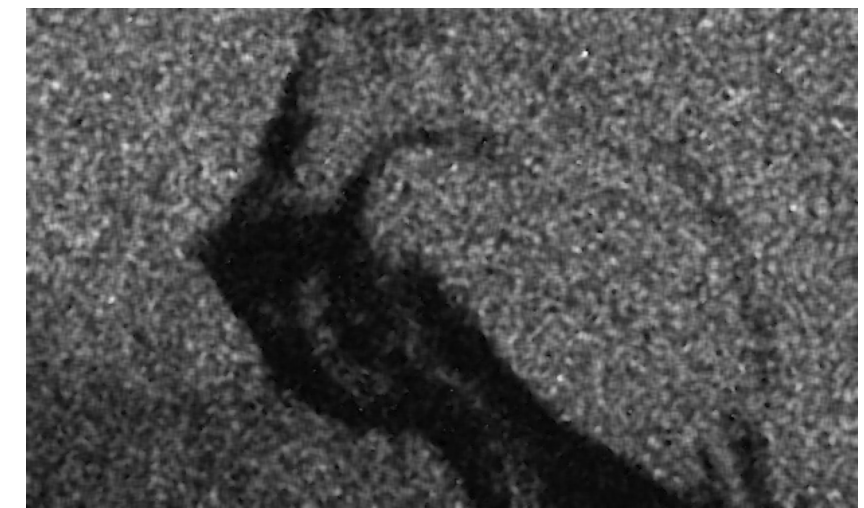
m) Improved DWT



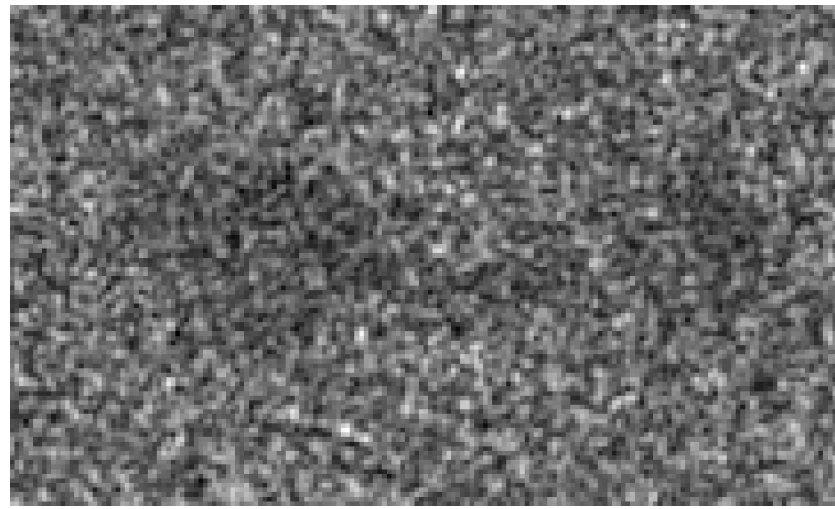
n) SAR BM3D



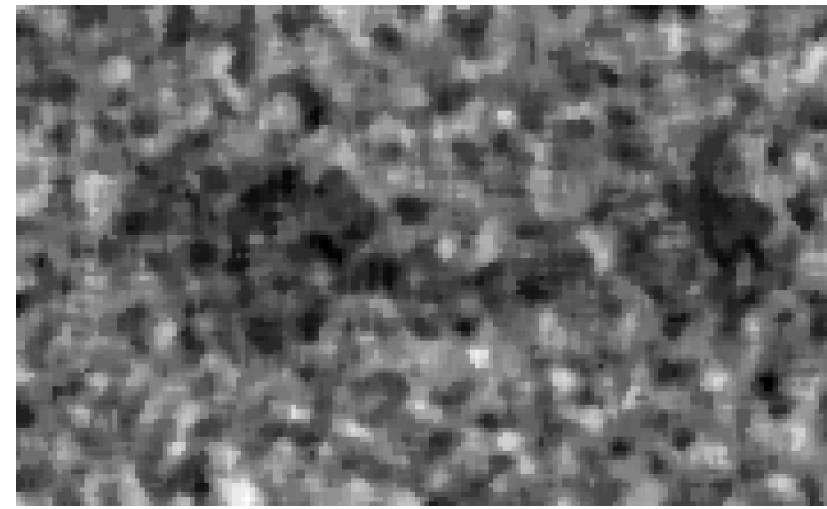
o) Gamma Map



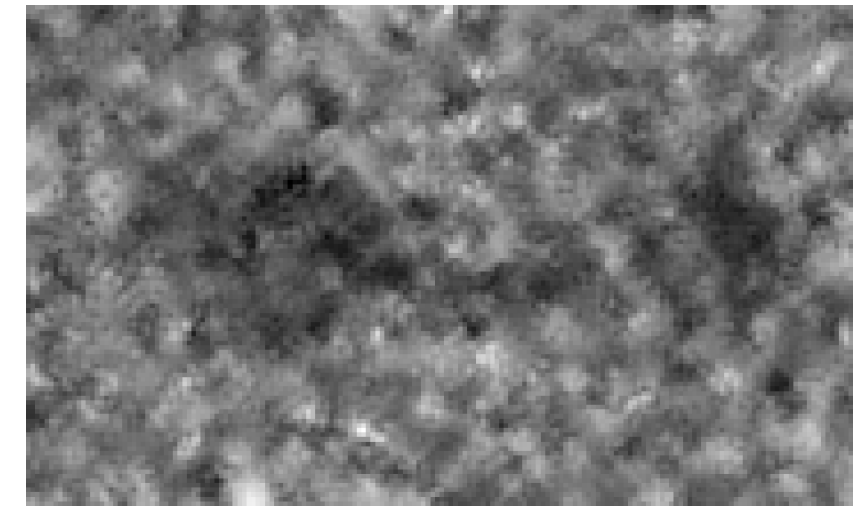
a) NRCS image



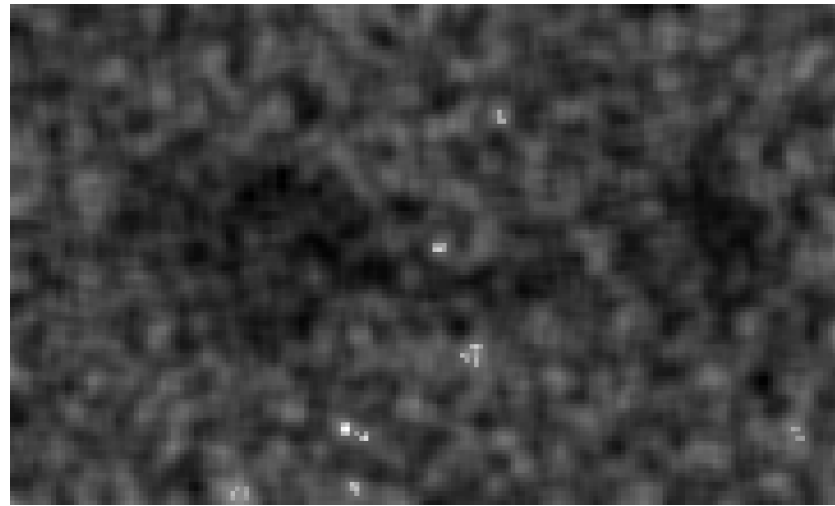
b) Median



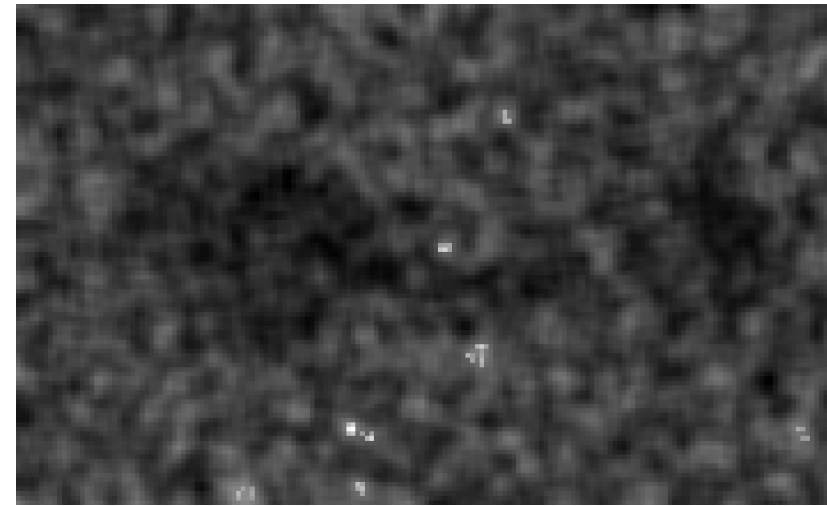
c) Lee



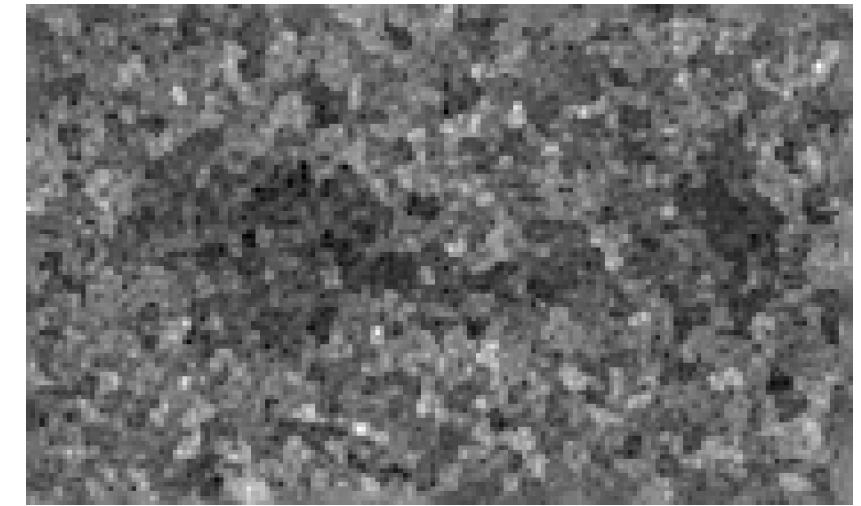
d) Lee Sigma



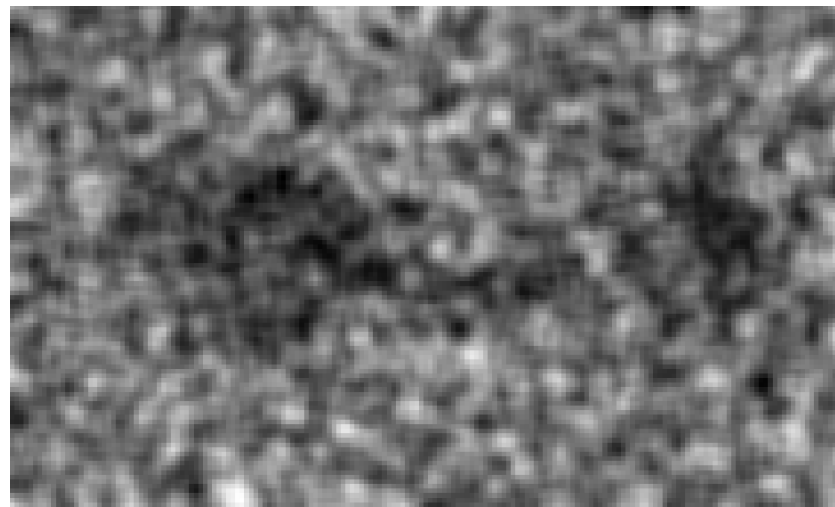
e) Enhanced Lee



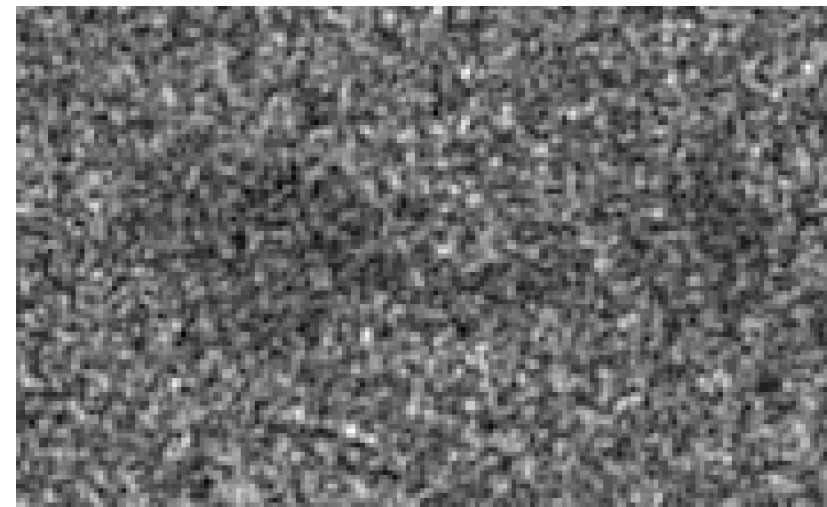
f) Refined Lee



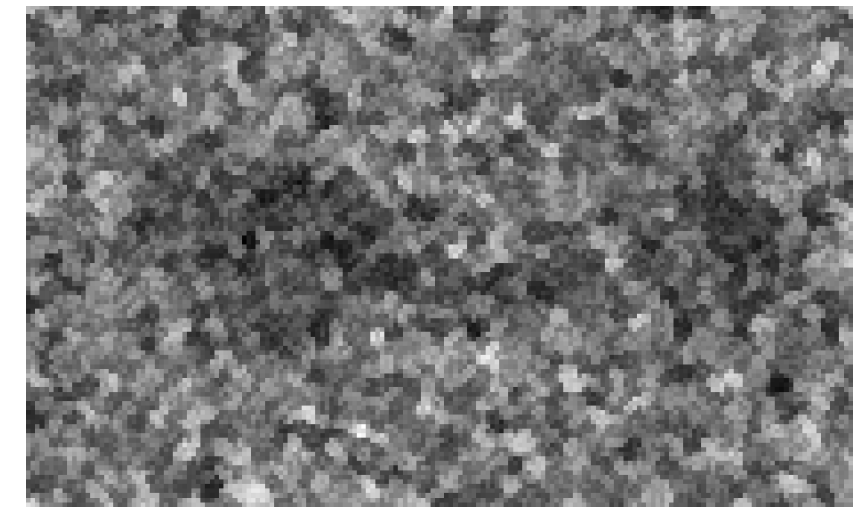
g) Frost



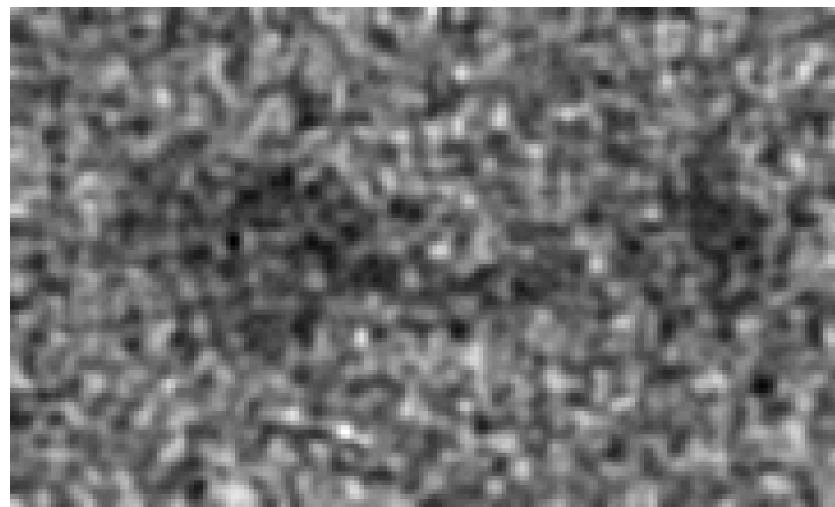
h) Enhanced Frost



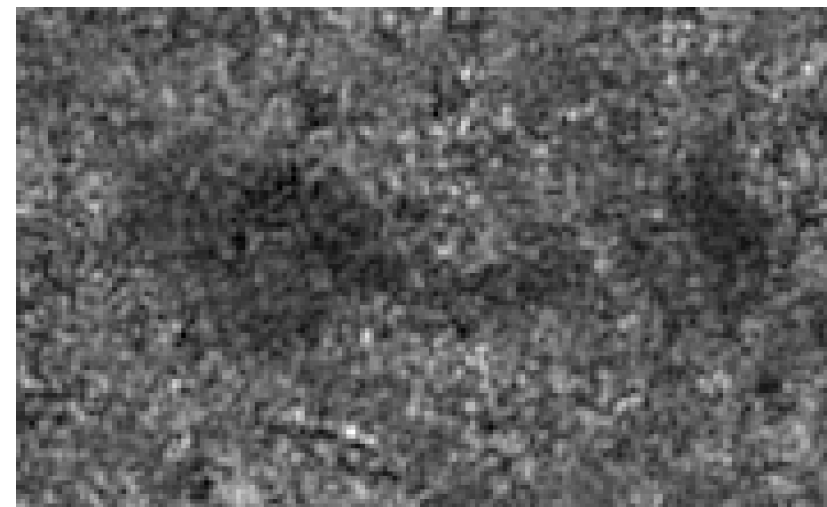
i) SNN



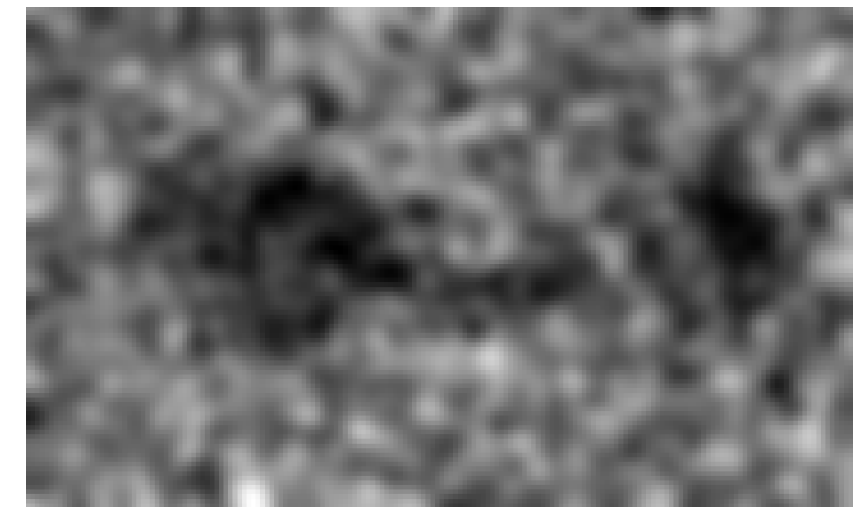
j) Bilateral



k) Guided filter



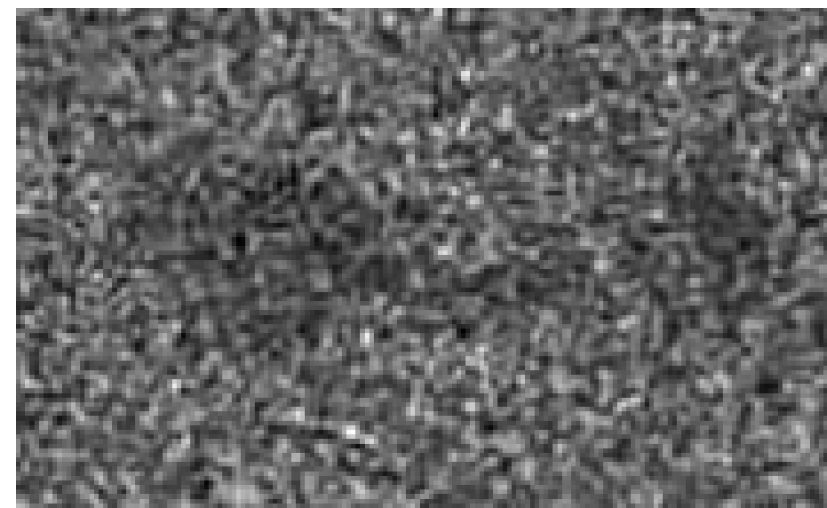
l) SRAD



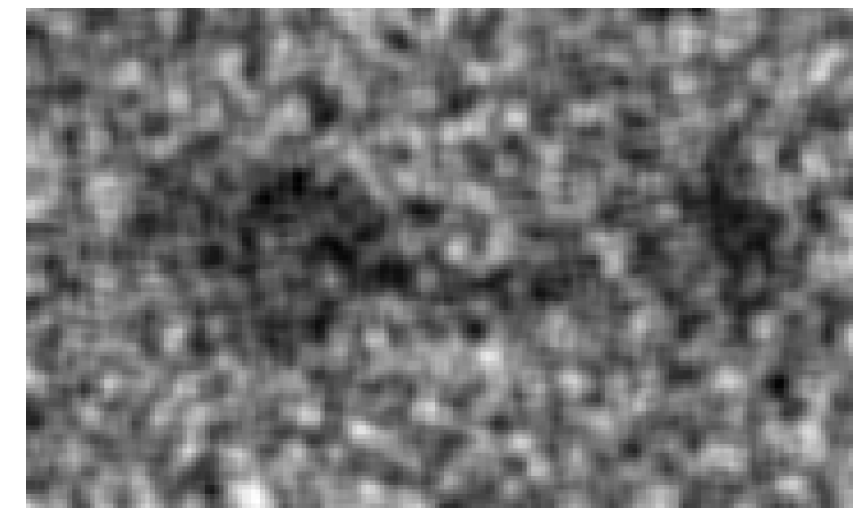
m) Improved DWT



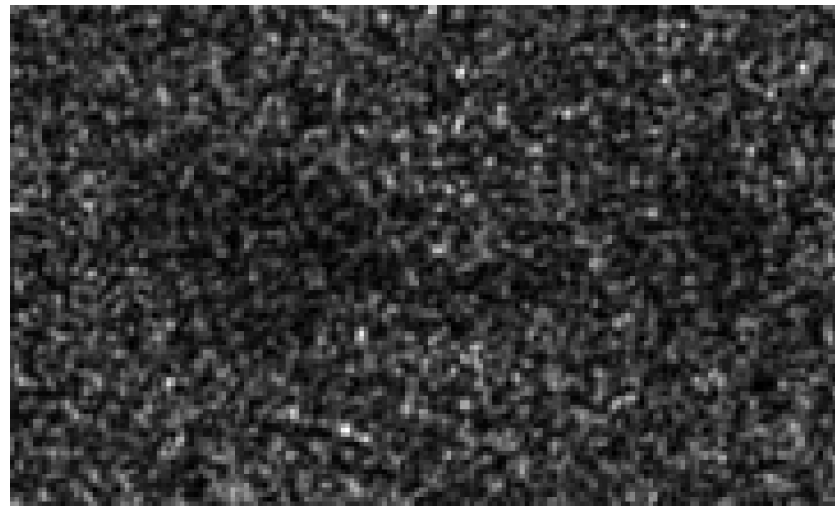
n) SAR BM3D



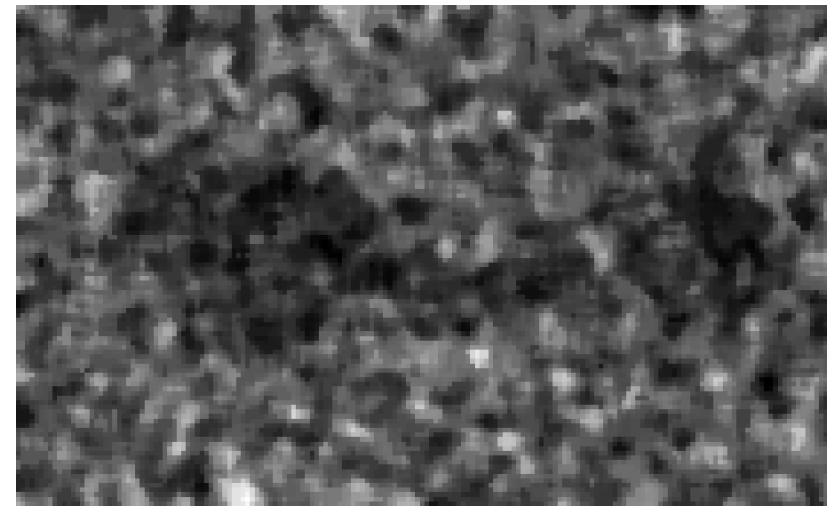
o) Gamma Map



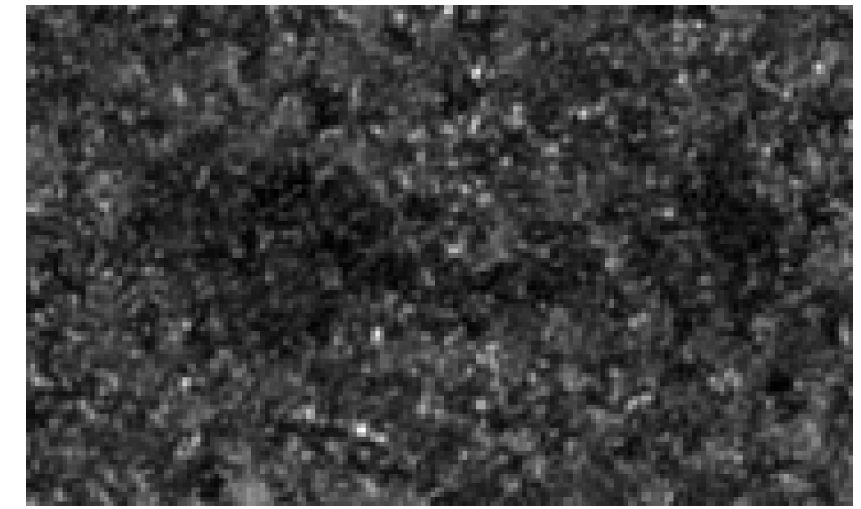
a) NRCS image



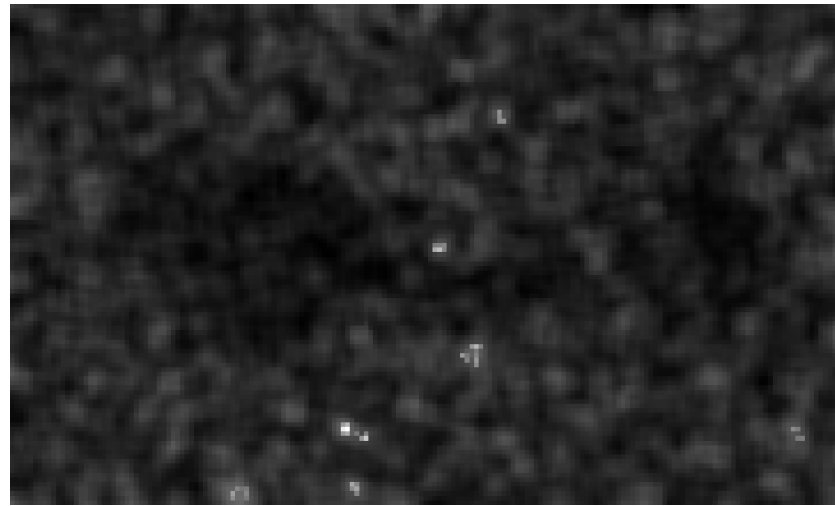
b) Median



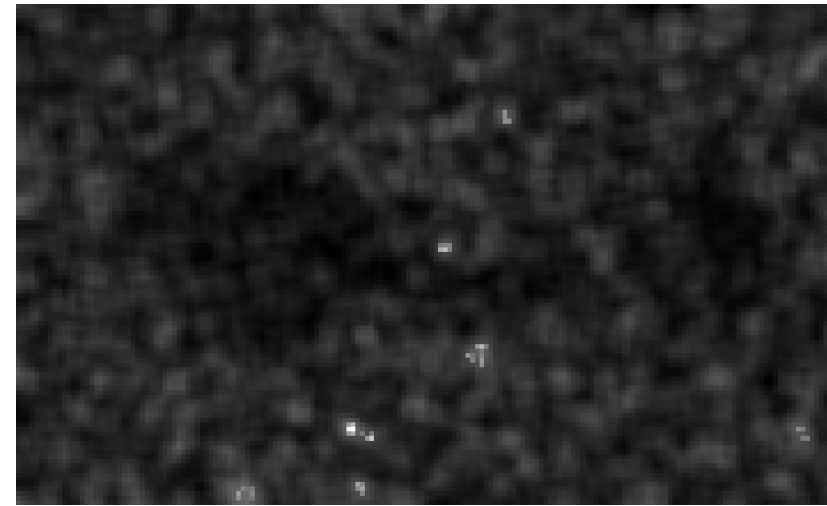
c) Lee



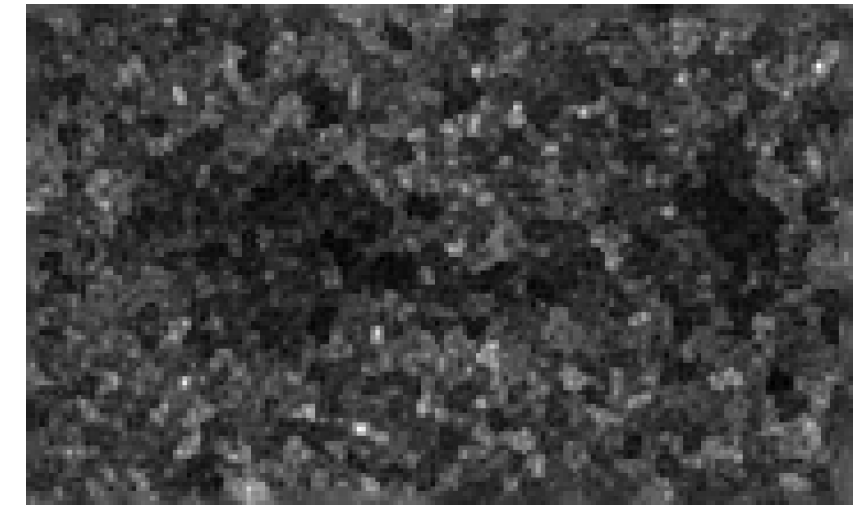
d) Lee Sigma



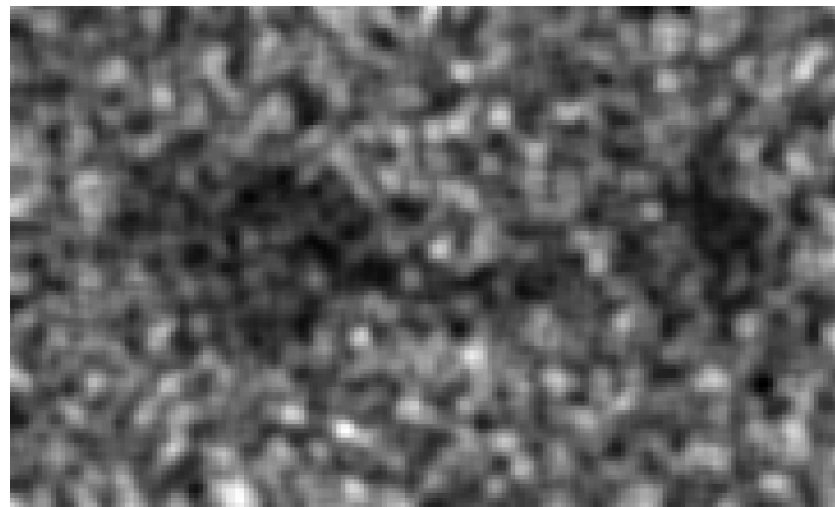
e) Enhanced Lee



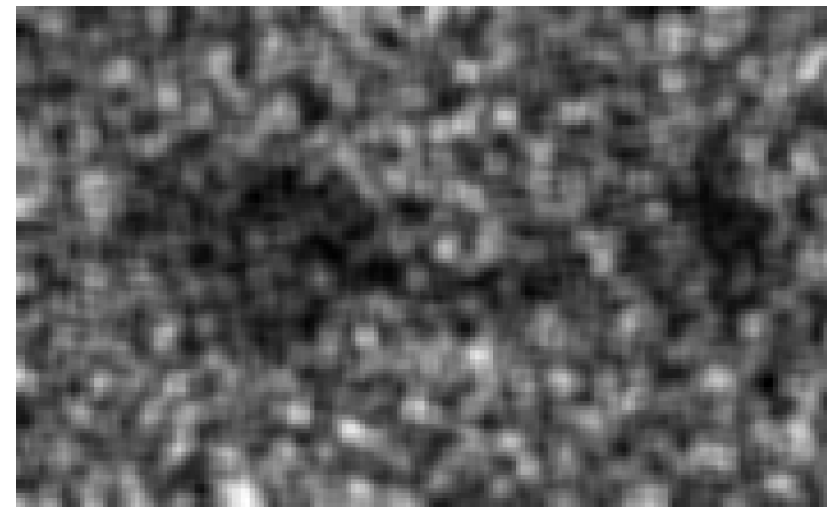
f) Refined Lee



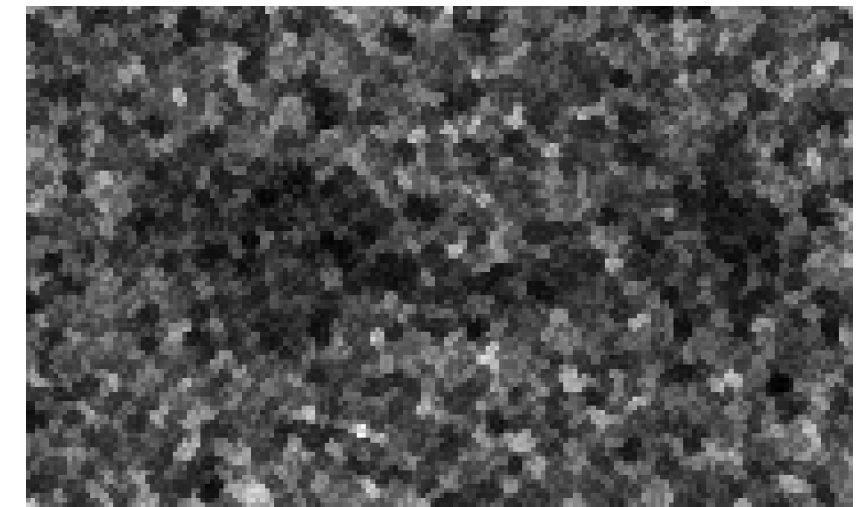
g) Frost



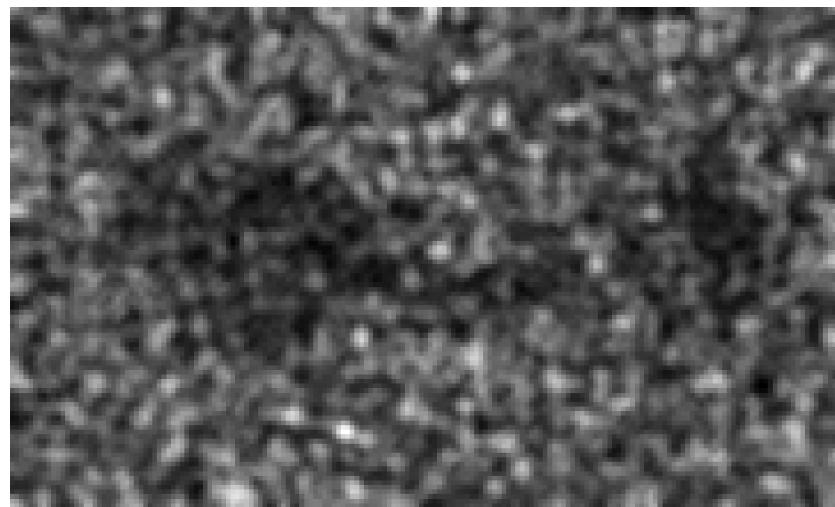
h) Enhanced Frost



i) SNN



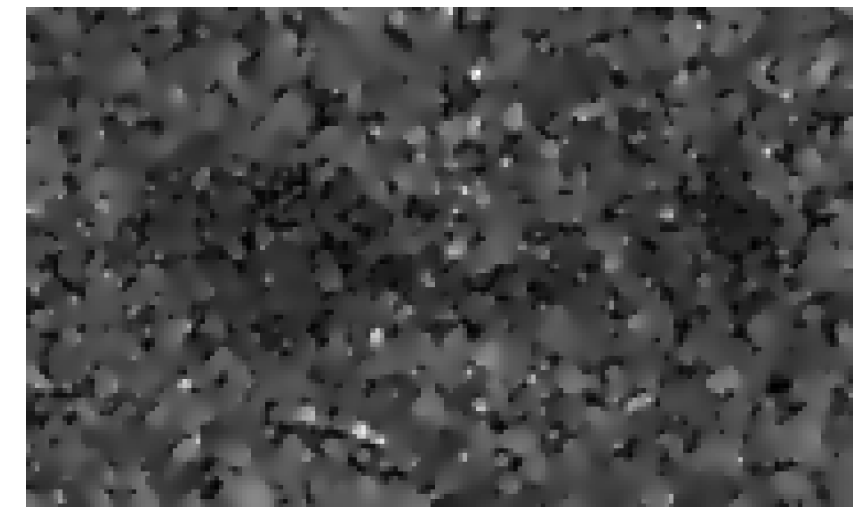
j) Bilateral



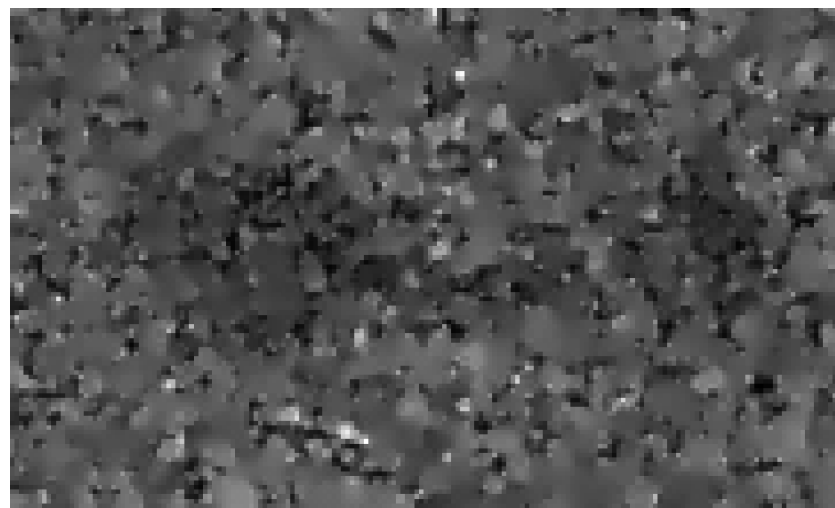
k) Guided filter



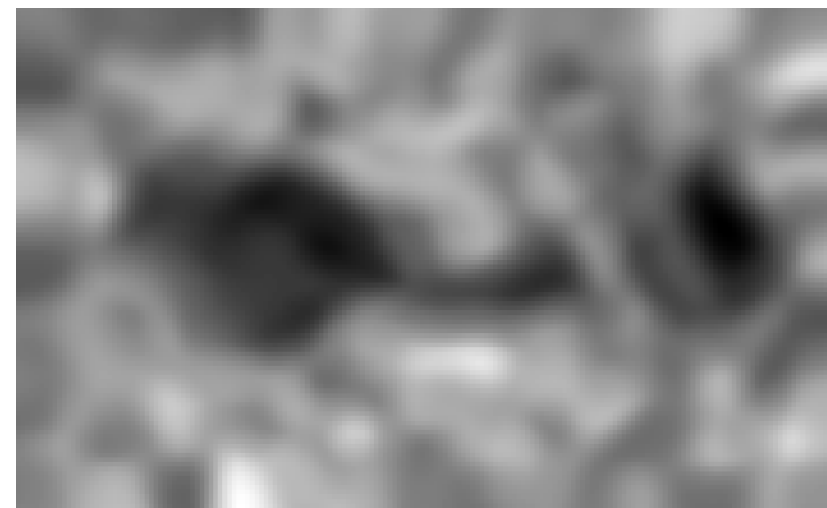
l) SRAD



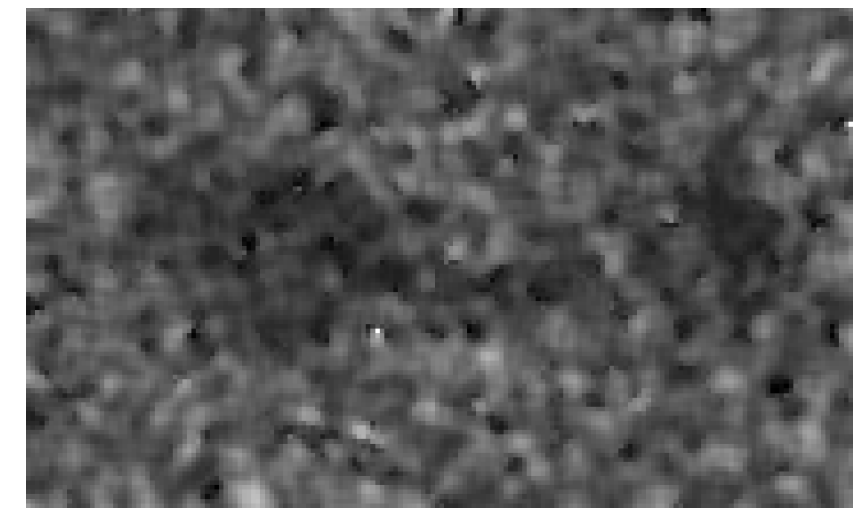
m) Improved DWT



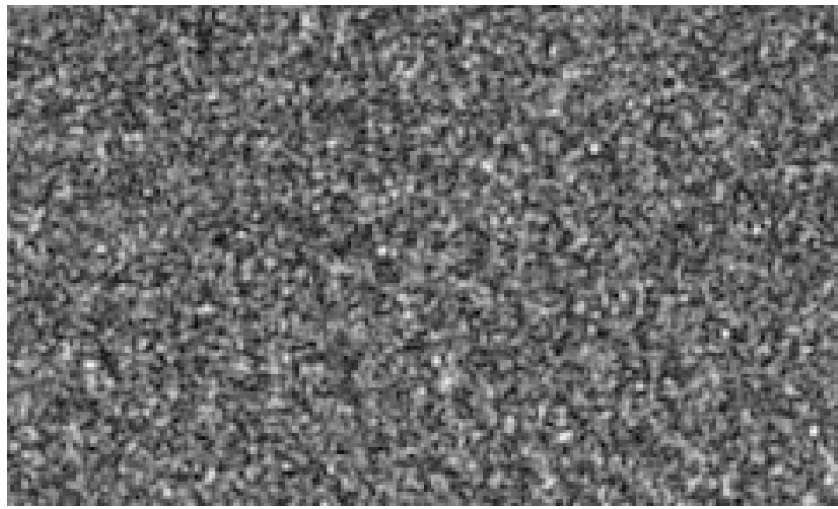
n) SAR BM3D



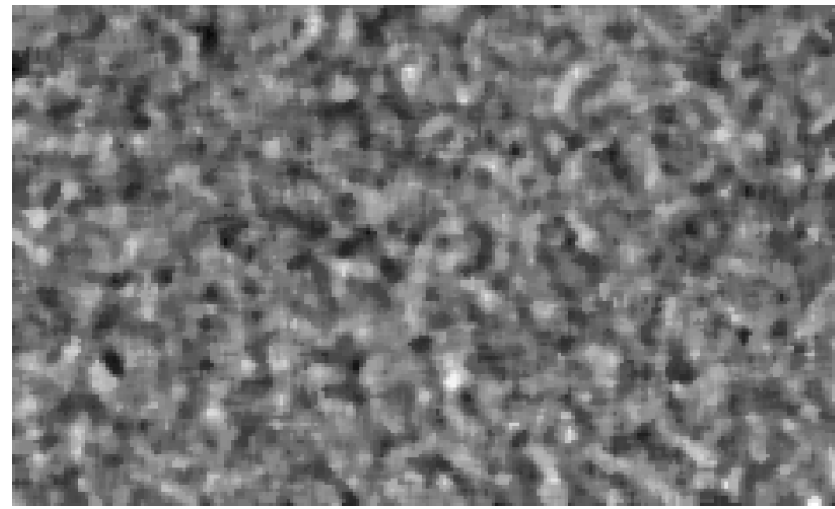
o) Gamma Map



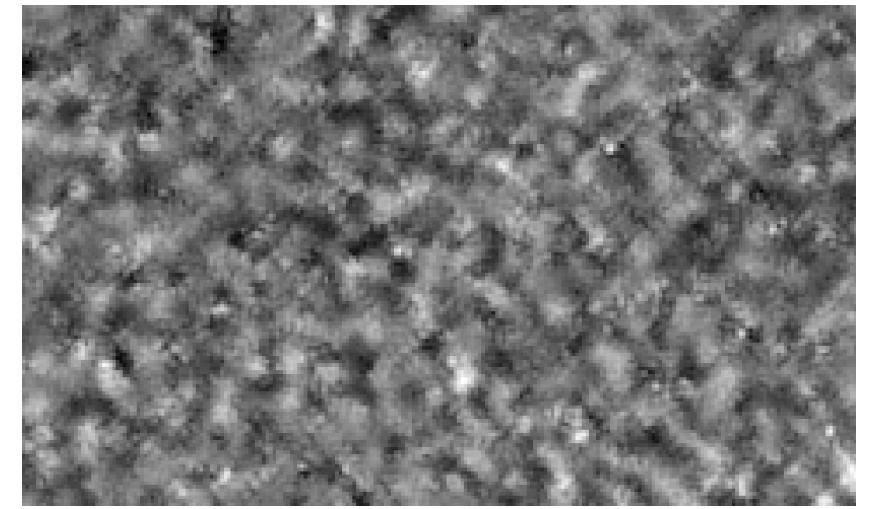
a) NRCS image



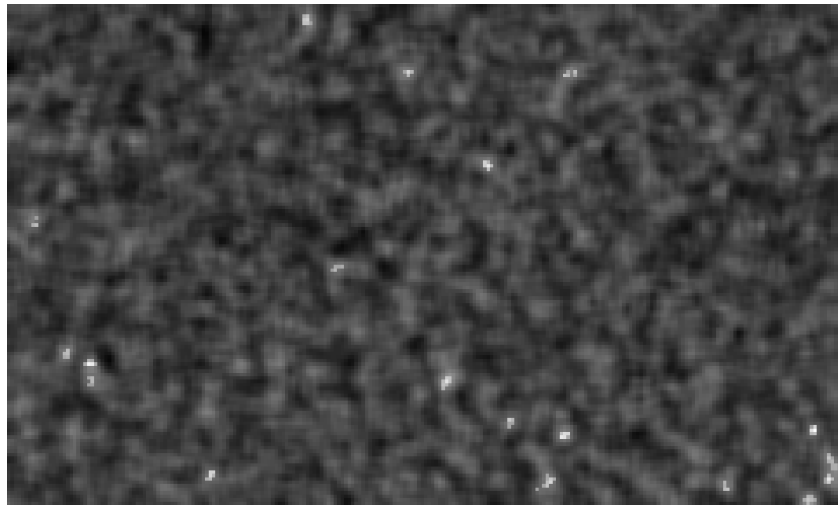
b) Median



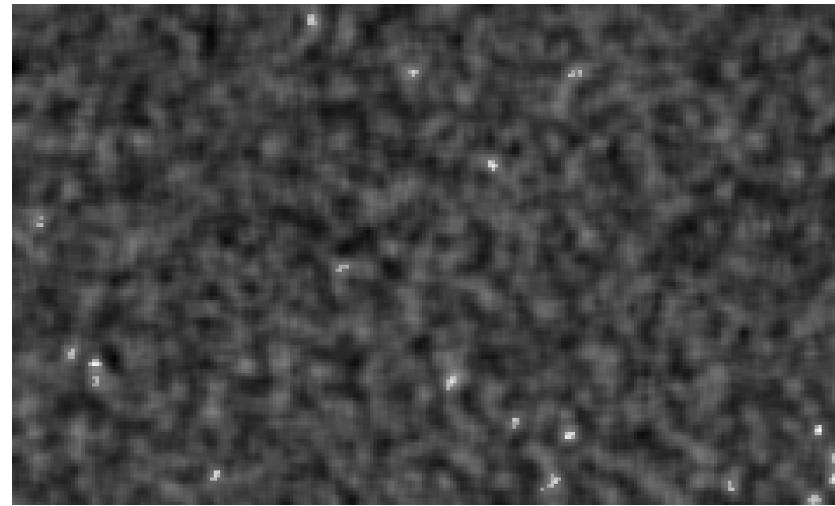
c) Lee



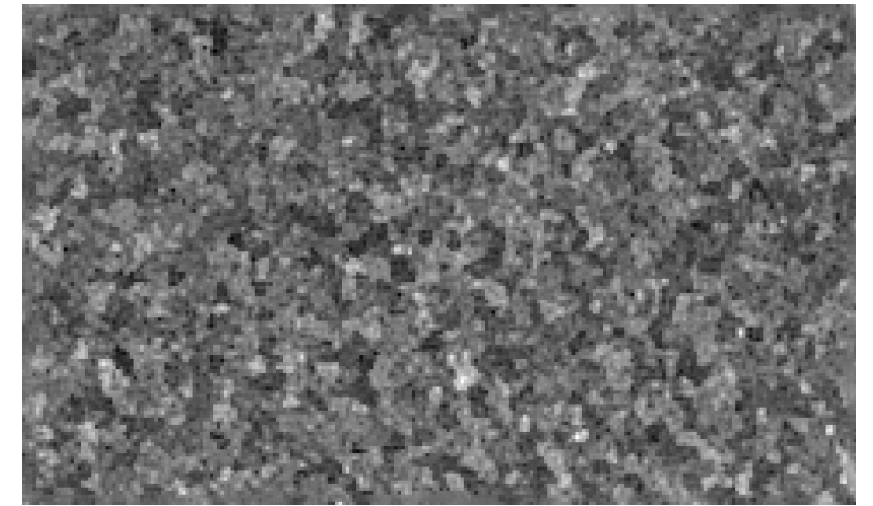
d) Lee Sigma



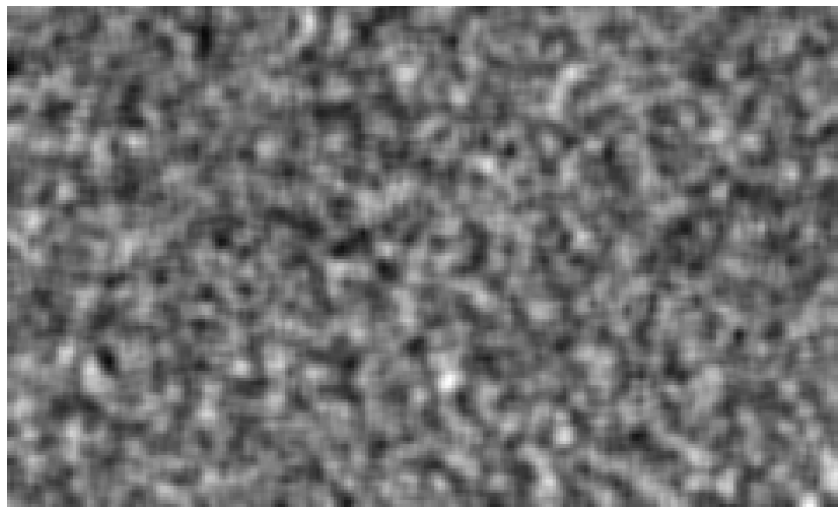
e) Enhanced Lee



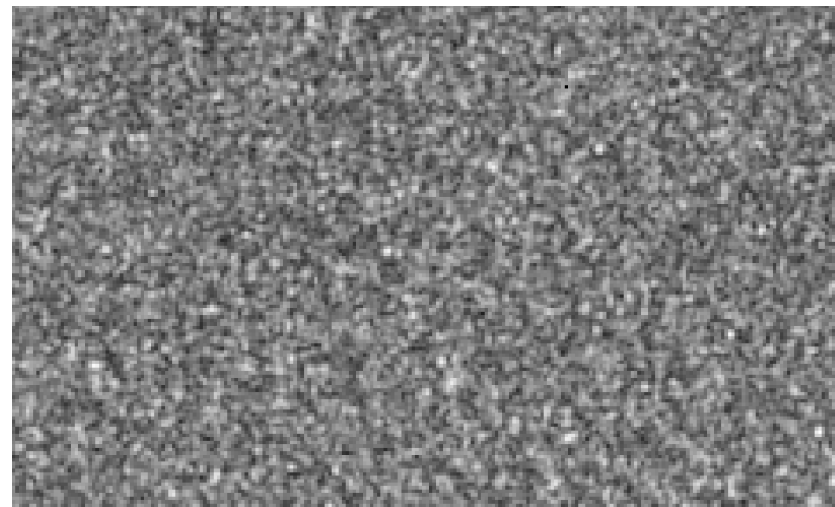
f) Refined Lee



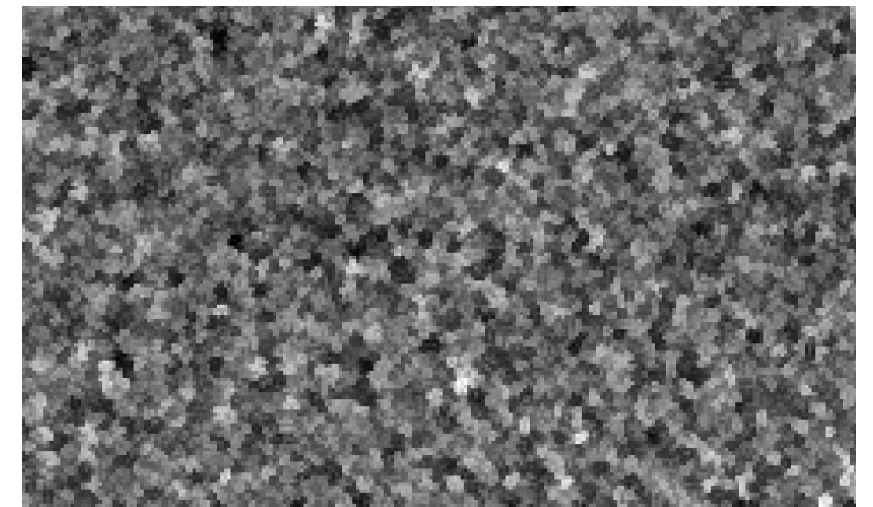
g) Frost



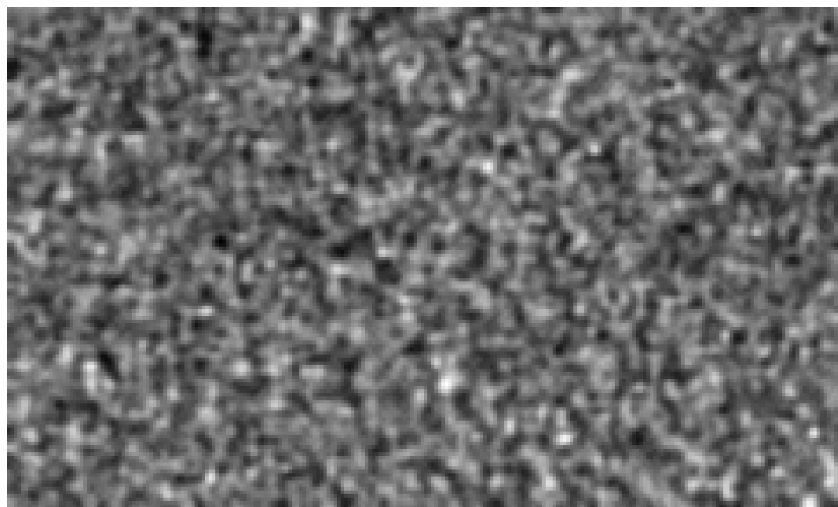
h) Enhanced Frost



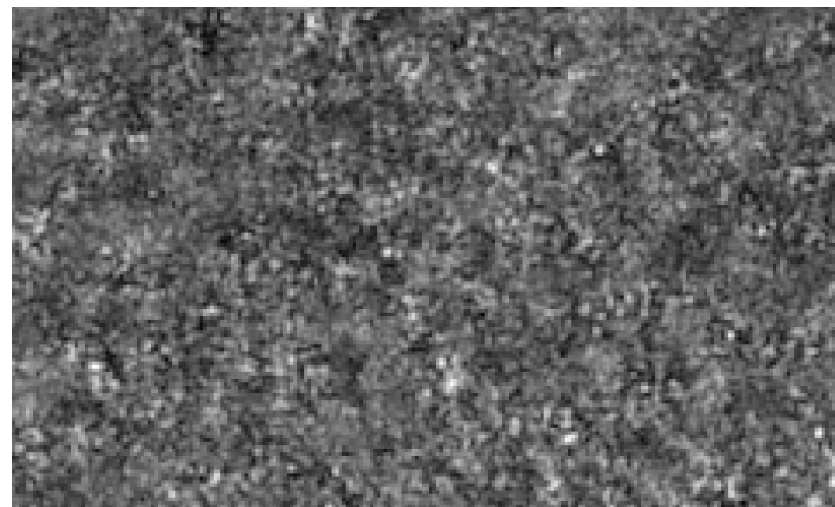
i) SNN



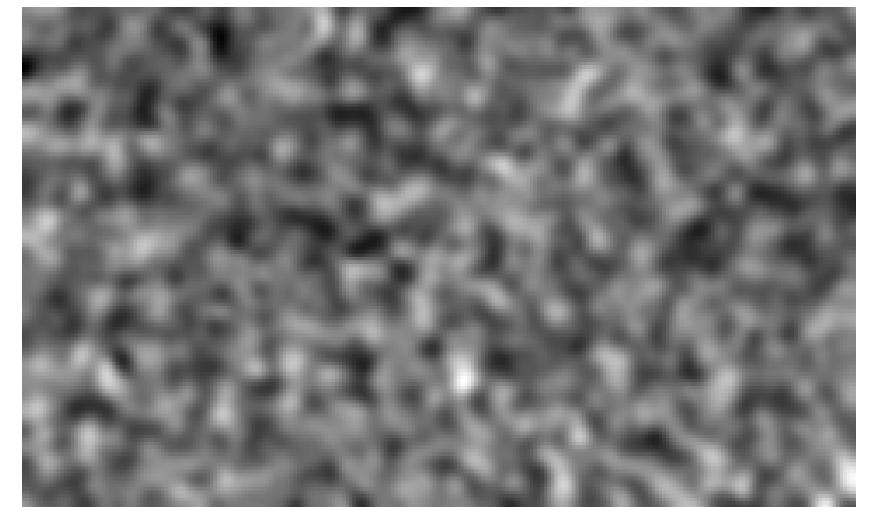
j) Bilateral



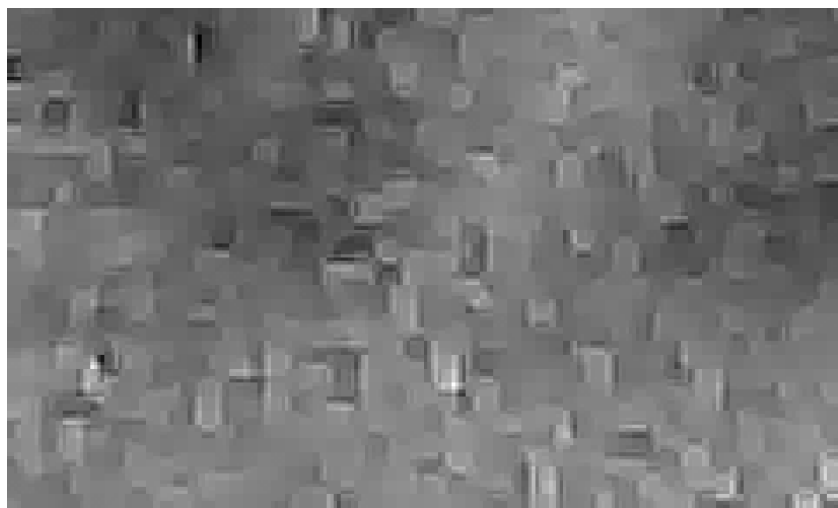
k) Guided filter



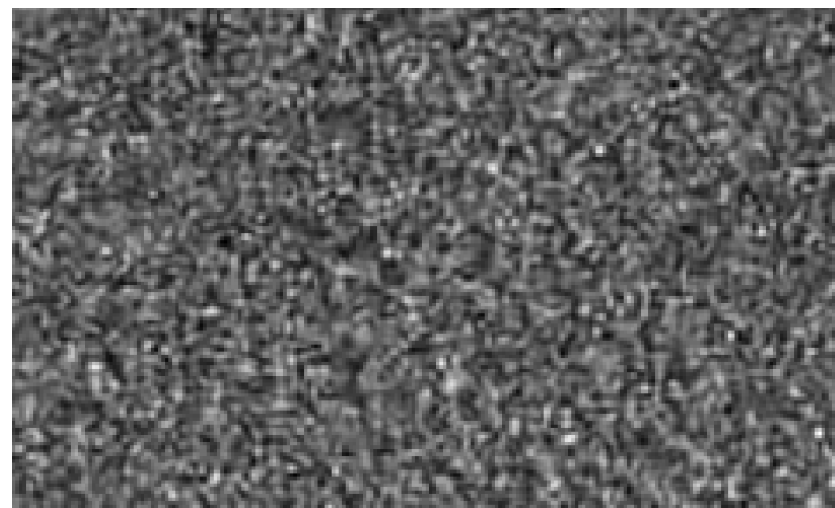
l) SRAD



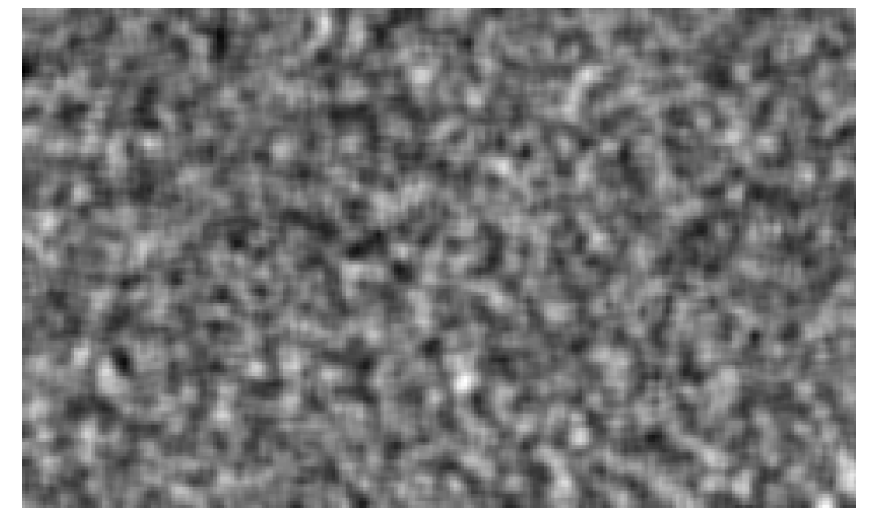
m) Improved DWT



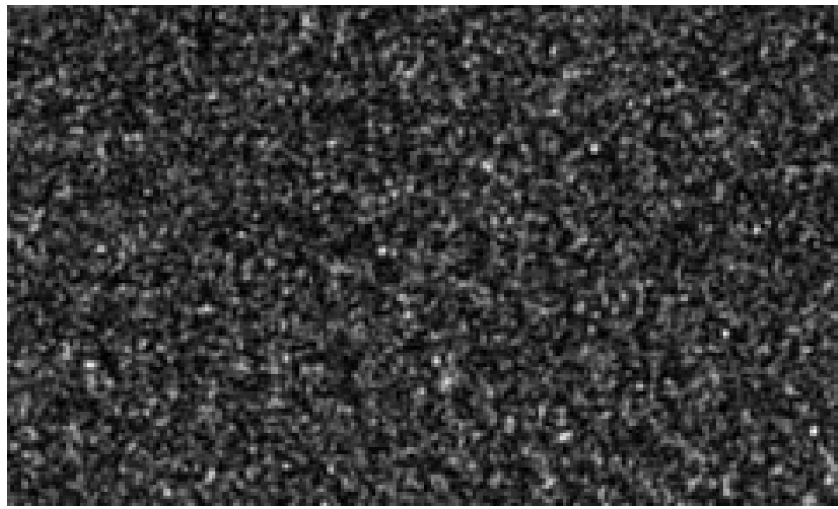
n) SAR BM3D



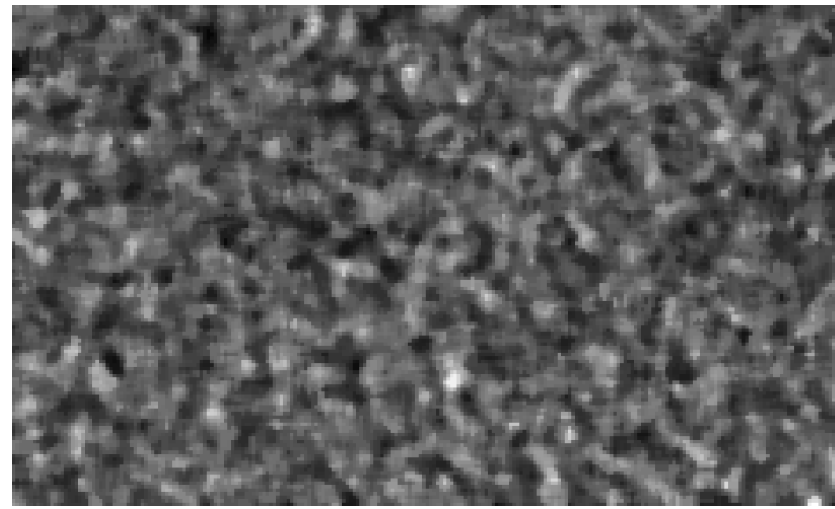
o) Gamma Map



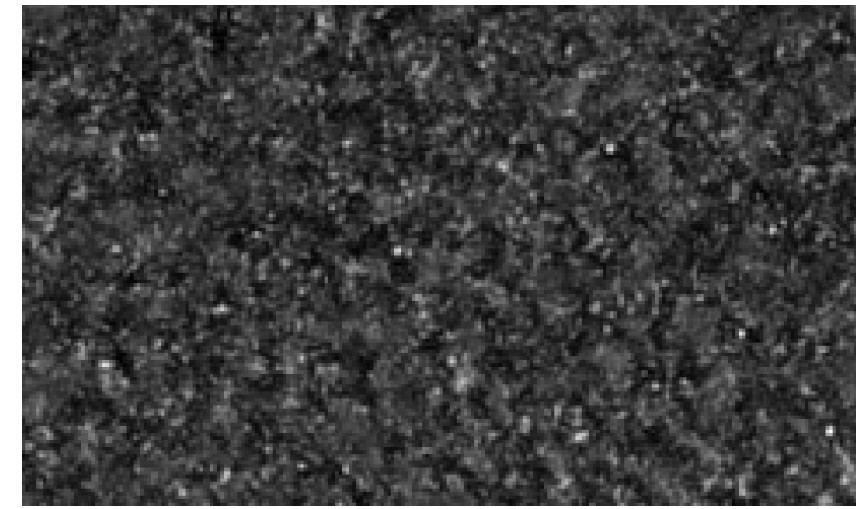
a) NRCS image



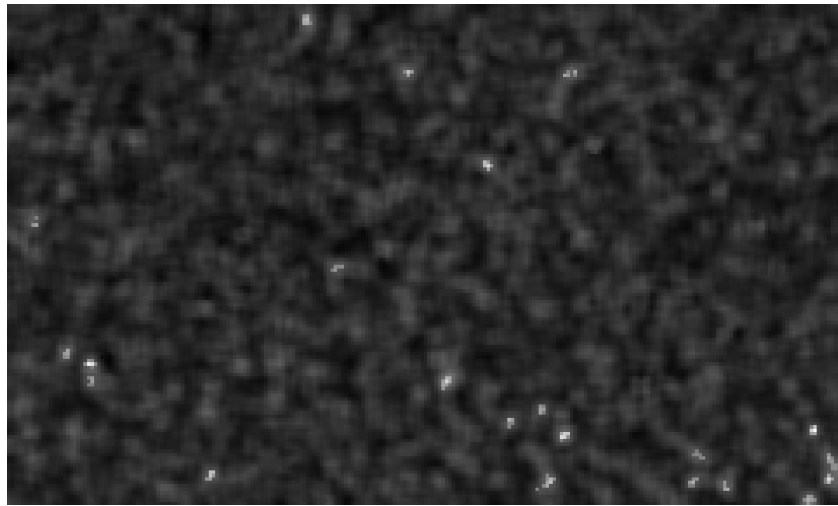
b) Median



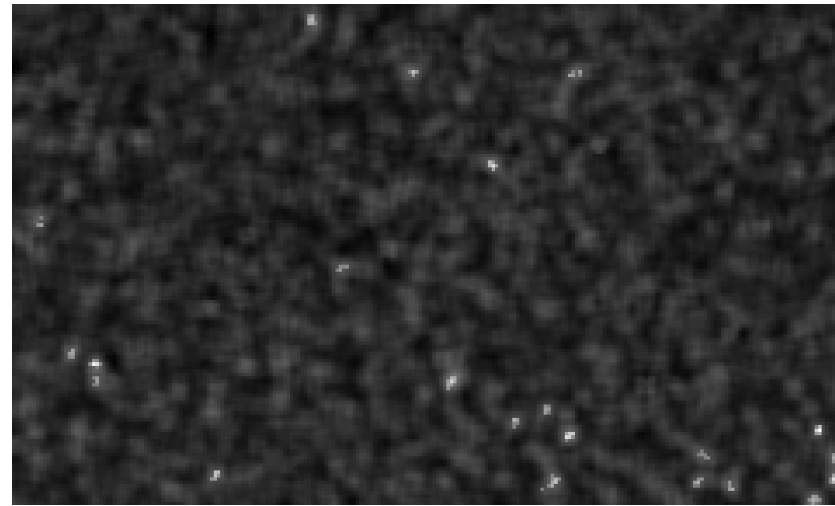
c) Lee



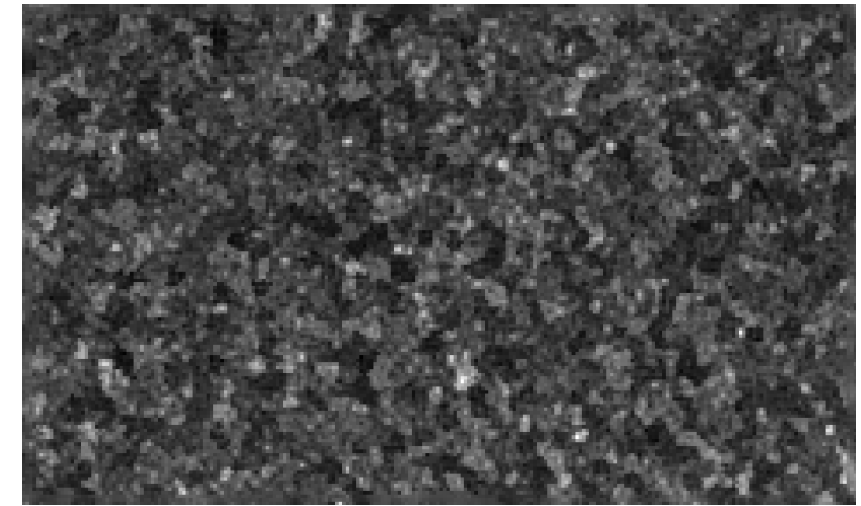
d) Lee Sigma



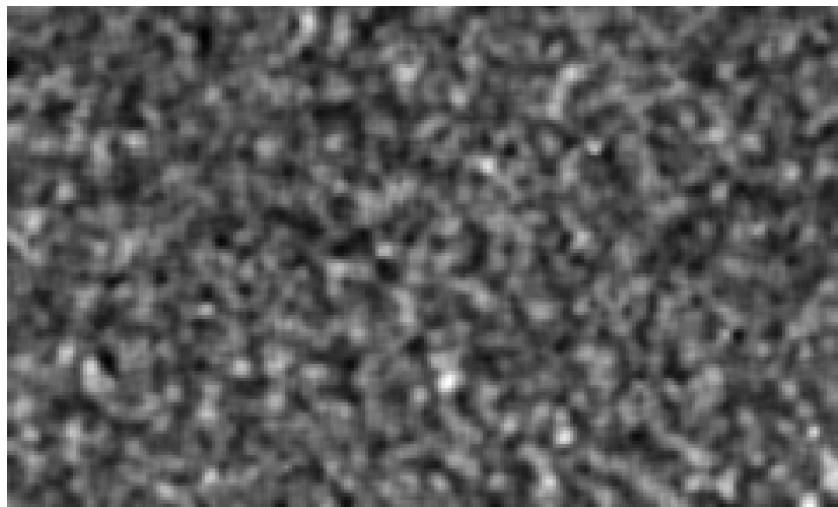
e) Enhanced Lee



f) Refined Lee



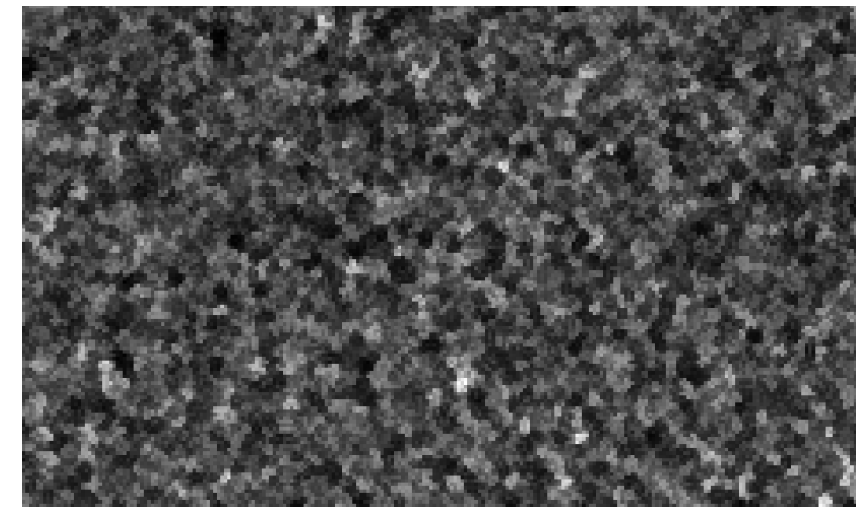
g) Frost



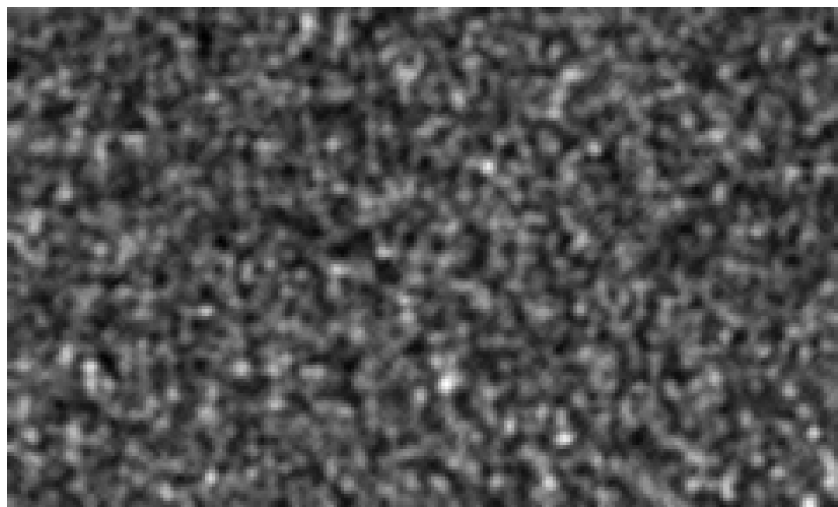
h) Enhanced Frost



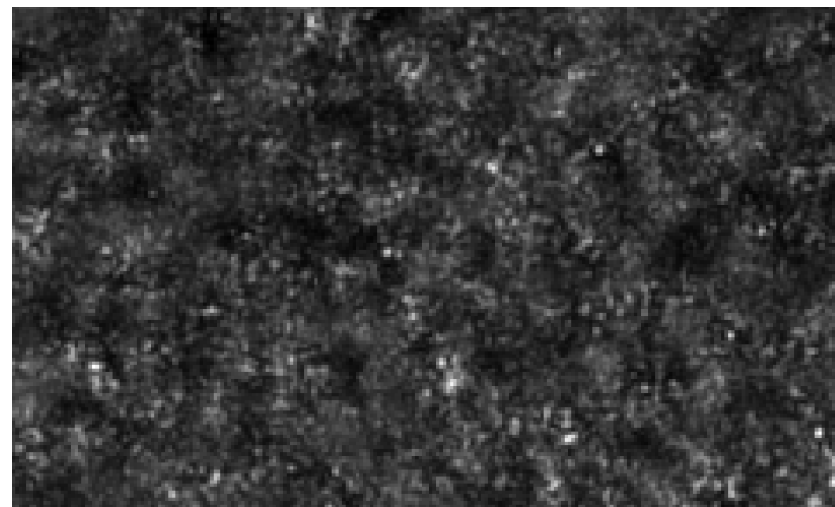
i) SNN



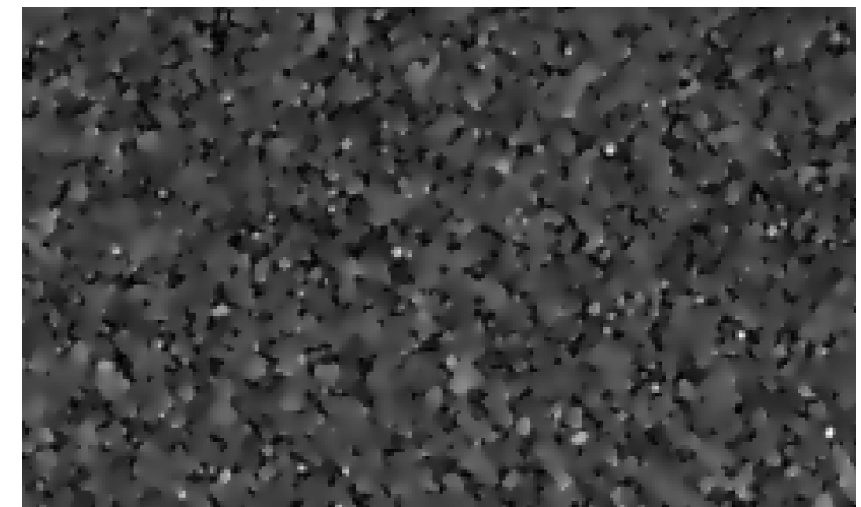
j) Bilateral



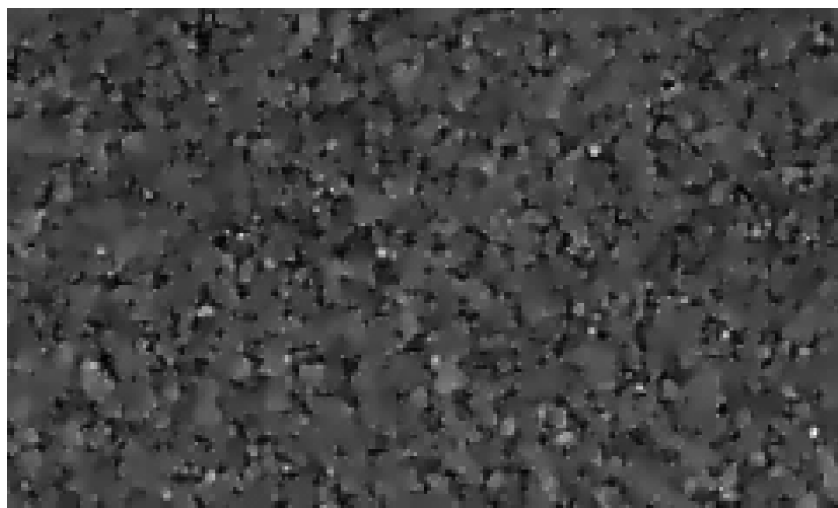
k) Guided filter



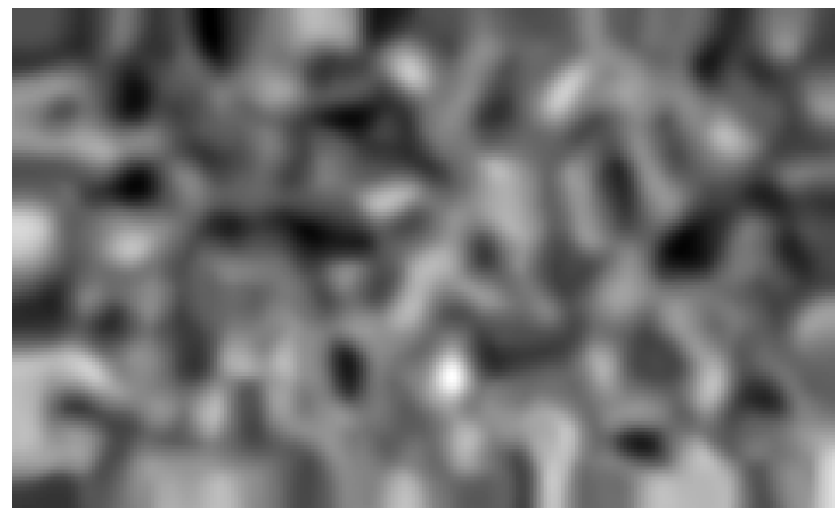
l) SRAD



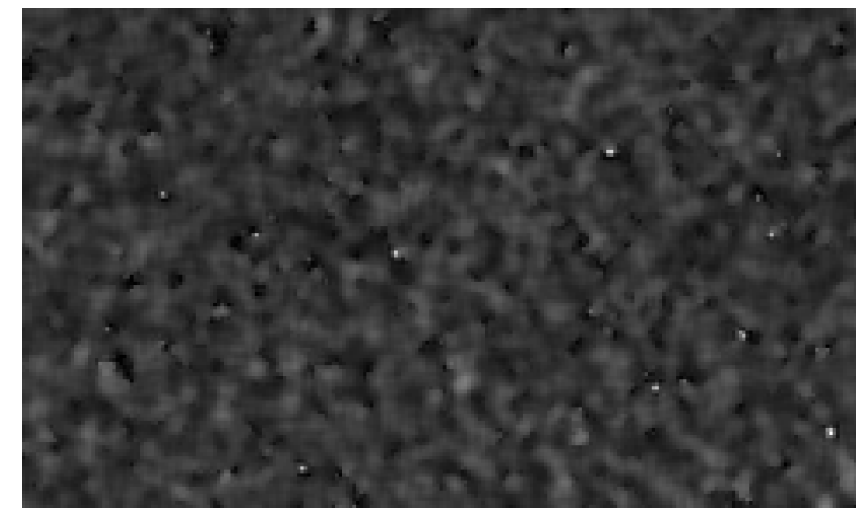
m) Improved DWT



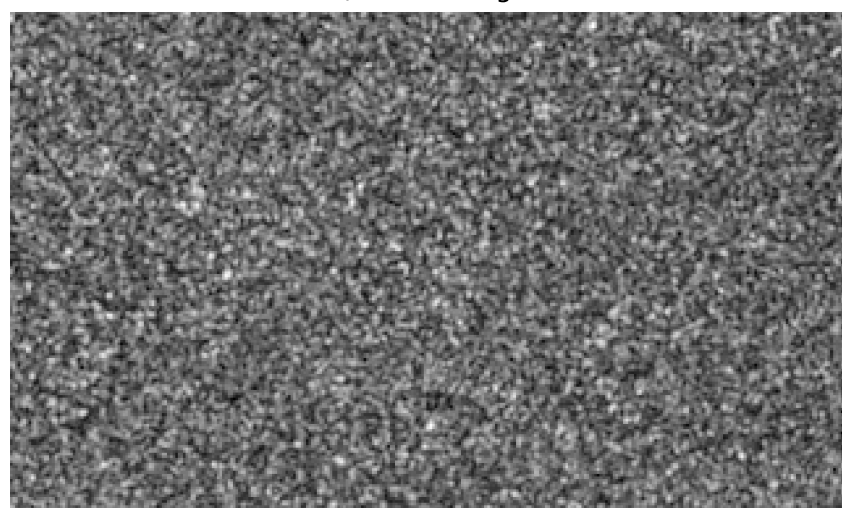
n) SAR BM3D



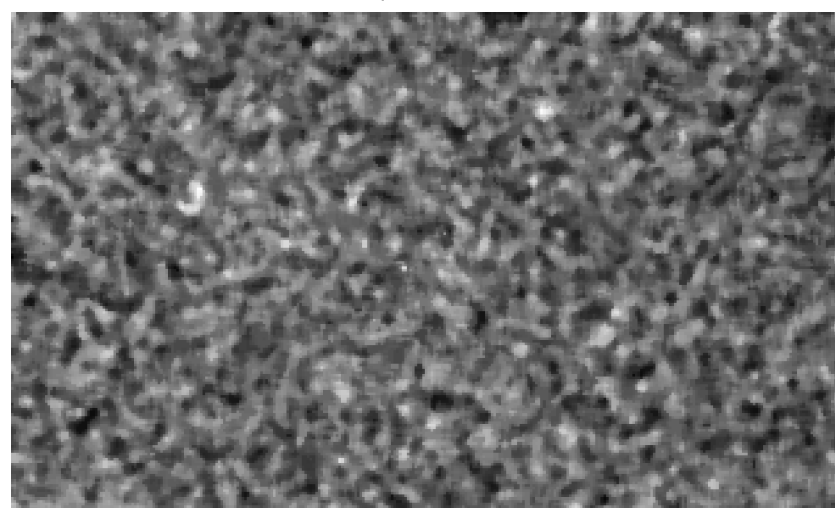
o) Gamma Map



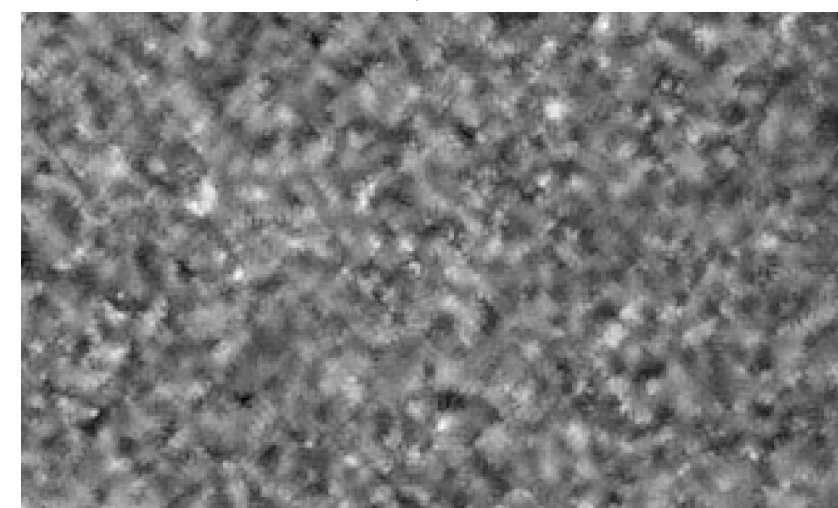
a) NRCS image



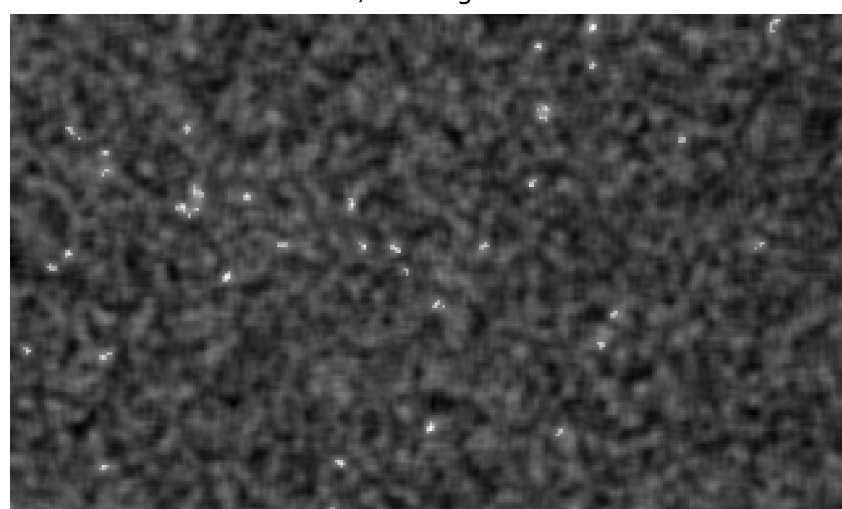
b) Median



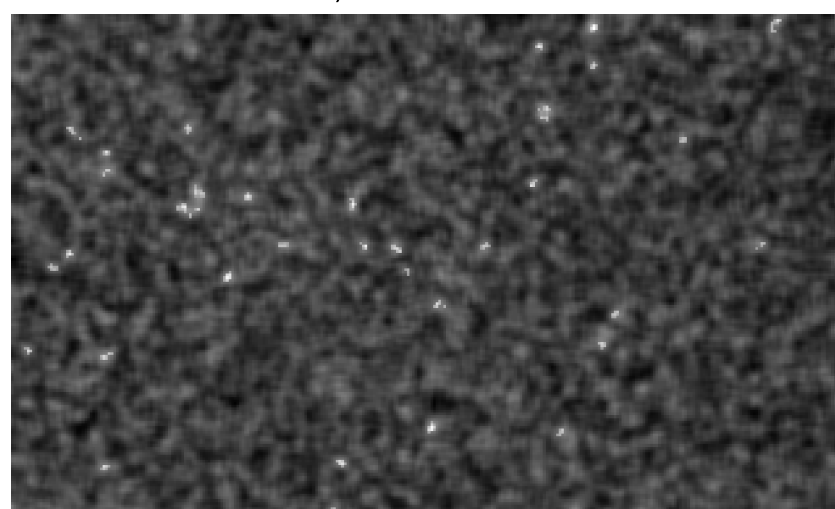
c) Lee



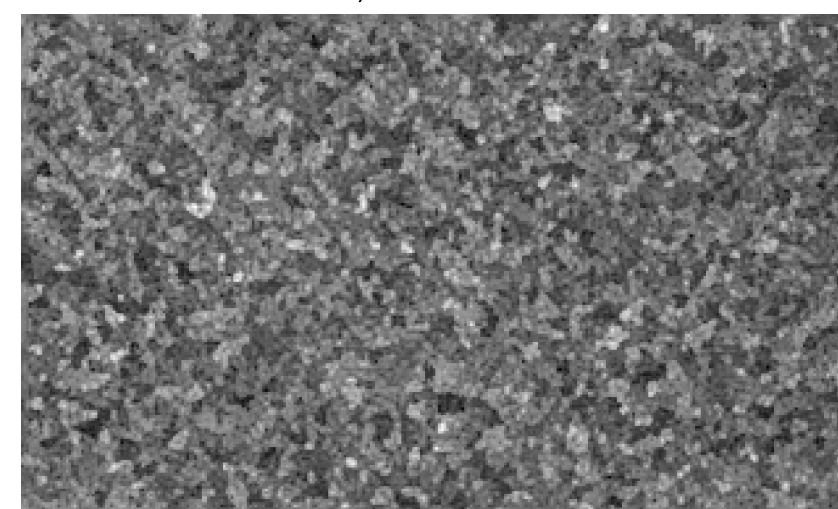
d) Lee Sigma



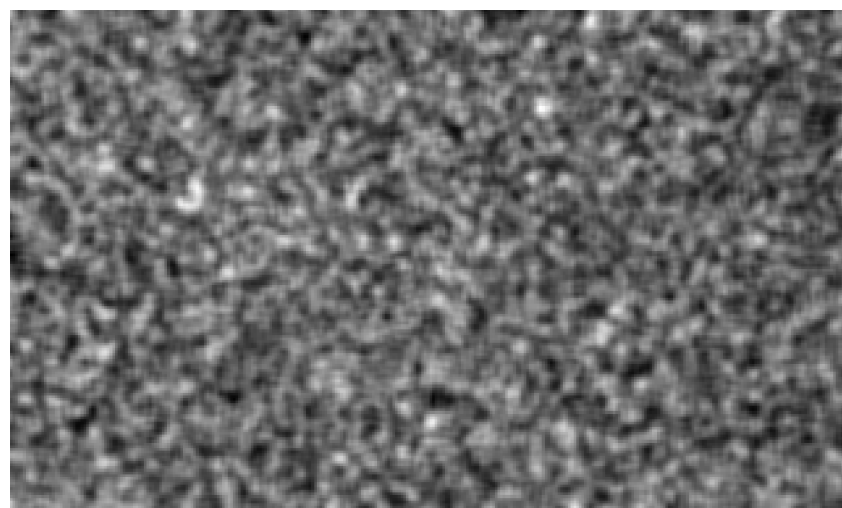
e) Enhanced Lee



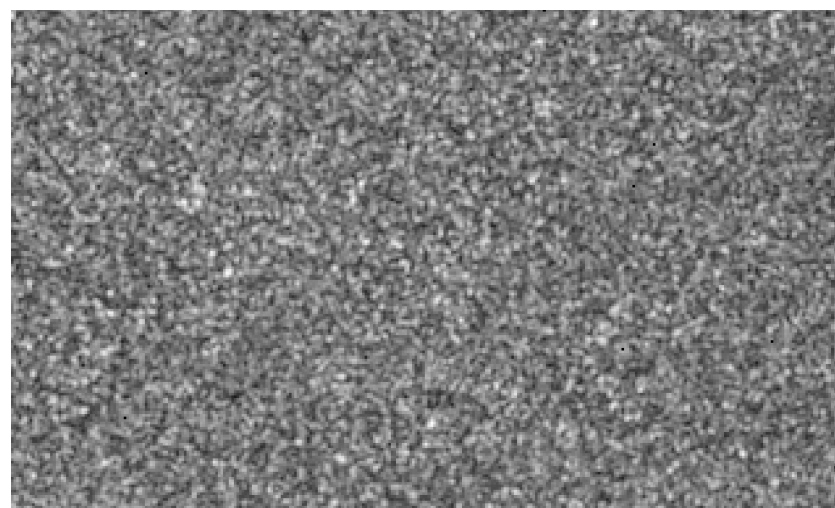
f) Refined Lee



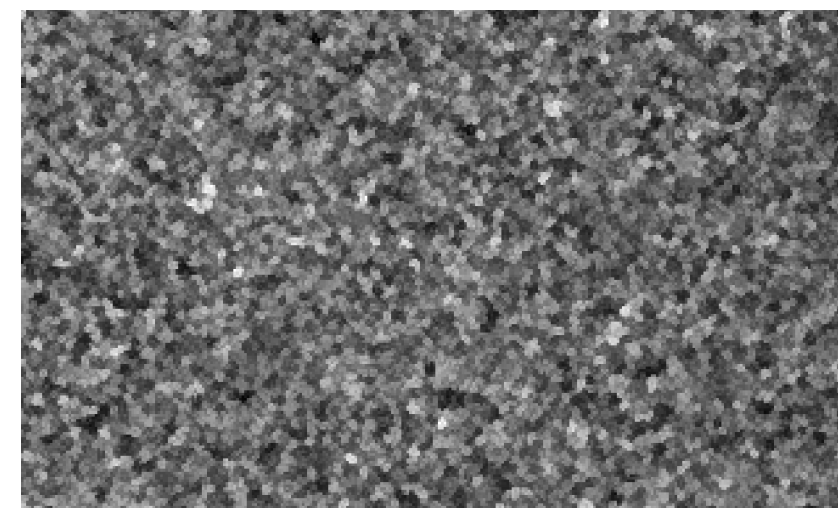
g) Frost



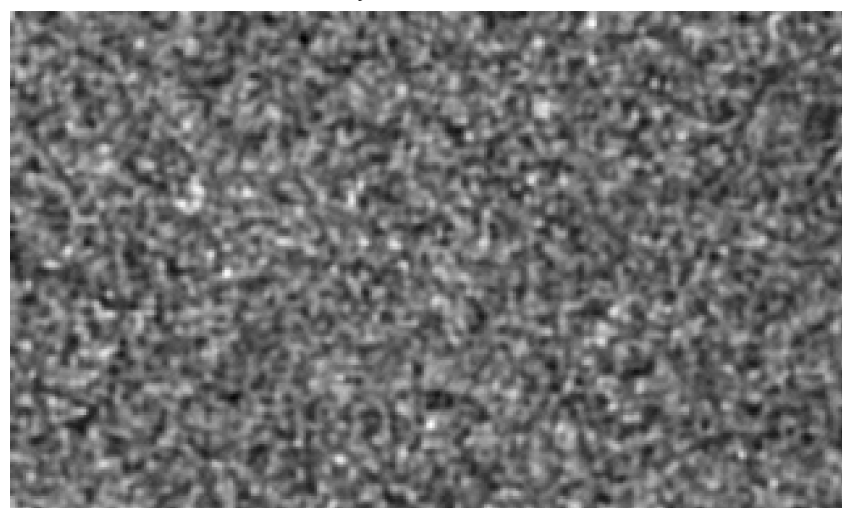
h) Enhanced Frost



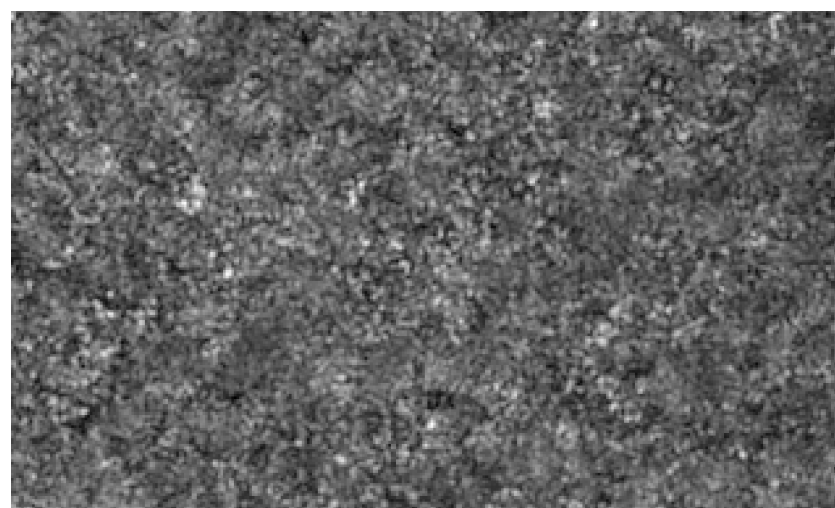
i) SNN



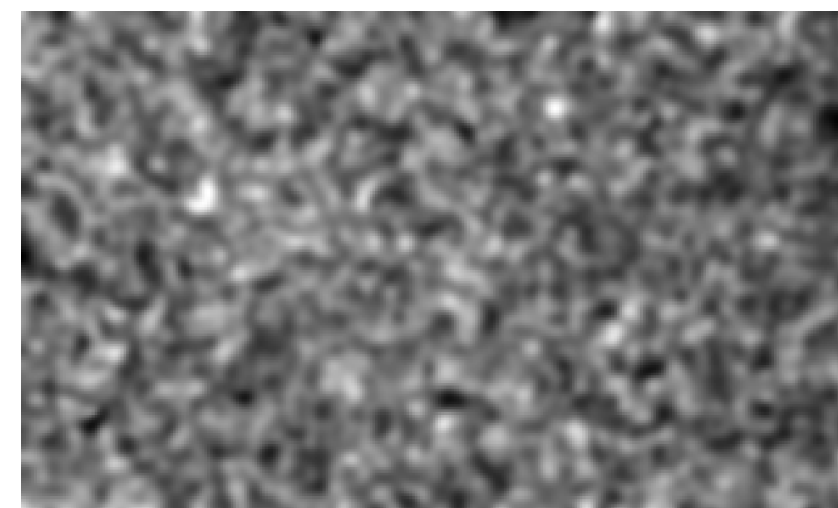
j) Bilateral



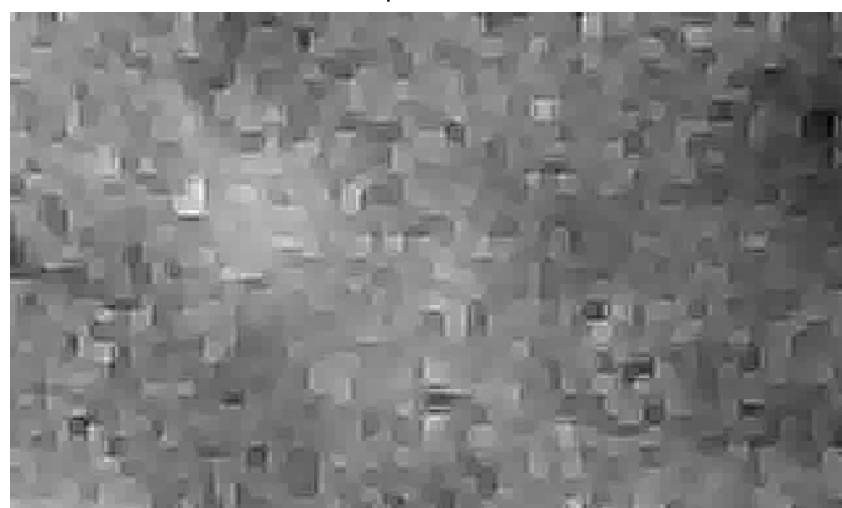
k) Guided filter



l) SRAD



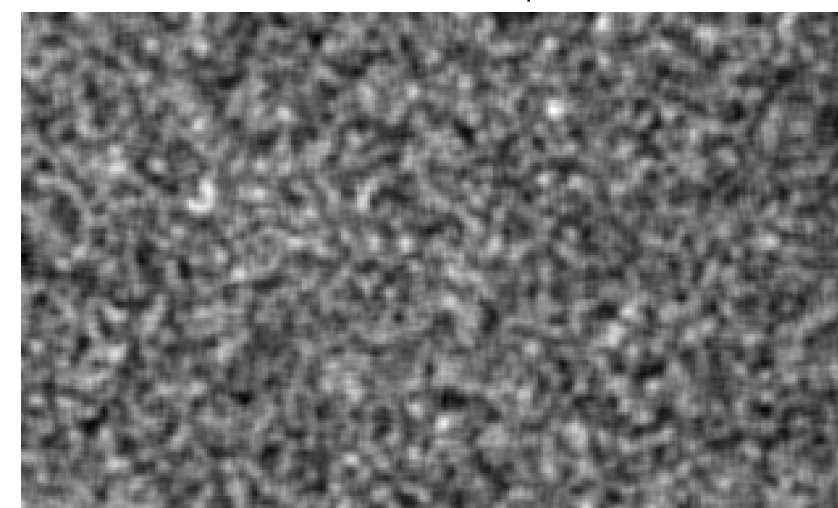
m) Improved DWT



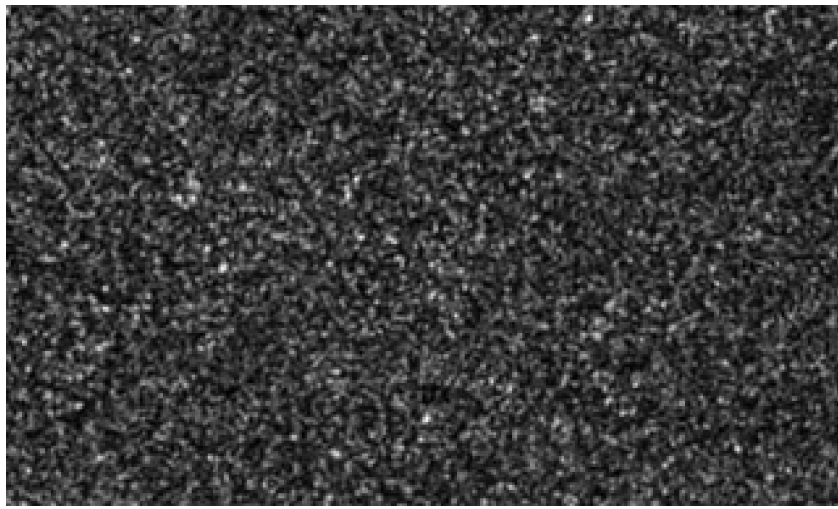
n) SAR BM3D



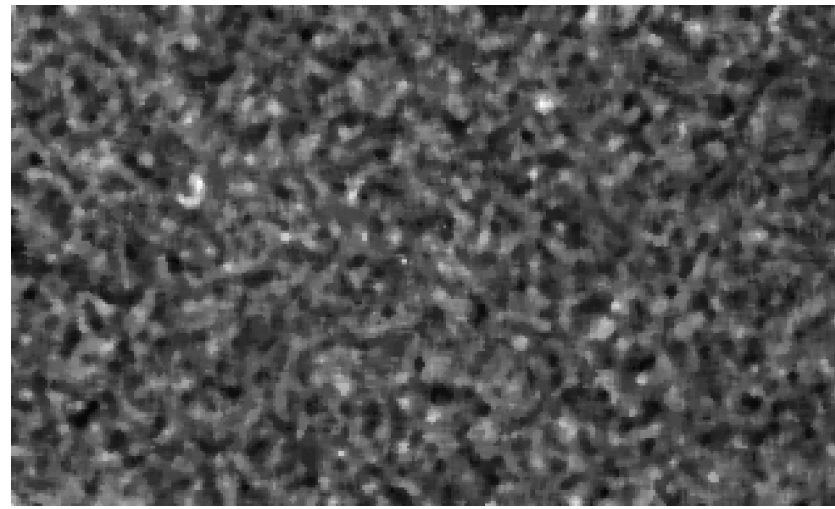
o) Gamma Map



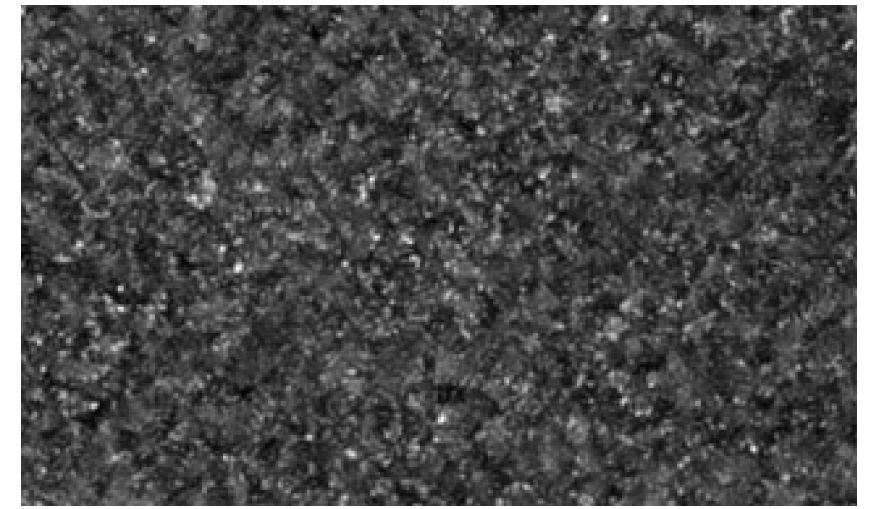
a) NRCS image



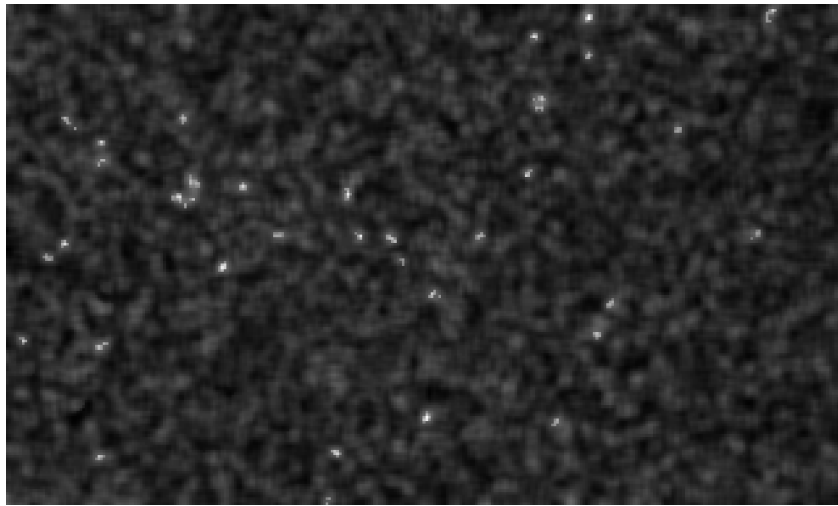
b) Median



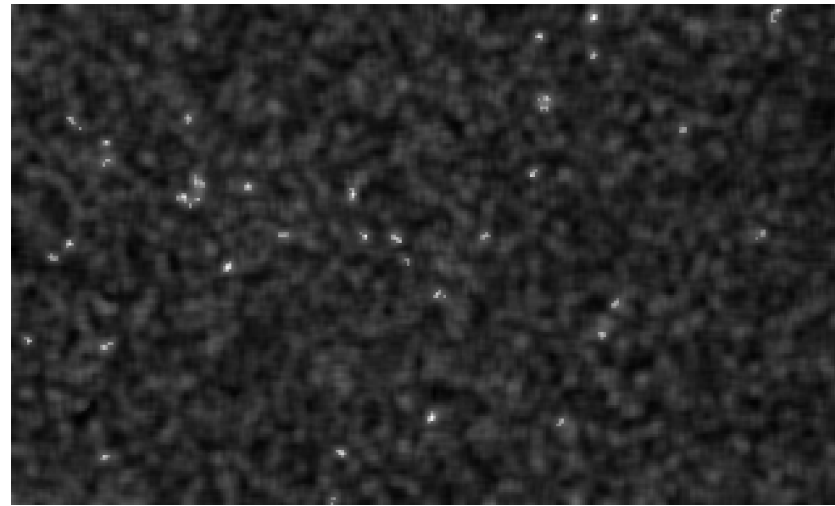
c) Lee



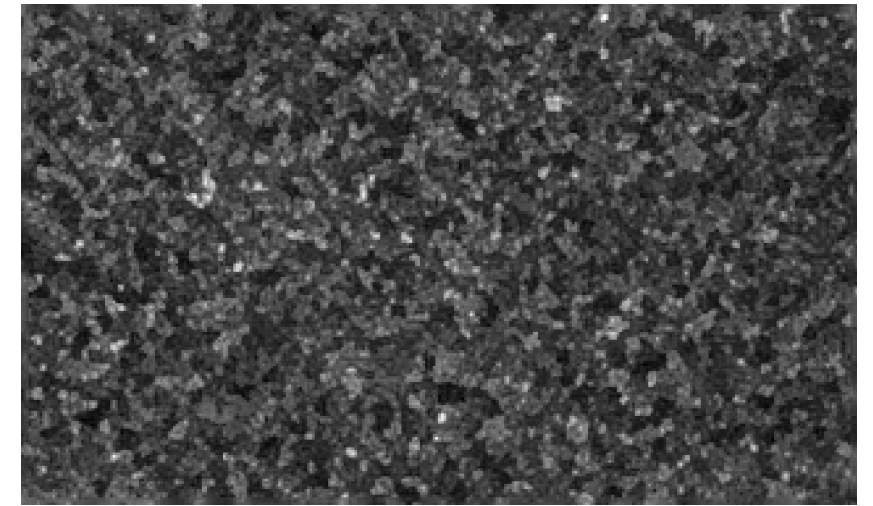
d) Lee Sigma



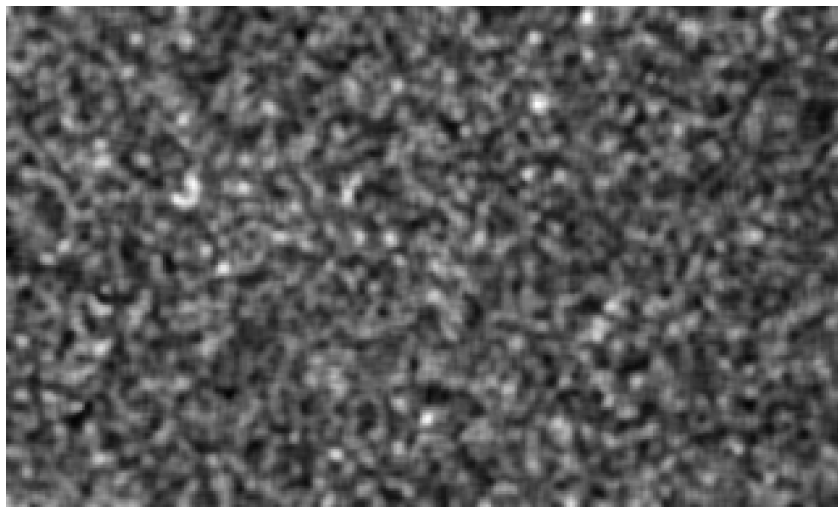
e) Enhanced Lee



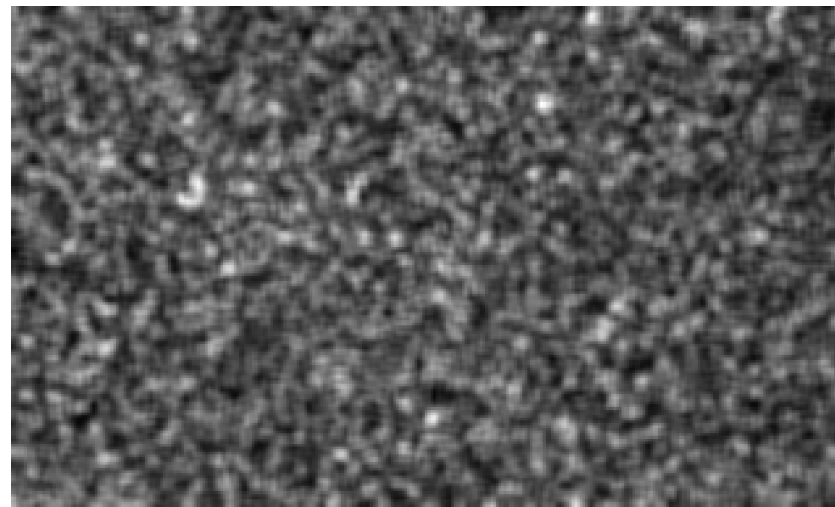
f) Refined Lee



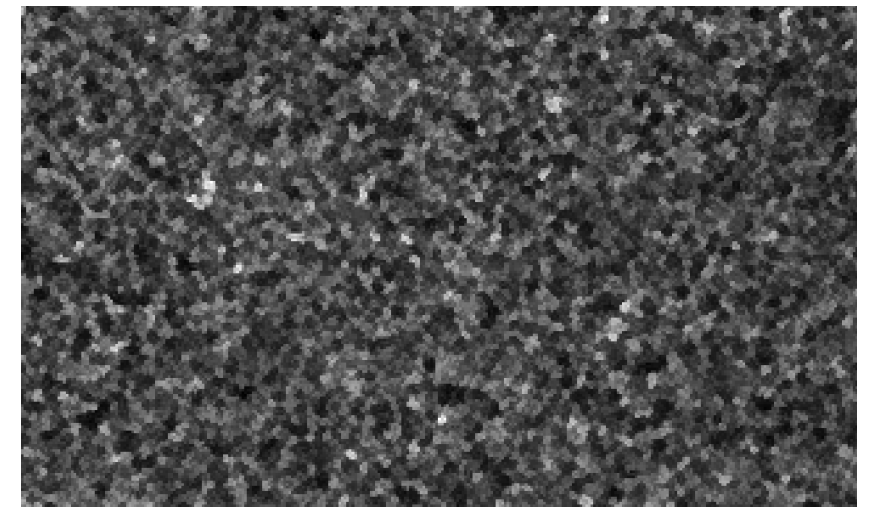
g) Frost



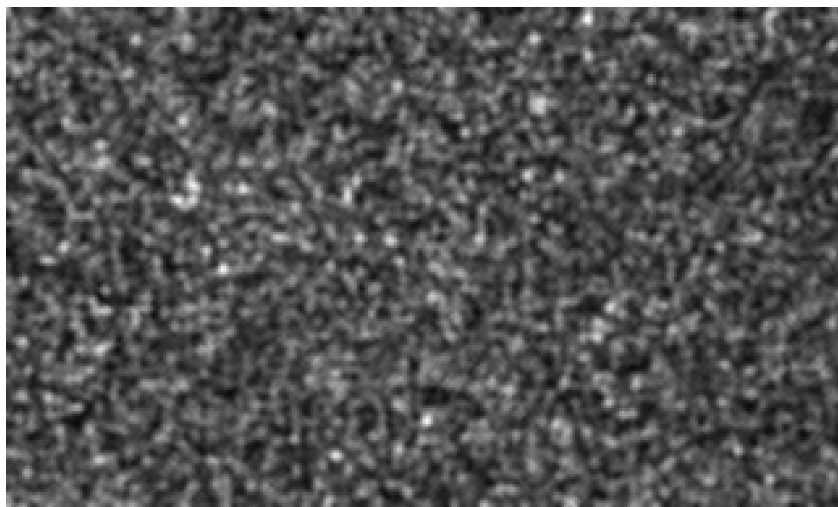
h) Enhanced Frost



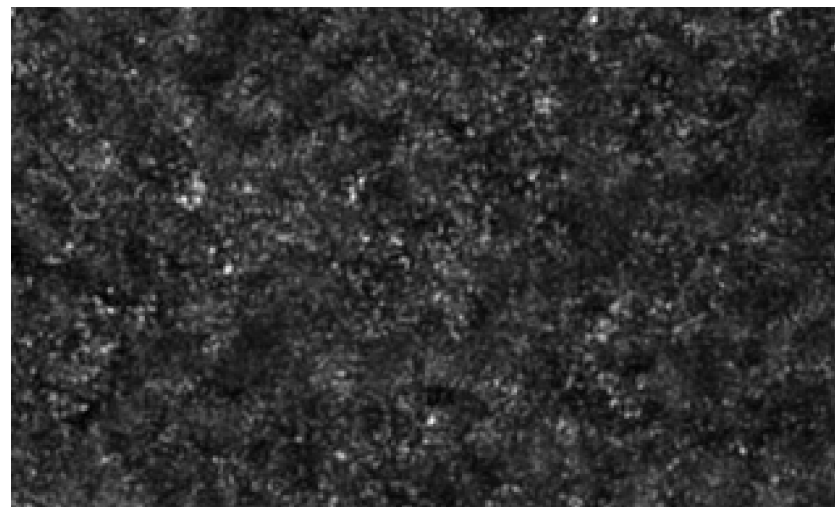
i) SNN



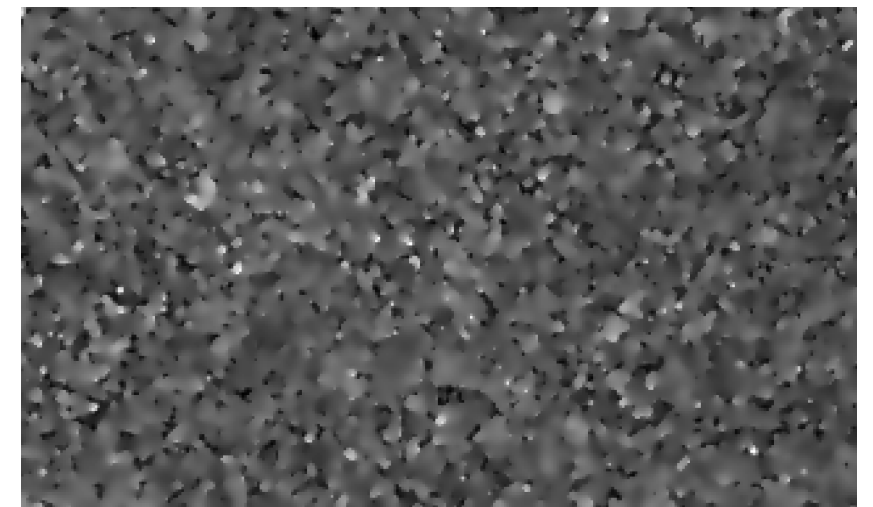
j) Bilateral



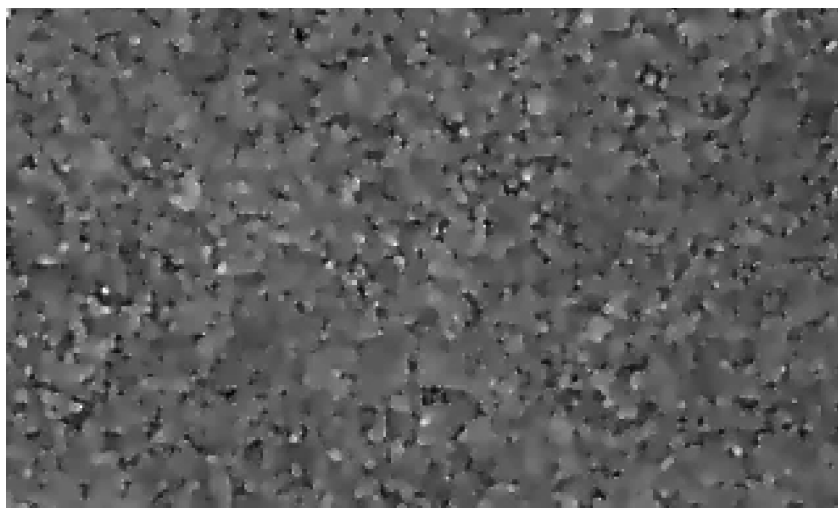
k) Guided filter



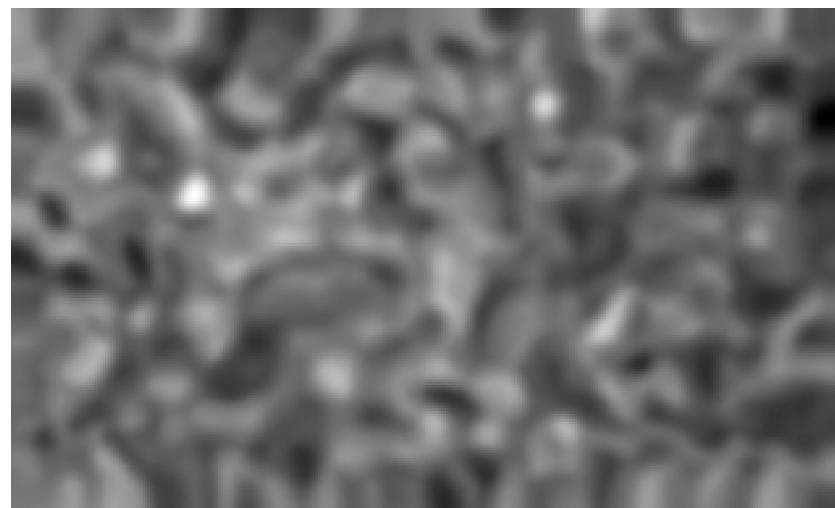
l) SRAD



m) Improved DWT



n) SAR BM3D



o) Gamma Map

